AD-A075 419 AIR FORCE ACADEMY CO F/G 20/4
AIR FORCE ACADEMY AERONAUTICS DIGEST. SPRING 1979.(U)
JUL 79 E J JUMPER, M M TOWE
UNCLASSIFIED USAFA-TR-79-7 NL

1 OF 2
AD
A075419

AD A075419

DDC FILE COPY

LEVEL

USAFA-TR-79-7

AIR FORCE ACADEMY

AERONAUTICS DIGEST - SPRING 1979

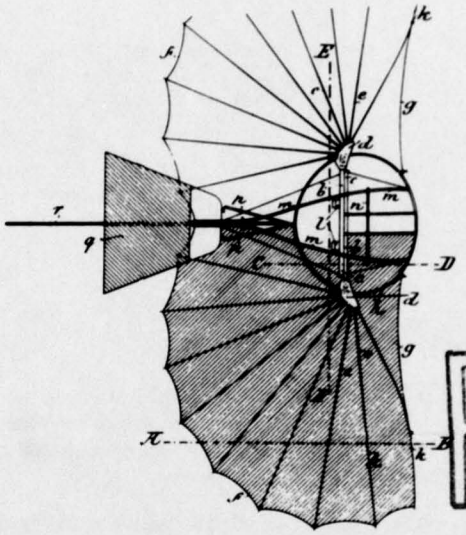

JULY 1979

FINAL REPORT

DDC
RECEIVED
OCT 24 1979
A

APPROVED FOR PUBLIC RELEASE: DISTRIBUTION UNLIMITED

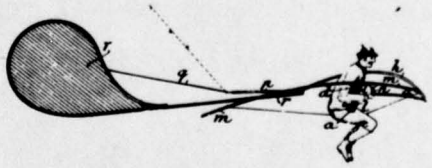

DEPARTMENT OF AERONAUTICS
DEAN OF THE FACULTY
UNITED STATES AIR FORCE ACADEMY
COLORADO 80840

Inventor: Otto Lilienthal
By Attorney: J. E. Lilienthal

79 22 22 128

AERONAUTICS DIGEST - SPRING 1979

COVER:
The figure on the cover is a blueprint of the patent obtained in 1893 by Otto Lilienthal for his hang-glider. As a German engineer he designed and built two dozen prototypes. He was the first man in the world to launch himself into the air and fly; many of his flights were over 1000 feet. He had over 2500 gliding flights before his death in 1896 when he stalled and nose-dived his glider into the ground.

Editorial Review by Capt Fannalou Guggisberg
Department of English
USAF Academy, Colorado 80840

This document is presented as a compilation of monographs worthy of publication. The United States Air Force Academy vouches for the quality of research, without necessarily endorsing the opinions and conclusions of the authors.

This digest has been cleared for open publication and/or public release by the appropriate Office of Information in accordance with AFR 190-17 and DODD 5230.9. There is no objection to unlimited distribution of this digest to the public at large, or by DDC to the National Technical Information Service.

This digest has been reviewed and is approved for publication.

John P. Wittry

JOHN P. WITTRY, Colonel, USAF
Vice Dean of the Faculty

UNCLASSIFIED
SECURITY CLASSIFICATION OF THIS PAGE *(When Data Entered)*

REPORT DOCUMENTATION PAGE

READ INSTRUCTIONS BEFORE COMPLETING FORM

1. REPORT NUMBER (14) USAFA-TR-79-7	2. GOVT ACCESSION NO.
3. RECIPIENT'S CATALOG NUMBER	
4. TITLE *(and Subtitle)* (6) Air Force Academy Aeronautics Digest, Spring 1979	5. TYPE OF REPORT & PERIOD COVERED (9) Final Report,
6. PERFORMING ORG. REPORT NUMBER	
7. AUTHOR(s)	8. CONTRACT OR GRANT NUMBER(s)
9. PERFORMING ORGANIZATION NAME AND ADDRESS Department of Aeronautics United States Air Force Academy, CO 80840	10. PROGRAM ELEMENT, PROJECT, TASK AREA & WORK UNIT NUMBERS 011 550
11. CONTROLLING OFFICE NAME AND ADDRESS (12) 167	12. REPORT DATE (11) July 1979
	13. NUMBER OF PAGES 162
14. MONITORING AGENCY NAME & ADDRESS *(if different from Controlling Office)*	15. SECURITY CLASS. *(of this report)*
	15a. DECLASSIFICATION/DOWNGRADING SCHEDULE

16. DISTRIBUTION STATEMENT *(of this Report)*

Approved for Public Release; Distribution Unlimited

17. DISTRIBUTION STATEMENT *(of the abstract entered in Block 20, if different from Report)*

(10) E. J. /Jumper M. M. /Tower

18. SUPPLEMENTARY NOTES

19. KEY WORDS *(Continue on reverse side if necessary and identify by block number)*

Aerodynamics, Fluid Mechanics, Thermodynamics, Education, Wind Tunnel

20. ABSTRACT *(Continue on reverse side if necessary and identify by block number)*

This digest covers unclassified research in aeronautics performed at the United States Air Force Academy during the six months ending 1 July 1979. This report includes individual technical papers in the specific areas of aerodynamics, fluid mechanics, experimental instrumentation, engineering education and thermodynamics and heat transfer.

011 550

DD FORM 1 JAN 73 1473 EDITION OF 1 NOV 65 IS OBSOLETE

UNCLASSIFIED
SECURITY CLASSIFICATION OF THIS PAGE *(When Data Entered)*

PREFACE

This report is the third issue of the Air Force Academy Aeronautics Digest. The articles printed here represent recent scholarly work by students and faculty of the Department of Aeronautics, members of other departments of the Academy and The F. J. Seiler Research Laboratory, researchers directly or indirectly involved with USAFA-sponsored projects, and authors in fields of interest to the USAFA.

In addition to complete papers, the Digest also includes, when appropriate, abstracts of lengthier reports and articles published in other formats. The editors will consider for publication contributions in the general field of Aeronautics, including

-Aeronautical Engineering
  --Flight Mechanics
  --Propulsion
  --Structures
-Fluid Mechanics
-Thermodynamics and Heat Transfer
-Engineering Education

Papers on other topics will be considered on an individual basis. Contributions should be sent to:

Editor, Aeronautics Digest
DFAN
US Air Force Academy, CO 80840

The Aeronautics Digest is presently edited by Captain E. J. Jumper, PhD, and Captain M. M. Tower, PhD, with the cooperation of the Department of English. In particular, the Digest would like to thank Captain Fannalou Guggisberg for her yeoman's service as liaison officer from DFENG. She gave many long hours of dedicated assistance to the Digest and provided the final editorial review. Our thanks also to our secretary, Mary Lynne Wright, for her diligent typing and cheerful attitude.

Accession For
NTIS GRA&I
DDC TAB
Unannounced
Justification
By
Distribution/
Availability Codes
Dist | Avail and/or special
A

CONTENTS

Section		Page
I.	AERODYNAMICS	1
	AERODYNAMICS OF PROPOSED SPOILER AND LASER CAVITY CONFIGURATIONS ON THE AIRBORNE LASER LABORATORY ----M. M. Tower	2
	PHYSICS OF A HOT AIR BALLOON ----J. P. Jackson	33
II.	FLUID MECHANICS	55
	STREAMLINE PLOTTING FOR AXISYMMETRIC CONE IN SUPERSONIC FLOW ----M. P. Baudhuin	56
III.	THERMODYNAMICS AND HEAT TRANSFER	65
	OPTIMIZATION OF LOW QUALITY ENERGY CONVERSION ----R. C. Winn	66
	PERFORMANCE OF GROOVED HEAT PIPE EVAPORATORS WITH VAPOR RELEASE SLOTS ----R. C. Oliver	72
IV.	PROPULSION	87
	EVALUATION OF A GLUHAREFF PRESSURE JET ----H. M. Brilliant	88
V.	INSTRUMENTATION AND HARDWARE	100
	CALIBRATION OF FIVE-HOLE PROBES FOR ON-LINE DATA REDUCTION ----K. W. Barker, R. W. Gallington, and S. N. Minster	101
	A FAST METHOD FOR ACCURATE MANUFACTURE OF SMALL FIVE-HOLE PROBES ----R. W. Gallington and C. F. Hollenbaugh	114
	A LASER DOPPLER VELOCIMETER SYSTEM TO INVESTIGATE UNSTEADY FLOW SEPARATION ----G. W. Sparks, Jr., J. P. Retelle, Jr., J. E. Keesee, M. S. Francis, and J. M. Lind	120
	PRELIMINARY WORK ON A PITOT-STATIC HANDBOOK ----W. Dieterich	136
VI.	ABSTRACTS	159
	PREDICTED AND MEASURED MAXIMUM INSTANTANEOUS DISTORTION FOR FLIGHT AND WIND TUNNEL MODEL DATA FOR A MIXED-COMPRESSION INLET ----H. M. Brilliant, C. A. Bauer, and R. A. Davis	160

SECTION I

AERODYNAMICS

AERODYNAMICS OF PROPOSED SPOILER AND LASER CAVITY CONFIGURATIONS ON THE AIRBORNE LASER LABORATORY

Michael M. Tower*

Abstract

Seven wind tunnel experiments dealing with airflow in and around cavities located in the wake of porous spoilers are discussed. The investigation was conducted in the Trisonic Wind Tunnel at the Air Force Academy. The experimental models were designed to study the flow characteristics associated with the laser cavity and exhaust ports on the Air Force Airborne Laser Laboratory. The purpose of the porous spoiler is to reduce the vortex flow and acoustical vibrations within the cavity. To determine the flow characteristics and relative merit of spoiler design, we employed a flow visualization technique using an oil-tracer paint. The static pressure on the cavity walls and floor was measured by static pressure ports connected to a manometer bank. Also included in this paper is a literature search with relevant conclusions applicable to the spoiler and cavity flow problem.

I. Introduction

The information contained within this paper is a compendium of work performed between January 1975 and December 1977 by Lt Col Richard F. Felton, Capt Michael M. Tower, and numerous Academy cadets in their laboratory and independent research courses.

A. Background

The Airborne Laser Laboratory, ALL, at Kirtland Air Force Base, NM, is a modified Boeing C-135 transport aircraft containing a laser device for projecting a laser beam. The beam is projected from the C-135 through an open port housed in a turret on top of the fuselage, as shown in Figure 1. There are also two exhaust ports under the fuselage for the hot laser exhaust gases to be vented.

Three problems arise in relation to the open laser cavity and exhaust ports: acoustical vibration, density variations, and vortical flow into the ports. The acoustical vibrations occur as a result of the airstream passing over the open port and causing a whistle-like effect. The resultant sound waves cause vibrations in the laser optics. The shedding of vortices from the upstream lip of the cavity causes the last two problems. These vortices cause density gradients and flow into the laser cavity. The density gradients are particularly troublesome because they refract the laser beam causing beam scattering and misalignment.

B. Objective

The purpose of this paper is to elaborate on previous work obtained from a literature search on the flow characteristics causing the problems of acoustical

---

*Captain, USAF, Associate Professor of Aeronautics, DFAN

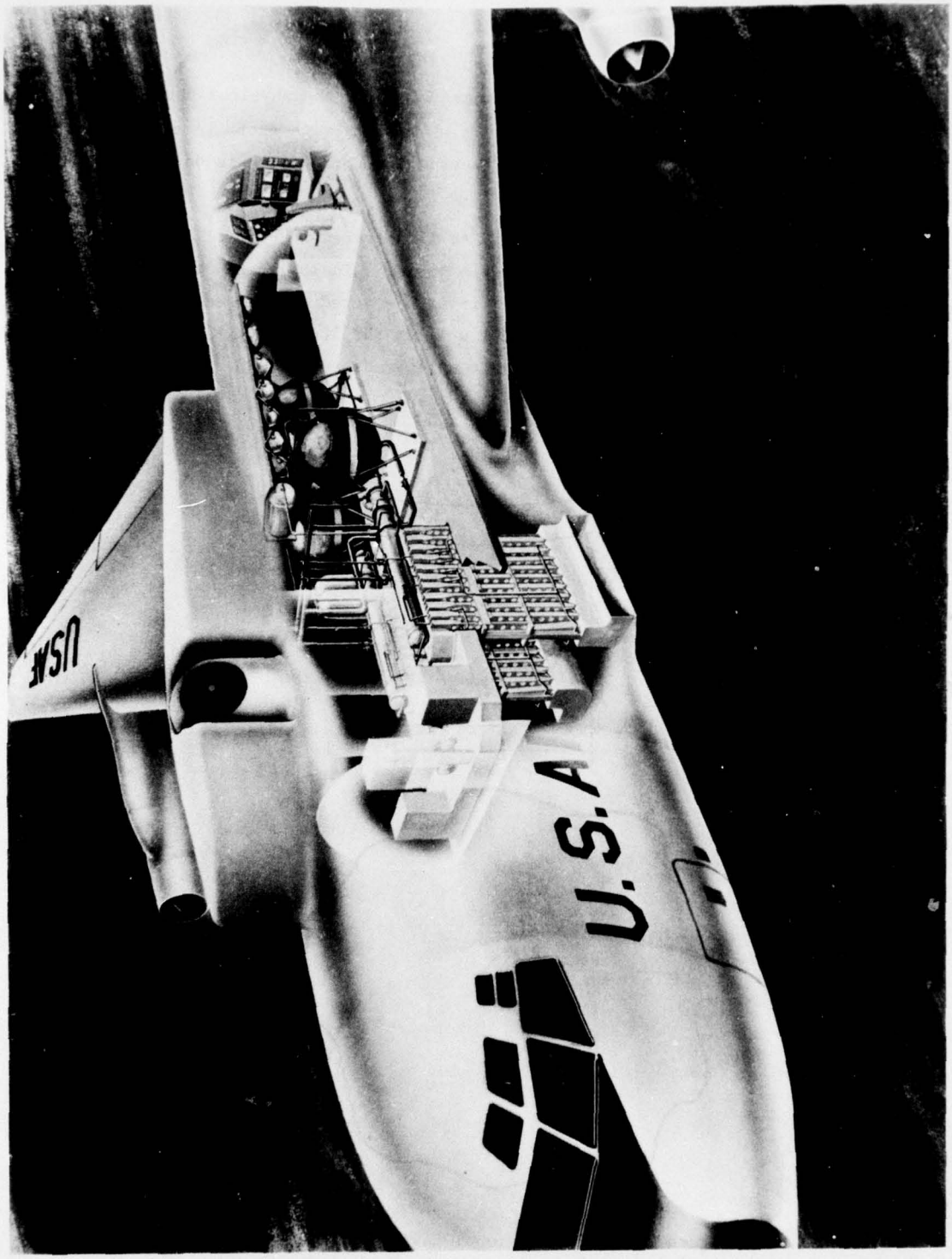

Figure 1. Airborne Laser Laboratory

vibration, vortex flow, and density gradients, then to summarize the experiments performed here at the Academy and draw conclusions pertinent to the Airborne Laser Laboratory.

II. Literature Search

As early as 1878, Strouhal made an experimental study of the physical phenomena associated with the flow over an open cavity. And Rayleigh (Ref. 1) stated in 1896, "The cause for oscillation (pressure fluctuation) production is doubtless connected with the instability of vortex sheets...."

As the freestream air passes over a cavity, as illustrated in Figure 2, circular flow is induced within the cavity in the form of a vortex. In the steady flow case the vortex sheet shed from the leading edge cavity lip is convected downstream and influenced by the interior cavity flow. The vertical wall at the leading edge tends to distort the vortex sheet downward whereas the aft wall tends to bend the vortex sheet upward (Ref. 2) as shown in Figure 2.

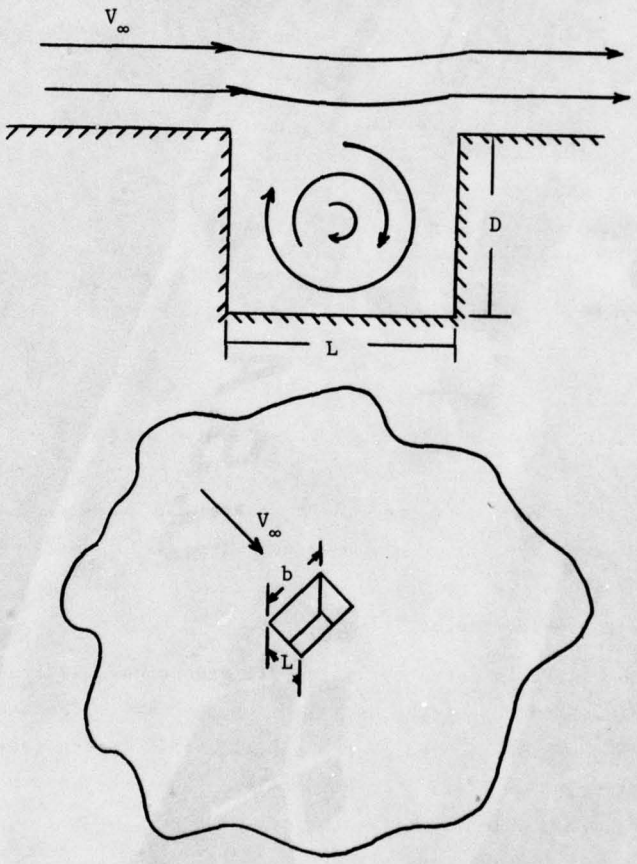

Figure 2. Two-Dimensional Cavity Flow

If the velocity is changed a perturbation will result producing additional vorticity and non-steady conditions. The vorticity will exert a force at right angles to the plane defined by the vortex and velocity vector (Circulation Theory of Lift). This force results in an induced velocity and the product of the force and velocity results in work on the cavity. If the rate of doing work is less than the ability of the cavity to dissipate energy by viscosity (heat interactions) and radiation (acoustical sound), the perturbations will be damped and flow will return to steady state. If the work on the cavity is greater than viscous and radiation dissipation, then the intensity and frequency of the oscillations will increase until the energy dissipated equals the energy supplied. The lowest value of frequency at which the oscillations will start is of the order of the lowest natural frequency of the cavity energy storage system. The laser cavity energy storage capability is difficult to determine, but this information would be useful in predicting whether the flow within the cavity is steady or unsteady.

Classical vortex kinematics (Ref. 3) gives us some further insight into the properties of cavity flow. It states: an isolated vortex in the presence of a solid wall tends to move parallel to the wall with a velocity less than that induced by the vortex. This yields the following three conclusions. First, in a deep cavity ($L/D<.25$) the vorticity is primarily governed by the images in the forward and aft walls. Secondly, in a shallow cavity ($L/D>4$) the vorticity is governed by the bottom and the flow across the top of the cavity. And finally, the spanwise walls do not influence the vortex motion.

Squire (Ref. 4) states that for most steady state analytical studies the vorticity can be assumed constant within the cavity core because the residual action of viscosity tends to destroy vorticity gradients. He further states that the velocity in the cavity may be as much as 30% of the freestream velocity.

For low Reynolds numbers and steady flow, Pan and Acrivos (Ref. 5) used numerical relaxation techniques to mathematically model the vorticity system established in deep rectangular cavities. They confirmed their theoretical work with experiments using a smoke tunnel. Their results can be summarized in Figure 3 which shows the number of distinct vortices versus cavity depth. They also determined that the speed of circulation decreases with cavity depth.

According to O'Brien's (Ref. 6) finite difference calculations, even for steady flow the vortices within the cavity oscillate up and down. She states that the two principal factors required to predict the vortex system in the cavity are the cavity geometry and external flow field. In her analysis she used both Couette and Poiseuille flow for the freestream velocity distribution.

Mehta and Lavan (Ref. 7) used finite difference techniques to solve the equations of motion for flow in a channel with a rectangular cavity. They varied the Reynolds number and as it increased from low values, they reached three conclusions: (1) the

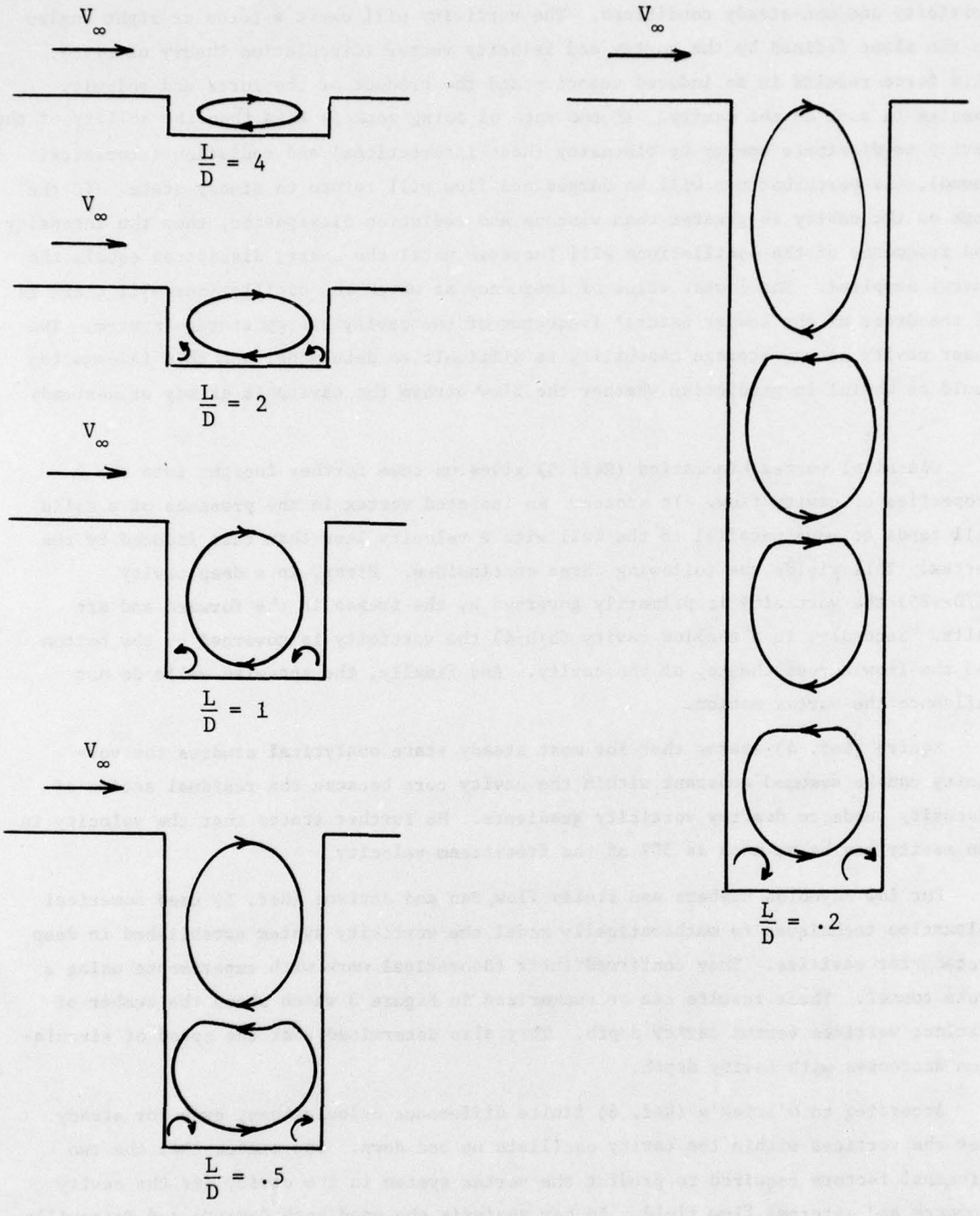

Figure 3. Vortex System in Cavities of Varying Depth, $R_e = 4000$

strength of the vortices increases, (2) the vortex centers shift downstream and upward, and (3) the streamline dividing the cavity flow and the channel flow is concave at low Reynolds numbers and convex at higher numbers, except at the corners, where it is always concave.

Up to this point all previous work has concluded that the vortex flow in the cavity is two dimensional. In work by Maull and East (Ref. 8) they found that in some circumstances the flow within the cavity is three dimensional. By varying the depth-to-span ratio they observed non-steady, three-dimensional motion for ratios of $1.2 \leq D/B \leq 1.52$ and span-to-length ratios greater than two. They also performed some experiments varying the cavity lip geometry, see Figure 4, for a velocity range of 90 fps to 200 fps. In Figure 4a the aft cavity lip was rounded. The effect produced two improvements: first, it increased the stability of the flow with respect to time, and secondly, it reduced the amplitude of the wave pattern of the spanwise pressure distribution to about a quarter that of a sharp corner. Another geometry tested is shown in Figure 4b where there is an overhang of the lip. The major result in flow modification in this case was to reduce the three-dimensional flow to two-dimensional motion.

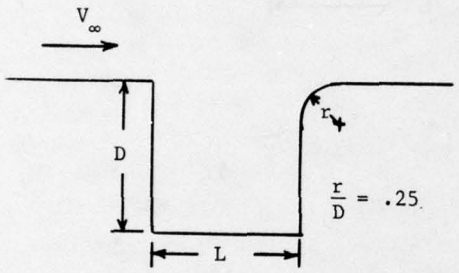

Figure 4a. Rounded Aft Cavity Lip

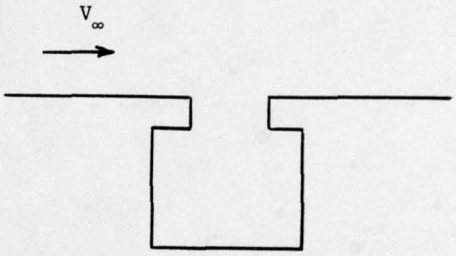

Figure 4b. Overhang Cavity Lip

An analytical study at high Mach numbers ($.8 \leq M \leq 3.0$) was performed by Bilanin and Covert (Ref. 9), who reached several interesting conclusions as to the overall picture. They found that cavities of rectangular, triangular, and circular planforms can be treated as two-dimensional flow. Further, the flow can be treated as inviscid everywhere with a high degree of accuracy; however the flow outside the cavity should include forced convection and within the cavity the acoustic (energy-storing) phenomenon must be considered.

Mills (Ref. 10) reached the same conclusions as Squire in that the vorticity within the vortex core is constant for flow over a square cavity. He was particularly looking at the velocity profiles within the laminar boundary layer on the cavity walls and floor. He substantiated the theoretical velocity profiles by his experiment. His results are shown in Figure 5.

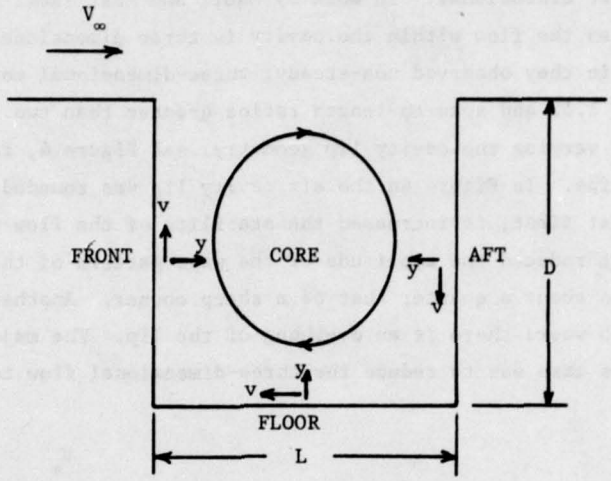

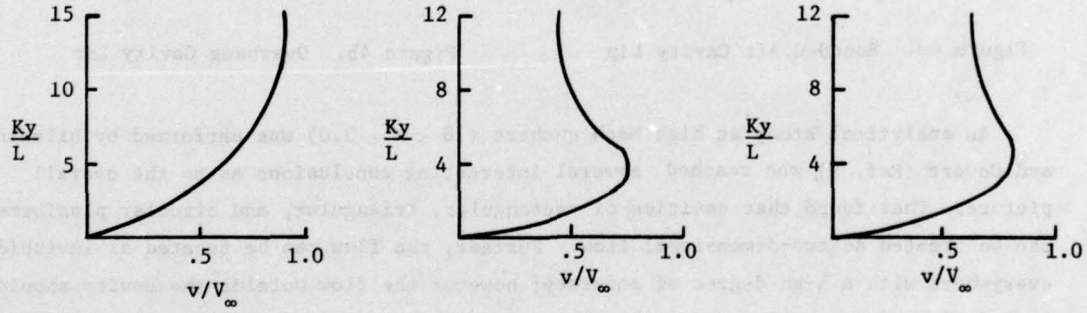

$$K = \left[\frac{V_\infty \pi L \rho}{2 \mu}\right]^{1/2}$$

μ - Viscosity coefficient
ρ - Density

Figure 5. Velocity Profiles for Laminar Boundary Layer on Cavity Walls and Floor

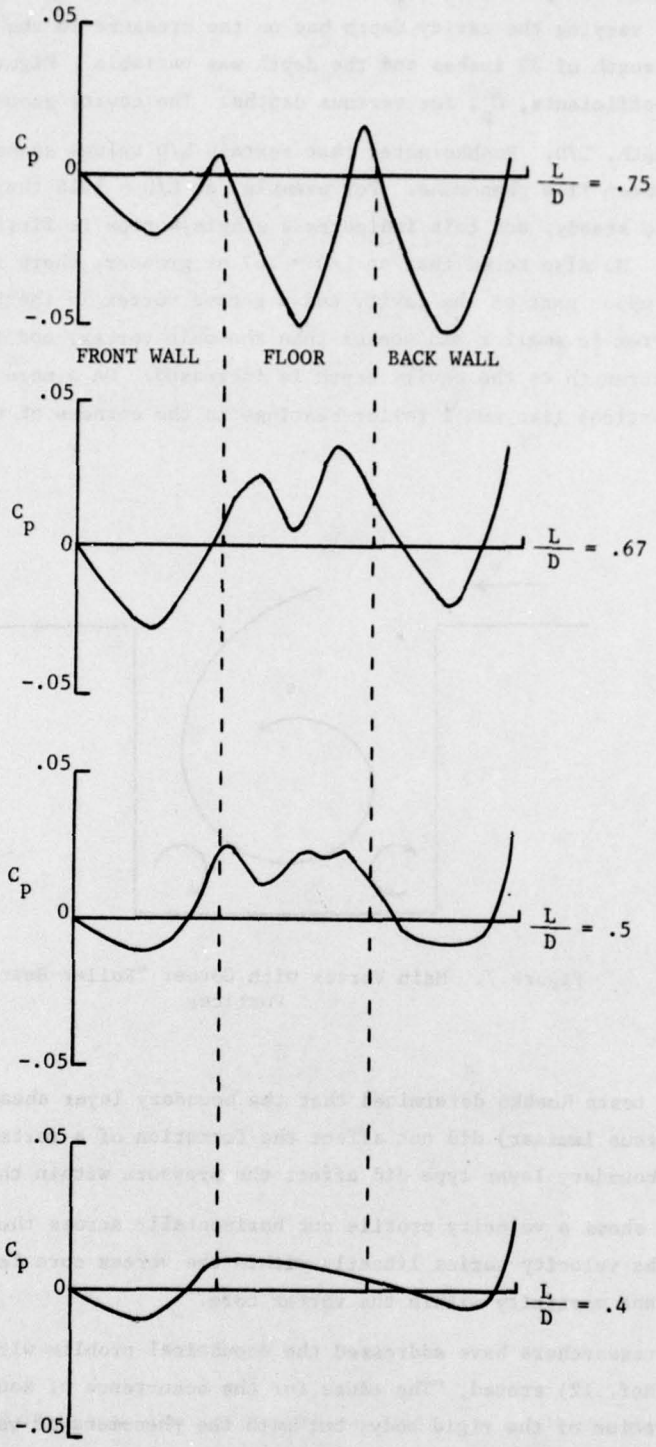

Figure 6. Variation of Pressure Coefficient Along Cavity Walls and Floor for V_∞ = 77 fps

Roshko (Ref. 11) performed experiments at low velocities (V = 77fps) to discover the effects varying the cavity depth has on the pressure in the cavity. Roshko's cavity had a length of 32 inches and the depth was variable. Figure 6 shows the change in pressure coefficients, C_p, for various depths. The cavity geometry is expressed as length over depth, L/D. Roshko noted that certain L/D values seemed to mark the transition between flow phenomena. For example, at L/D = 1.15 the pressures change from intermittent to steady, and this indicates a single vortex is first formed in the cavity of this depth. He also noted that at L/D = .67 or greater, there is a strong main vortex in the upper part of the cavity and a second vortex in the bottom of the cavity. The second vortex is smaller and weaker than the main vortex, and the main vortex decreases in strength as the cavity depth is increased. On a more detailed level Roshko found small vortices like small roller bearings in the corners of the cavity as shown in Figure 7.

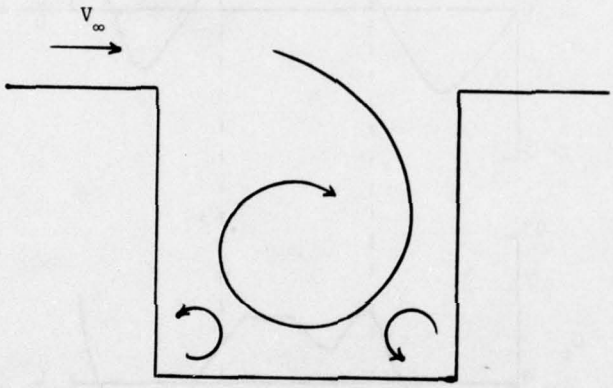

Figure 7. Main Vortex with Corner "Roller-Bearing" Vortices

In other tests Roshko determined that the boundary layer ahead of the cavity (turbulent versus laminar) did not affect the formation of a vortex in the cavity. However, the boundary layer type did affect the pressure within the cavity.

Figure 8 shows a velocity profile cut horizontally across the cavity. As seen in the figure, the velocity varies linearly within the vortex core leading to the conclusion of constant vorticity within the vortex core.

Several researchers have addressed the acoustical problem within the cavity. Blokhintsev (Ref. 12) stated, "The cause for the occurrence of sound is not connected with the vibration of the rigid body, but with the phenomena of vortex formation in the flow of a fluid," which he called "vortical sound." Krishnamuity (Ref. 13) puts it another way, "Aerodynamic shear energy is converted to acoustical energy."

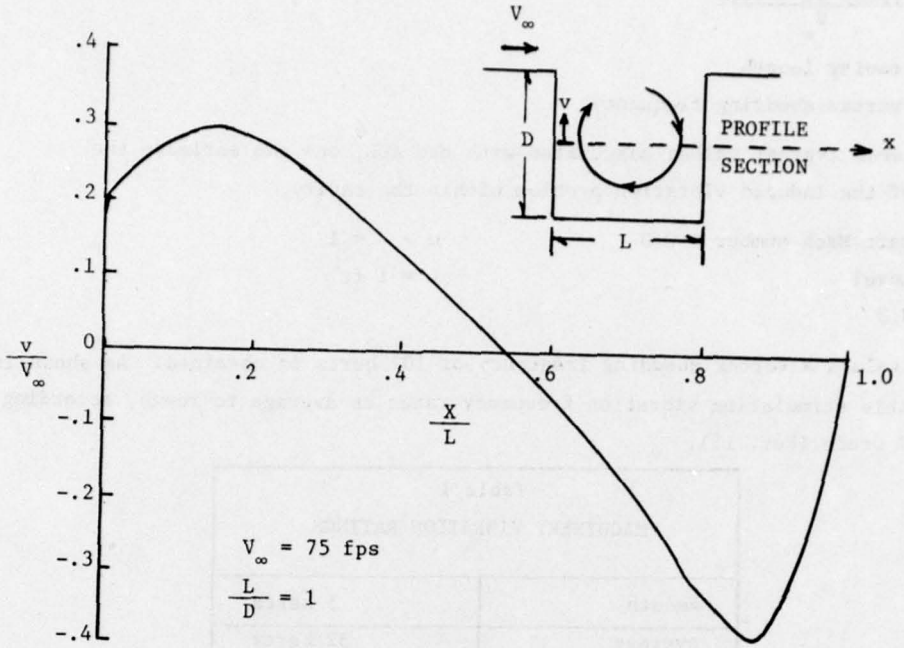

Figure 8. Velocity Profile Across a Square Cavity

Krishnamuity (Ref. 13) experimentally studied bomb bay openings in the form of small rectangular cavities over a Mach number range of $.25 < M < 1.5$. His cavity dimensions varied from $0.5 \leq L/D \leq 4$. He determined that the acoustical emissions within the cavity were a function of the freestream boundary layer, L/D ratio, and Mach number. His conclusions can be summarized: (1) laminar freestream boundary layers produce stronger acoustic emissions, whereas turbulent freestream boundary layers produce more violent motion in the cavity, but lead to weaker acoustic emissions; (2) larger L/D ratios produce stronger acoustic emissions; and (3) the lower Mach numbers produce stronger acoustic emissions.

Rossiter (Ref. 14) gives the vortex shedding frequency in square cavities as

$$f = \frac{V_\infty}{L} \frac{m - \gamma}{\frac{1}{k} + \frac{V_\infty}{a_\infty}} \qquad (1)$$

where

V_∞ - freestream velocity

a_∞ - freestream sound speed

$m = 1, 2, 3, \ldots$ - resonant frequencies

γ - phase relation constant between vortex motion and acoustic motion

$$K = \frac{\text{speed of vortex}}{V_\infty}$$

L - cavity length

f - vortex shedding frequency.

Selecting some typical values associated with the ALL, one can estimate the severity of the induced vibration problem within the cavity.

Aircraft Mach number = 0.3 $\quad m - \gamma = 1$

Sea Level $\quad L = 1$ ft

K = 0.3

For these values a vortex shedding frequency of 102 hertz is obtained. As shown in Table 1, this stimulating vibration frequency rates as average to rough, according to Harris and Crede (Ref. 15).

Table 1
MACHINERY VIBRATION RATINGS

smooth	5 hertz
average	32 hertz
rough	127 hertz

Performing a similar calculation for a Mach number equal to 0.7, which is the upper cruise velocity for the ALL, obtained a frequency of 211 hertz. Reference 16 places the vibration frequencies of turbojet aircraft at less than 500 hertz. The conclusion seems to be that the vortex shedding frequencies are of the same order of magnitude as the natural vibration of the KC-135.

Two flight test projects with open ports have been reported. One experiment was conducted as part of the Ames Airborne Infrared Observatory Project (Ref. 17). In this project a telescope was mounted in an open fuselage cavity on the side of a C-141 aircraft. An open port was used since a window cannot be used for this type of telescope. In order to ensure that the telescope optics would remain steady, an investigation to suppress the acoustic resonance was made. A porous spoiler was used to accomplish the suppression.

The spoiler designed for the C-141 was made of 19 individual sections fastened to the aircraft by a hinge. They could be extended at different angles and had porosities of 38%. The spoiler was mounted ahead of the cavity as shown in Figure 9.

Data were taken on the spoiler and cavity arrangement in a series of nine flights. Mach numbers varied from 0.58 to 0.76. The spoiler was extended from 15 to 90 degrees with the cavity open. High-frequency-response pressure transducers spanning the

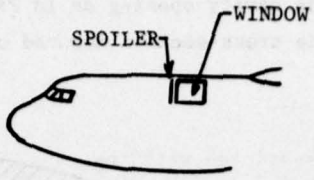

Figure 9. C-141 Aircraft and Spoiler

interior walls obtained pressure data in the cavity. The data showed that the mean static pressure in the cavity was approximately equal to the ambient pressure. Pressure fluctuation coefficients tended to increase with spoiler extension but decrease with increasing Mach number. It was also found at the higher Mach numbers a high frequency oscillation created ahead of the spoiler was transmitted into the cavity. Taking flight maneuvers into consideration, Ames found that a spoiler extension of 30 degrees yields minimum resonance.

Perhaps the most relevant study is that reported by Buell (Ref. 18) of the Ames Research Center where tests were conducted on cavities with anti-resonance devices in the Ames supersonic wind tunnel and on a KC-135 aircraft in flight. This study was brought about by the need to mount an infrared telescope in an aircraft where a window could not be used.

The devices tested in the tunnel consisted of two basic configurations. One was a high-aspect-ratio diffuser as shown in Figure 10 and was constructed so that air passed beneath the ramp, through a divergent channel and porous surface, and over the cavity.

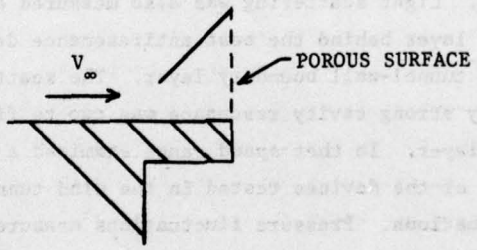

Figure 10. 45^o Diffuser Spoiler

It was intended that this diffusion process would cover the opening with a thick blanket of low-energy air. The spoiler height was chosen because it is approximately equal to the thickness of the boundary layer on the wind tunnel wall. Removing the

ramp tested a porous spoiler configuration also. The second configuration was a long diffuser wrapped around the cavity opening as in Figure 11. It consisted of a cambered plate with a streamline cross-section mounted on a porous support.

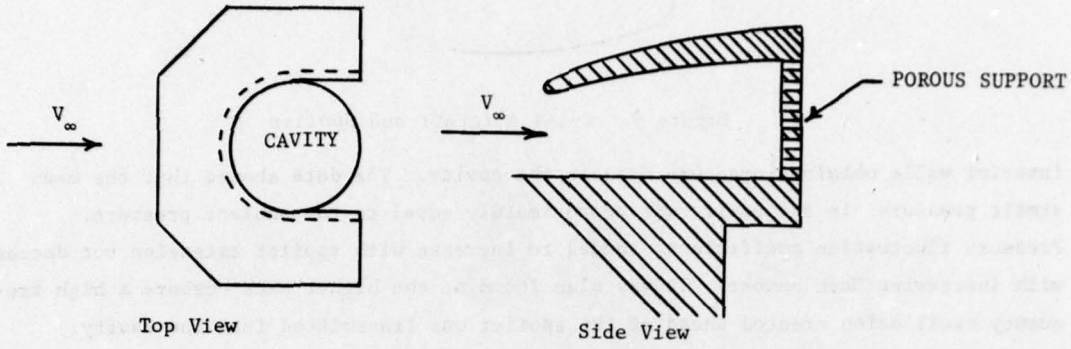

Figure 11. Airfoil Wrap-Around Diffuser Spoiler

The aircraft tests used a 45-degree diffuser, similar to the one tested in the wind tunnel (Figure 10), mounted ahead of a rectangular opening in the KC-135. The cavity contained a mirror, gimbals, torque motors, and the front end of the telescope tube. Data were collected using pressure transducers and total pressure rakes. Mach numbers in the tunnel ranged from 0.6 to 0.9 and on the aircraft from 0.6 to 0.8.

The test results yielded that a solid spoiler was clearly inferior to the other configurations tested in suppressing cavity resonance, indicating that some minimum amount of flow through the porous surface is required for the spoiler to be effective. Also, it was shown that the shape of the opening, square or circular, was unimportant to pressure fluctuation. Light scattering was also measured and it was found that the scattering in the shear layer behind the best antiresonance devices was less than half the scattering from the tunnel-wall boundary layer. The scattering from the thicker shear layers produced by strong cavity resonance was two to five times as great as that from the wall boundary layer. In that speed range examined a 35 percent porous spoiler was the most consistent of the devices tested in the wind tunnel in maintaining a low level of pressure fluctuations. Pressure fluctuations measured in the airplane cavity were of about the same magnitude as those in the best wind tunnel configuration.

Some previous experiments relevant to the ALL were conducted by Castro (Ref. 19) on the wake downstream of a porous spoiler. Castro's initial model had a rectangular porous fence mounted perpendicular to the airflow. As shown in Figure 12, he found that a fence of zero porosity produced two vortices downstream of the fence. These vortices are caused by the shedding of the two shear layers at the fence tips, which

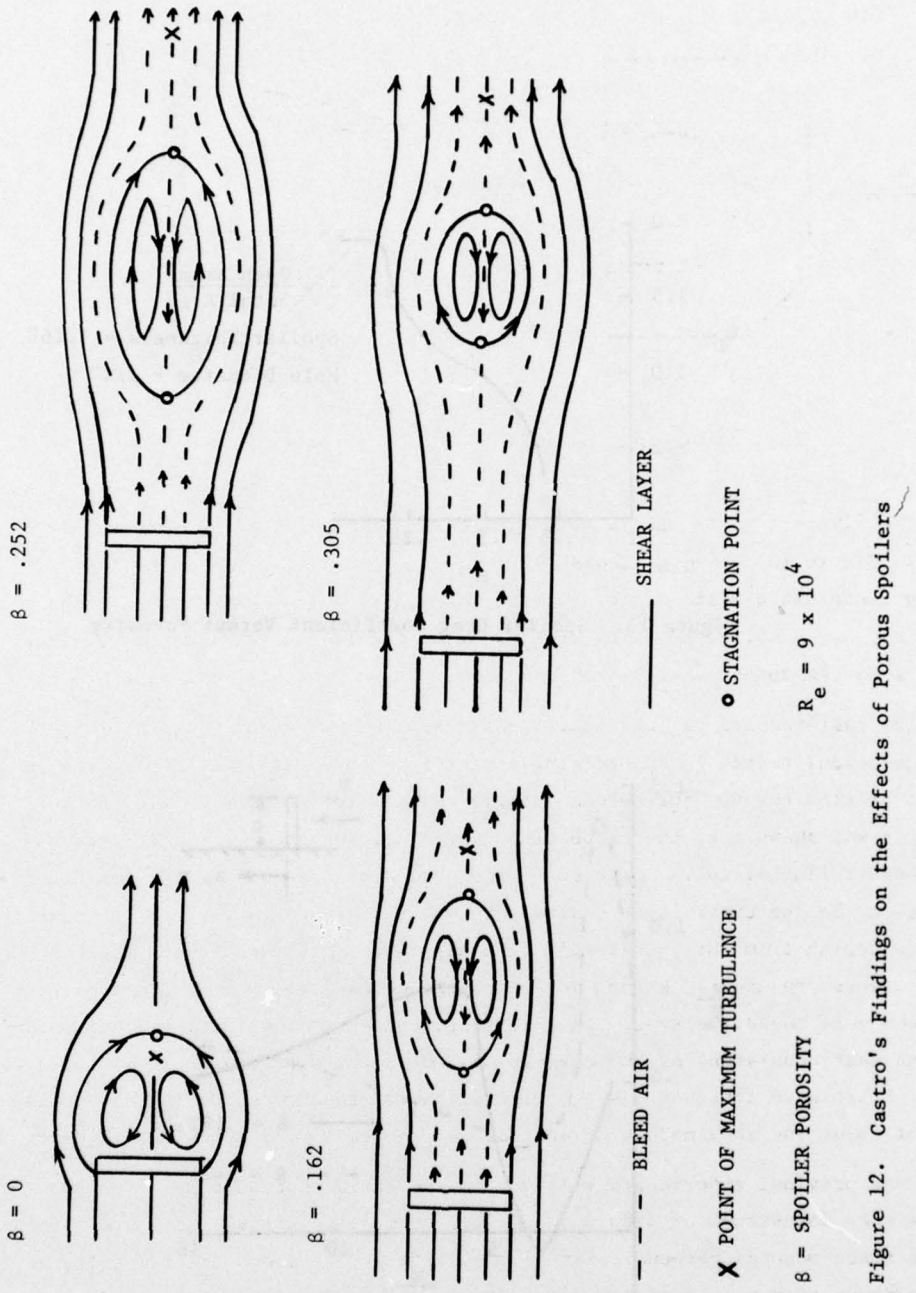

Figure 12. Castro's Findings on the Effects of Porous Spoilers

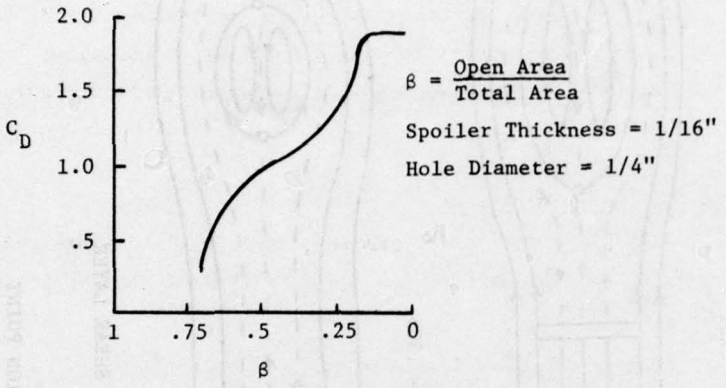

Figure 13. Spoiler Drag Coefficient Versus Porosity

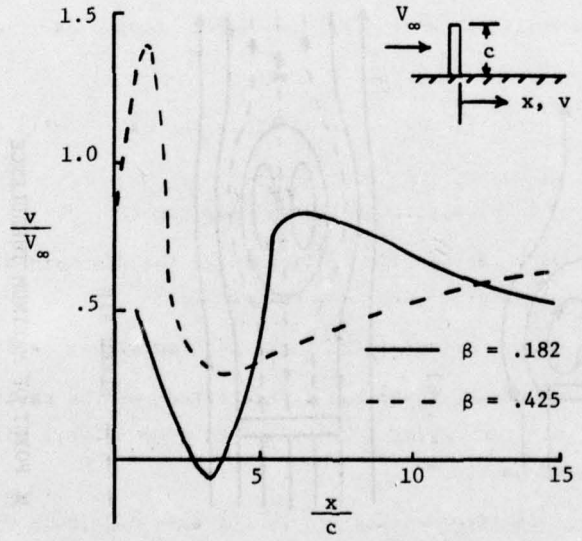

Figure 14. Wake Velocity Ratio Versus Downstream Distance

interact in the near wake. The near wake flow reverses upstream and a stagnation point is formed. Castro determined that if air is bled into the wake through the porous spoiler, the vortex formation point and stagnation points move downstream.

Castro's experiments showed that by increasing the fence's porosity, the stagnation region could be moved farther downstream. This stagnation region might be an optimal location for a laser cavity or exhaust port, so that the air inside the cavities would be under the stagnant region. It should be noted that the highest porosity used by Castro was $\beta = 0.305$.

Other results presented by Castro are shown in Figures 13 and 14. Figure 13 depicts the spoiler's drag coefficient as a function of porosity. Figure 14 shows the ratio of wake velocity to freestream velocity versus length downstream for low and high porosity.

III. Summary of Literature Search Conclusions

The following list of conclusions drawn from the literature search seems particularly relevant to the analysis of the laser cavity and exhaust ports on the Airborne Laser Laboratory.

A. Vortices will be established within the cavity.

B. Vortices within the cavity can be assumed in steady state and of constant vorticity.

C. Rotational flow within the cavity can be as large as 30% of the freestream velocity.

D. More than one distinct vortex is established in deep cavities.

E. The speed of rotation decreases with depth.

F. Even in steady state flow, vortices within the cavity will oscillate up and down.

G. Vortex strength is proportional to Reynolds number.

H. Flow within cavity can usually be treated as two dimensional; however, spanwise flow can occur for large span-to-depth ratios.

I. Cavity lip geometry can stabilize vortical flow within cavity.

J. The freestream boundary layer has little effect on the cavity flow, but does affect the pressure within the cavity. Turbulent boundary layers will cause more violent motion within the cavity.

K. The vortex shedding frequencies are of the same magnitude as the natural vibration of the KC-135.

L. Porous spoilers are superior to solid spoilers in reducing cavity resonance.

M. Porous spoilers can reduce the density gradients to such an extent that light scattering can be reduced to half that refracted by a boundary layer over a glass window.

N. Porous spoilers can be used to control a stagnation region downstream. Porosities of 35% for $0.6 \leq M \leq 0.9$ produce the largest stagnation regions in the spoiler wake.

IV. *Summary of Experiments*

The following section is a summary of experiments and major conclusions drawn from the work of several instructors and cadets at the Air Force Academy from 1975 through 1977. The results are presented in chronological order to show the evolution and growing sophistication of experiments. The Academy's Trisonic Wind Tunnel was used for all experiments.

A. Lindsay's Experiment

Performed by Charles L. Lindsay (Ref. 20) from 1 September 1975 to 15 December 1975.

1. Purpose

Flow visualization of the near wake behind a porous spoiler.

2. Test Apparatus

A flat plate was exposed to the freestream with a porous spoiler normal to the airflow as shown in Figure 15.

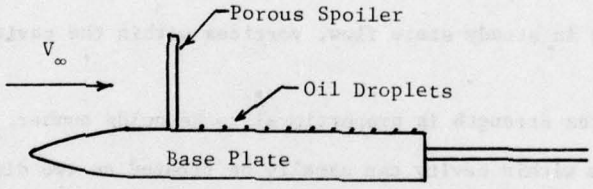

Figure 15. Flow Visualization Model

Oil droplets were sprayed on the base plate prior to wind tunnel operation. During operation the oil droplets moved in the airflow direction, leaving a telltale trail of flow direction. Figure 16 shows the actual hardware. The spoilers were 1 to 1.5 inches high with 0.125 and 0.25 inch holes for porosity. Porosity varied from 7 to 32 percent.

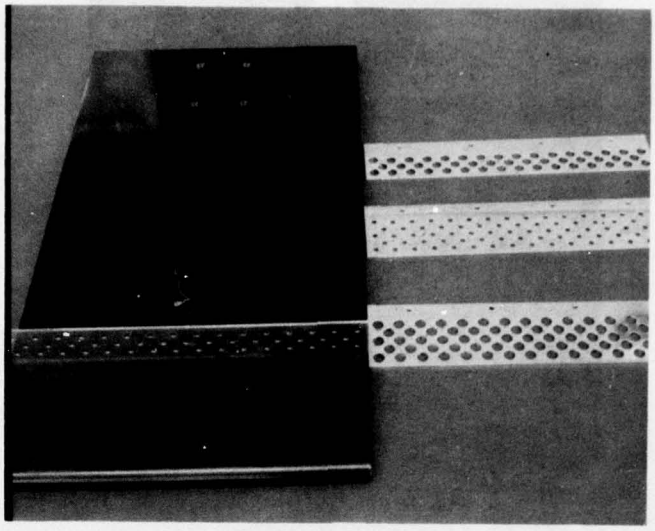

Figure 16. Lindsay's Test Apparatus

3. Test Velocity

All tests were run at M = 0.48

4. Conclusions

a. The experiment essentially confirmed the work done by Castro (Ref. 19)

b. Two stagnation regions exist in the spoiler wake as seen in Figure 17.

c. The highest porosity (32%) produced the most uniform flow in the spoiler's wake.

d. The tallest spoiler (1.5 inches) moved the stagnation regions the farthest downstream.

B. Hatfield's Experiment

Performed by David N. Hatfield (Ref. 21) from 1 January 1976 to 15 May 1976.

1. Purpose

To determine the spoiler's desirability by varying thickness, porosity, hole placement, and hole size.

2. Test Apparatus

A flat plate similar to Lindsay's experiment (Ref. 20) was exposed to the freestream with a porous spoiler normal to the airflow. Flow visualization was again used by observing the motion of oil droplets.

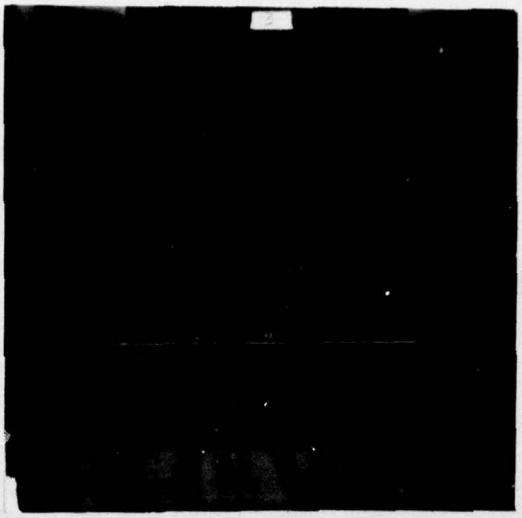

Figure 17. Near Wake Flow Visualization

The spoiler's porosity was ranged from 10 to 40 percent and was achieved by varying the hold size (0.125 to 0.25 inches) and placement, as shown in Figure 18. The spoiler was also tested for thickness from 0.03125 to 0.25 inches.

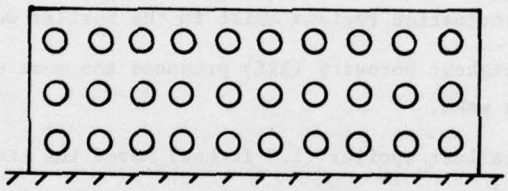

Constant Hole Size

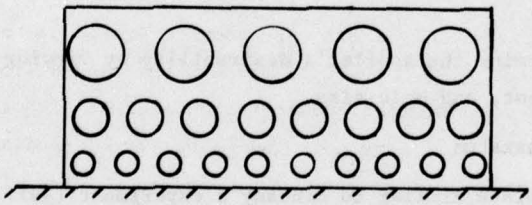

Variable Hole Size

Figure 18. Spoiler Hole Geometry

3. Test Velocities

All spoilers were tested at Mach numbers of 0.37, 0.48, and 0.71.

4. Conclusions

a. Thicker spoilers (0.25 inches) hinder the permeability of the flow through the holes because of boundary layer growth within the holes.

b. Low porosity spoilers (less than 10%) approach the wake pattern of a solid spoiler.

c. The highest porosity (41%) with the smallest holes (0.125 inch) had the most uniform flow in the near wake.

d. Variable hole size produced undesirable jetting and increased shear layers in the wake.

e. Varying the Mach number had little overall effect on the general flow characteristics; however, the higher Mach numbers did produce stronger wake motion.

C. Tower's Experiment

Performed by Michael M. Tower (Ref. 22) from 1 September 1976 to 15 December 1976.

1. Purpose

To reduce the vortex flow within a cavity by placing spoilers of various geometries circumferentially around the cavity opening.

2. Test Apparatus

The base plates of the previous experiments by Lindsay and Hatfield were modified by drilling a square and circular cavity of variable depth. The purpose of the three-by-three-inch-square cavity was to simplify the flow characteristics by presenting the flow with a two-dimensional spoiler rather than a circular spoiler used with the three-and-a-half-inch circular cavity. The cavity depth could be varied from zero to two-and-a-half inches in half-inch increments.

The perforated spoilers were mounted around the cavity opening. They had thicknesses of 0.0625 and 0.125 inches and ranged from 0.125 to 1 inch in height. The perforation geometry consisted of circular holes or vertical slots as shown in Figure 19. The holes varied in diameter from 0.0625 to 0.25 inches and were arranged in two to five rows. The slotted fence had gaps and slats of 0.0625 to 0.25 inches. The spoiler porosities varied from 21 to 50 percent.

Oil droplets were used to study the flow characteristics.

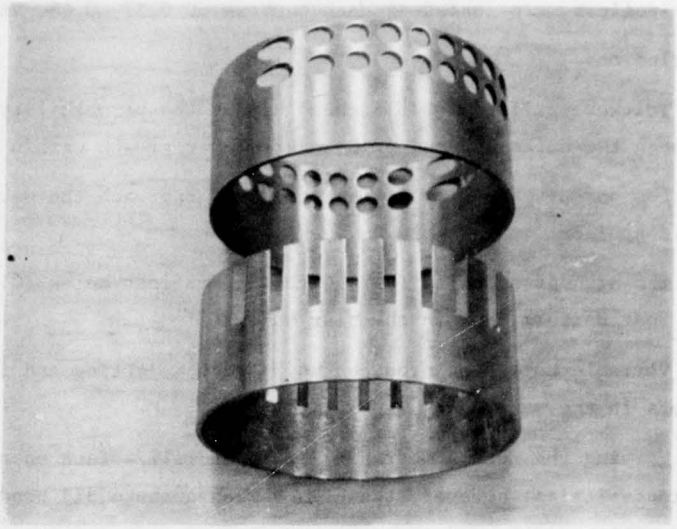

Figure 19. Circular Spoiler Geometry

3. Test Velocities

All models were tested at Mach numbers of 0.48 and 0.71.

4. Conclusions

a. A full (360°) circumferential spoiler produced essentially the same cavity flow results as a spoiler that was placed only around the cavity's front half.

b. Mach number had little effect on the general flow pattern.

c. The deeper the cavity the less the flow activity on the bottom.

d. Reverse flow on the cavity bottom was apparent in all tests indicating the presence of a vortex within the cavity.

e. Circumferential spoilers with non-porous side plates eliminated tip vortices.

f. For a given porosity, many small openings produced more uniform cavity flow than did a spoiler with larger holes or slots.

g. Flow characteristics within the cavity are very similar for both the circular and square cavities.

h. Porosities of 20 to 40 percent produced the least turbulent motion within the cavity.

i. Typical results are shown in Figures 20 and 21.

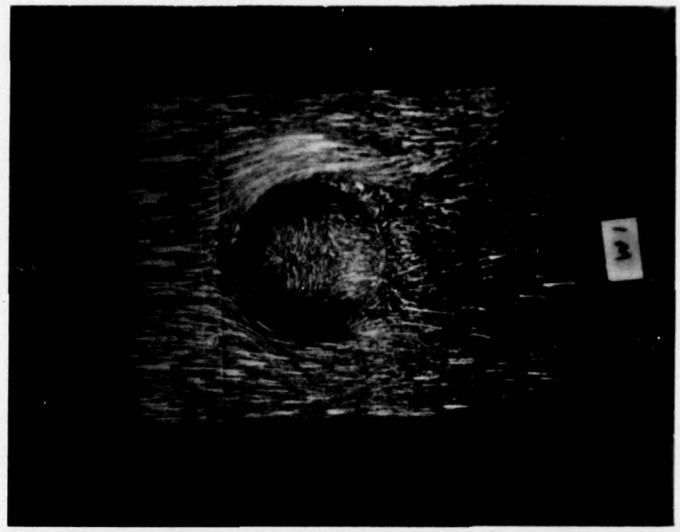

M = 0.71

Cavity
Depth = 0.6 inch

Spoiler
Height = .38 inch

Spoiler
Porosity = 50%

Figure 20. Circular Cavity with Circumferential Slotted Spoiler

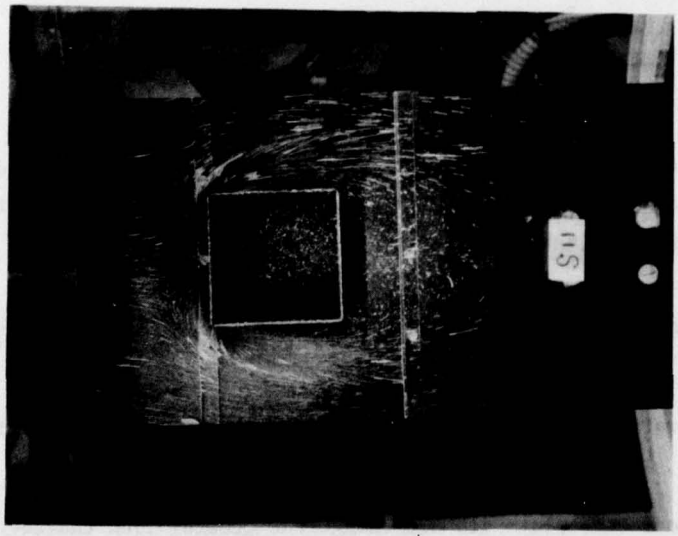

M = 0.71

Cavity
Depth = .6 inch

Spoiler
Height = 1 inch

Spoiler
Hole Dia. = 1/8 inch

Porosity = 21%

Figure 21. Square Cavity with Peripheral Porous Spoiler

D. Wurst's Experiment

Performed by Stephen G. Wurst (Ref. 23) from 1 September 1976 to 15 December 1976.

1. Purpose

To examine the cavity flow behind a porous spoiler mounted on a half cylinder.

2. Test Apparatus

Wurst's experiment is similar to the previously described experiments, except for the base plate which is formed by a half cylinder (see Figure 22).

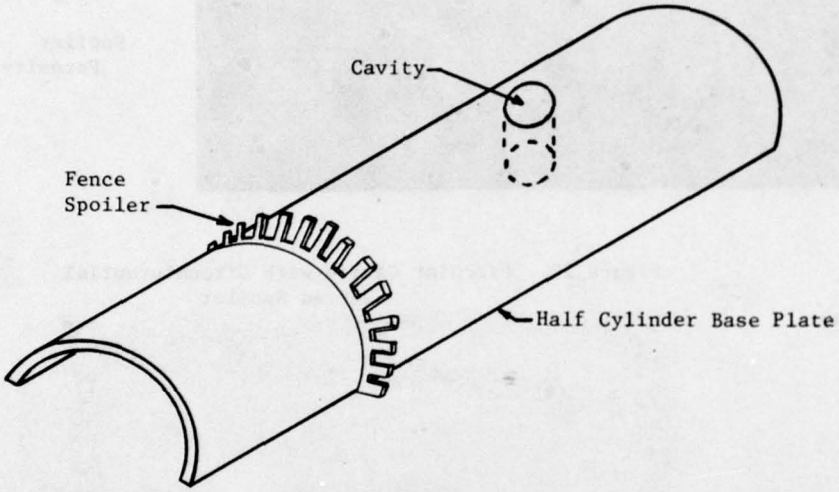

Figure 22. Wurst's Experimental Model

The spoiler was of the picket fence type with porosities of 39, 42, and 71 percent. Two heights were tested, 0.625 and one inch. Also, two arc lengths were used, a 60° length and a full 180° arc length across the base plate.

The cavity was placed in the predicted spoiler-wake stagnation region. The cavity was one-and-a-half inches in diameter and one-inch deep.

3. Test Velocities

All test configurations were run at Mach numbers equal to 0.48 and 0.71.

4. Conclusions

a. The cylindrical base plate did not change the general flow characteristics in the spoiler's wake.

b. The location and geometry of spoiler is a factor in the location and size of the wake stagnation region.

c. Low porosity combined with short spoiler height created a stagnation region farther upstream than any other combination.

d. The width of the stagnation region is a function of the arc length of the spoiler.

e. The general flow characteristics at Mach 0.48 and Mach 0.71 were not significantly different.

f. A typical result of flow visualization is shown in Figure 23.

E. Foister's Experiment

Performed by James W. Foister (Ref. 24) from 1 January 1977 to 15 May 1977.

1. Purpose

To investigate the flow patterns in and around a cavity with porous spoilers of various heights and porosities mounted upstream of the cavity on a cylindrical base plate.

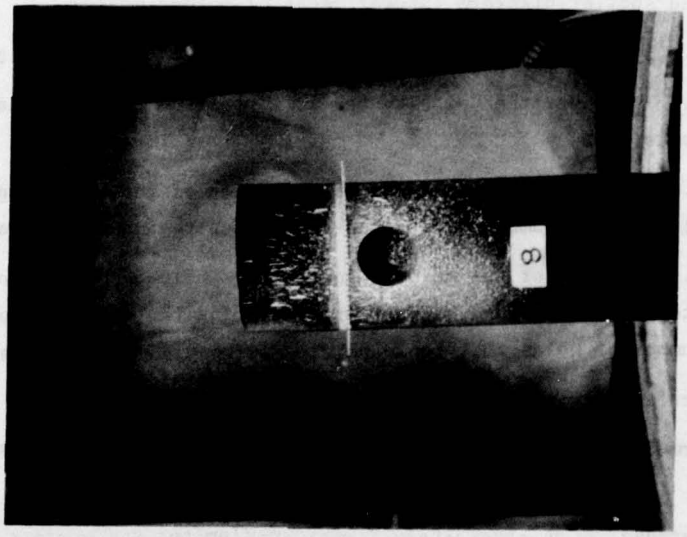

Figure 23. Cylindrical Base Plate Results for M = 0.48 and 42% Porosity

30

2. Test Apparatus

The test apparatus was the same as that used by Wurst except for the spoilers. The geometry was of two types, the picket fence type and the porous hole type. The porosity was varied from 0.156 to 0.504.

Spoilers with holes varied from one row of holes to three rows. Hole sizes were of 0.125, 0.25 and 0.5 inches. Two spoiler heights were tested, 0.625 and one inch.

The cavity was again placed in the spoiler wake stagnation region. The cavity was one-and-a-half inches in diameter and one-inch deep.

3. Test Velocities

All test geometries were run at Mach numbers of 0.48 and 0.71.

4. Conclusions

a. The picket fence spoiler bleeds air into the wake in the form of vertical sheets causing shear layers only in the vertical plane, whereas the spoiler with holes bleeds air into the wake in individual jets causing shear layers vertically as well as horizontally.

b. The general flow characteristics within the cavity are independent of the spoiler planform (picket fence or porous holes).

c. Spoiler porosity is a major influence on the flow within the cavity.

d. The lower the porosity the more upstream the wake stagnation region moves.

e. The Mach number affects the location of the wake stagnation region. Higher Mach numbers drive the stagnation region downstream.

f. The spoiler height only indirectly influenced the spoiler-wake-stagnation region by directly influencing the allowable porosity by the number of holes that could physically be drilled in the spoiler.

F. Thacker's Experiment

Performed by Thomas H. Thacker (Ref. 25) from 1 September 1977 to 15 December 1977.

1. Purpose

To investigate the pressure distribution within a circular cavity behind a porous spoiler by the use of static pressure ports attached to a manometer bank. Flow visualization by oil traces was also used.

2. Test Apparatus

The cavity and spoiler models were the same used by Tower in his experiment with the addition of five static pressure ports drilled into the cavity for static pressure measurements (see Figure 24). Each static port was connected to a manometer where the pressure was visually read during the wind tunnel test.

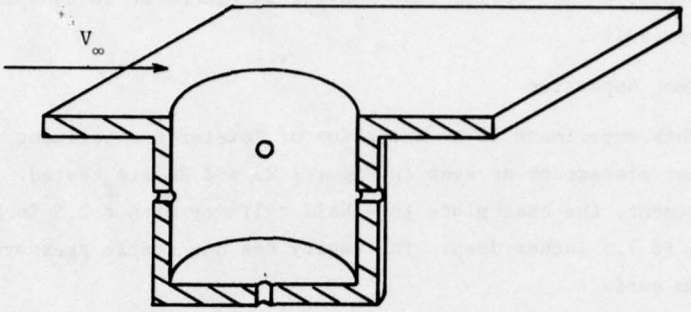

Figure 24. Cross-Sectional View of Cavity with Static Pressure Ports

Spoiler heights ranged from 5/16 to one inch and varied in porosity from 20 to 34 percent. Some of the spoilers only covered the front half of the cavity, whereas others completely circumvented the cavity.

3. Test Velocities

All test geometries were run at Mach numbers of 0.48 and 0.71.

4. Conclusions

a. Pressure gradients between static pressure ports were found between the range of 0.02 and 1.0 pounds per square inch.

b. The constant porosity hole spoiler produced less pressure gradients than the picket fence spoiler.

c. The constant porosity hole spoiler with three rows of 0.125 inch holes, 20 percent porosity, and covering only the front 140 degrees of the cavity was the best spoiler geometry tested for limiting pressure gradients.

d. Increasing the Mach number from 0.48 to 0.71 increased the difference between the maximum and minimum static pressure measured between ports in all cases.

G. Diamond's Experiment

Performed by Dennis J. Diamond (Ref. 26) from 1 September 1977 to 15 December 1977.

1. Purpose

To investigate the flow and static pressure within a circular cavity. The cavity in one case is surrounded by a circumferential porous spoiler, and in the other, a flat cylindrical spoiler is placed at various locations upstream of the cavity.

2. Test Apparatus

This experiment is an extension of Foister's experiment (Ref. 24). Two spoiler placements as seen in Figures 25 and 26 are tested. As in Foister's experiment, the base plate is a half cylinder with a 2.5 inch diameter cavity which is 1.5 inches deep. The cavity has one static pressure port on the bottom surface.

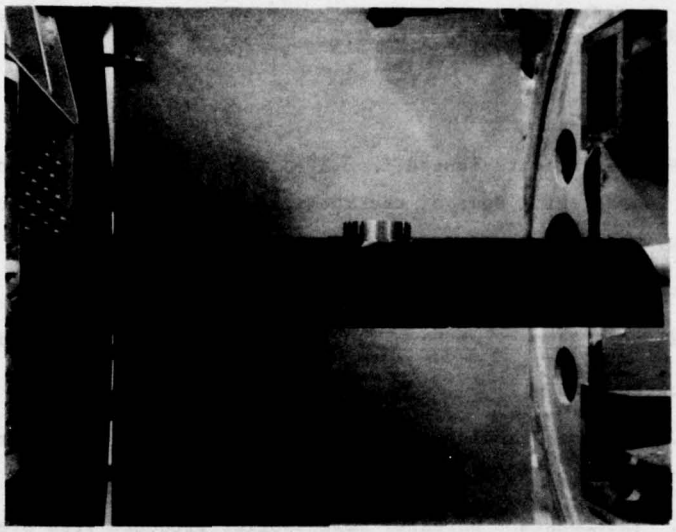

Figure 25. Circumferential Porous Spoiler Around Cavity

The circumferential porous spoilers, as seen in Figure 26, were of the picket fence and the constant porous holes types. Porosity was either 0.29 or 0.49. The spoilers ranged in height from 0.125 to 0.5 inches.

The cylindrical spoilers, as seen in Figures 26 and 27, had two rows of holes with diameters from 0.125 to 0.25 inches. The porosity was varied over

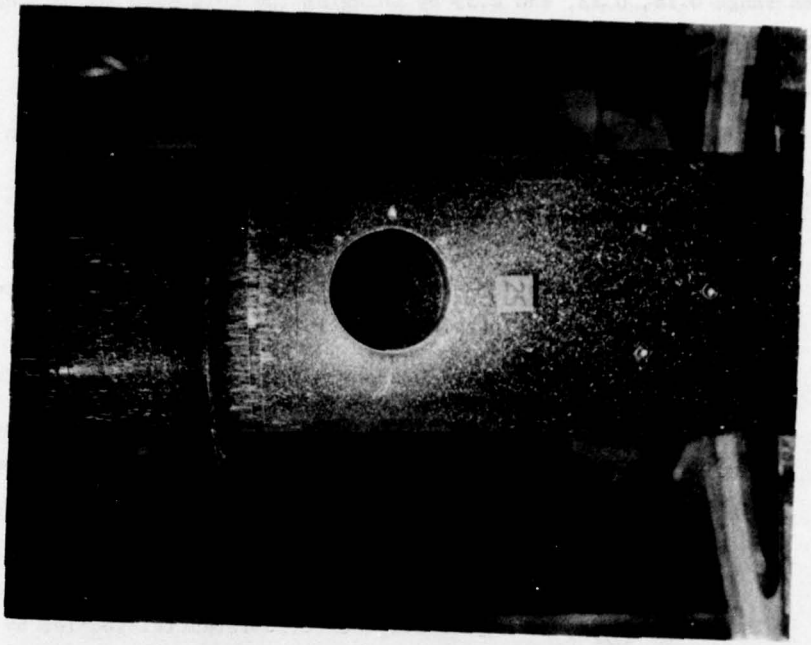

Figure 26. Cylindrical Porous Spoiler Placed Upstream of Cavity

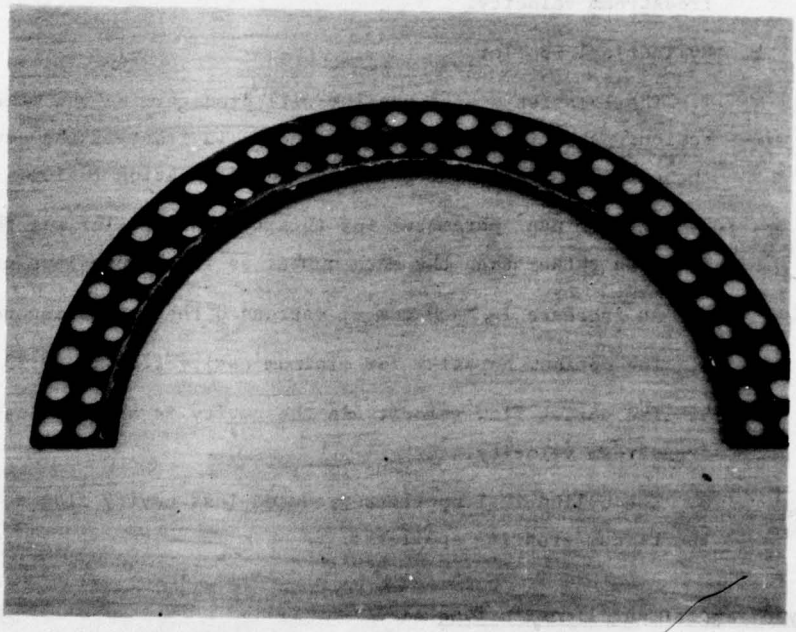

Figure 27. Cylindrical Porous Spoiler

the range 0.16, 0.23, and 0.39 by changing the hole size and placement. The spoilers were all 0.875 inches in height.

3. Test Velocities

All model geometries were tested at Mach numbers of 0.48 and 0.71.

4. Conclusions

a. Circumferential Spoiler

1. As the height of the spoiler is increased from 0.125 to 0.5 inches, the flow activity within the cavity is decreased.

2. The lower porosity, 0.29, yielded less cavity flow activity.

3. The Mach number is the dominant parameter affecting the flow inside the cavity. As the Mach number increases, so does the flow activity in the cavity.

4. Static pressure measurements for the circumferential spoilers are lower than for the cylindrical spoilers, indicating the flow velocity in the cavity is higher for the circumferential spoiler by about 30 percent.

5. The vortex flow velocity in the cavity is about 68 percent of the freestream velocity.

b. Cylindrical Spoiler

1. The location of the spoiler will predetermine the wake stagnation region. A spoiler position 3.5 inches in front of the cavity allowed the cavity to be in the center of the stagnation region.

2. The dominant parameter for this type of spoiler was the spoiler location rather than the Mach number as in the previous case.

3. An increase in Mach number decreased the stagnation region area.

4. The optimum porosity for minimum cavity flow was 0.23.

5. The vortex flow velocity in the cavity is about 45 percent of the freestream velocity.

6. The cylindrical spoilers produced less cavity flow activity than the circumferential spoilers.

V. Summary of Experimental Conclusions

The following list of conclusions is drawn from the experimental tests performed at the Academy which seem particularly relevant to the analysis of the laser cavity and exhaust ports on the Airborne Laser Laboratory.

A. Stagnation regions can be produced behind porous spoilers.

B. Varying the Mach number has little effect on the general flow characteristics within the cavity.

C. Higher Mach numbers drive the stagnation region downstream of the spoiler.

D. Porosities of 20 to 40 percent yield the most uniform flow in the spoiler wake.

E. Thinner spoilers allow more permeability than thicker spoilers of the same porosity.

F. A full (360°) circumferential spoiler produces essentially the same cavity flow results as a spoiler placed only around the cavity's front half.

G. For a given porosity, many small openings produce more uniform cavity flow than a spoiler with larger holes or slots.

H. The picket fence spoiler bleeds air into the wake in the form of vertical sheets causing shear layers only in the vertical plane, whereas the spoiler with circular holes bleeds air into the wake in individual jets causing shear layers vertically as well as horizontally.

I. Pressure gradients within the cavity range between 0.02 and 1.0 pounds per square inch.

J. Cylindrical spoilers, see Figure 27, produce the lowest vortex velocities within the cavity.

K. The vortex flow velocity within the cavity is about 45 percent of the free-stream velocity.

References

1. Rayleigh, J. W. S. The Theory of Sound. Vol. 2. London: Macmillan, 1896, p. 412.

2. Covert, E. E. "An Approximate Calculation of the Onset Velocity of Cavity Oscillations." AIAA Journal, Vol. 8 (December 1970), 2189-94.

3. Nyborg, W. L. "Acoustical Characteristics of Jet-Edge and Jet-Edge-Resonator Systems." Journal of the Acoustical Society, Vol. 24 (May 1958), 283.

4. Squire, H. B. "Note on the Motion Inside a Region of Recirculation (Cavity Flow)." Journal of the Royal Aeronautical Society, Vol. 60 (March 1956), 203-205.

5. Pan, F. and A. Acrivos. "Steady Flows in Rectangular Cavities." Journal of Fluid Mechanics, Vol. 28, Part 4 (June 1967), 643-655.

6. O'Brien, V. "Closed Streamlines Associated with Channel Flow Over a Cavity." Physics of Fluids, Vol. 15 (December 1972), 2089.

7. Mehta, V. B. and Z. Lavan. "Flow in a 2-D Channel with a Rectangular Cavity." Journal of Applied Mechanics, ASME-36 (December 1969), 897-907.

8. Maull, D. J. and L. F. East. "Three Dimensional Flow in Cavities." Journal of Fluid Mechanics, Vol. 16 (August 1963), 621.

9. Bilanin, A. J. and E. E. Covert. "Estimation of Possible Excitation Frequencies for Shallow Rectangular Cavities." AIAA Journal, Vol. 11 (March 1973), 347-351.

10. Mills, R. D. "On the Closed Motion of a Fluid in a Square Cavity." Journal of the Royal Aeronautical Society, Vol. 69 (February 1965), 116-120.

11. Roshko, A. Some Measurements of Flow in a Rectangular Cutout. NACA TN-3488, August 1955.

12. Blokhintsev, D. I. Acoustics of a Non-Homogeneous Moving Medium. NACA TM-1399, 1946.

13. Krishnamuity, K. Acoustic Radiation From Two Dimensional Rectangular Cutouts in Aerodynamic Surfaces. NACA TN-3487, 1955.

14. Rossiter, J. E. Wind Tunnel Experiments on the Flow Over Rectangular Cavities at Subsonic and Transonic Speeds. RAE TR-64037, 1964.

15. Harris, C. M. and C. E. Crede. Shock and Vibration Handbook. Vol. 3. New York: McGraw-Hill, 1961.

16. Reference Data for Radio Engineers. 5th ed. Indianapolis, IN: Howard W. Sams & Co., Inc., 1968.

17. Buell, D. A. "Airloads Near the Open Port of a One-Meter Airborne Telescope." AIAA Paper 75-71, presented at the AIAA Aerodynamic Acoustic Conference, San Diego, California, January 1975.

18. Buell, D. A. An Experimental Investigation of the Airflow Over a Cavity with Antiresonance Devices. NASA TN-D-6205, March 1971.

19. Castro, I. P. "Wake Characteristics of Two-Dimensional Perforated Plates Normal to an Airstream." Journal of Fluid Mechanics, Vol. 46 (1971), 607.

20. Lindsay, C. L. "An Investigation of the Flow Through Perforated Spoilers." Aeronautics Department 499 Report, USAF Academy, Colorado, December 1975.

21. Hatfield, D. N. "An Investigation of Air Flow Through Straight and Circular Perforated Spoilers." Aeronautics Department 499 Report, USAF Academy, Colorado, May 1976.

22. Tower, M. M. Flow Visualization in Square and Circular Cavities Behind a Porous Spoiler. USAFA-DFAN-TN-1. USAF Academy, Colorado, Aeronautics Department, December 1976.

23. Wurst, S. G. "An Investigation of the Flow Field Disturbances Created by Circumferential Porous Spoilers." Aeronautics Department 350 Report, USAF Academy, Colorado, December 1976.

24. Foister, J. W. "An Investigation into the Flow Effects of Porous Spoilers of Porosities from 0.504 to 0.156." Aeronautics Department 350 Report, USAF Academy, Colorado, May 1977.

25. Thacker, T. H. "An Investigation of Circular Perforated Spoilers for Use on the Airborne Laser Laboratory." Aeronautics Department 350 Report, USAF Academy, Colorado, December 1977.

26. Diamond, D. J. "An Investigation of Flow Field and Cavity Flow Effects of Different Types of Porous Fences." Aeronautics Department 499 Report, USAF Academy, Colorado, December 1977.

PHYSICS OF A HOT AIR BALLOON

John P. Jackson*

Abstract

This paper discusses the physics and governing equations for a hot air balloon. The equations for lift, drag, solar effects, heat transfer, and dimpling are derived from basic principles and demonstrative calculations are made for a standard hot air balloon. Where applicable, actual flight test data are used to aid in analysis.

I. Introduction

Lighter-than-air flight is much older than heavier-than-air flight. There is good reason for this: lighter-than-air flight is far simpler both scientifically and technologically. Yet, surprisingly, the physical principles of aerostatic systems do not seem to be as widely known as aerodynamic systems, even though the physics of the latter is far more complex.

This paper dealing with one kind of aerostatic system, a hot air balloon, has been written for several reasons. First, the author, in believing that the study of aerostatics is an excellent primer to the study of aerodynamics, wishes to make some of his calculations available to instructors at the Air Force Academy. And second, hot air ballooning, a popular sport, has been part of cadet flying activities and hence such a paper might be worthwhile for supplementing such a program.

The author holds a commercial hot air balloon license and, though presently inactive in the sport, was a co-organizer of a hot air balloon club in Albuquerque, New Mexico; co-authored a book on hot air ballooning (Ref. 1); and performed some flight measurements of his own balloon which form the bases for the calculations in this paper. The author is indebted to his former ballooning partner, Lt Col Rudolph Dichtl and to Aerodynamicist Capt Eric Jumper for his support of these calculations.

Throughout this paper, reference will be made to what the author calls a "Standard Hot Air Balloon" whose characteristics are specified in Table 1. This will allow all calculations performed herein to be standardized to a balloon with these parameters. To determine the flight parameters of any other balloon configuration, one can simply and straightforwardly proceed to scale the results by using the appropriate physical equations. All calculations will be performed in the more familiar but awkward "British" system of units and wherever appropriate the result in the metric system will also be reported. The reason for this is that balloon manufacturers still use the "British" system to specify their balloon parameters and, therefore, these are usually the more familiar to the balloon enthusiast.

---

*Captain, USAF, Associate Professor of Physics, DFP

Table 1

STANDARD HOT AIR BALLOON

V	53,000 ft^3	1.50×10^9 cm^3
D	46.6 ft	1.42×10^3 cm
T_i	137°F	331.4°K
T_o	51°F	283.6°K
F	4×10^6 BTU/hr	1.17×10^{13} ergs/sec
P_o	14.7 lb/in	1.10×10^6 dynes/cm^2
α_s	.5	
α_{IR}	.27	
ϵ_b	.9	

The reader is referred to the list of symbols at the end of this paper and, as such, symbols may not be defined in the text although many are.

II. Aerostatics of Hot Air Ballooning

To many people who watch a balloon quietly drifting on an early morning flight, it seems, somehow, that the balloon really shouldn't be there because it appears to violate that well established principle popularly ascribed to Newton -- "What goes up, must come down." Perhaps the reason the floating balloon looks so much out of place is that we psychologically turn around in our minds what is reality and what is the absence of it. For example, consider the two pictures in Figure 1. In side A, we see a picture

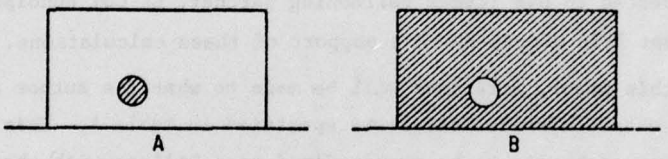

Figure 1. Two Ways of Looking at a Balloon

showing how we normally see a balloon--a ball apparently suspended in free space. All other objects which we see fall towards earth but this one has the uncanny ability to rise. However, if we could, for a moment, put on a special type of visual aid which would allow us to see mass density, our view would change completely and everything would make sense again. For then, we would see things as in side B where the balloon would now appear as a hole, a vacancy in a dense sea of air. This hole would appear

to move upward only because the dense air, which is what possesses weight, falls toward the ground as any massive object must. We have no trouble reconciling the motion of the hole for its movement, we see, merely reflects the response of the dense fluid to its own gravitational weight. The air fluid simply tries to "work" the hole or bubble up as high as it can until some stable equilibrium is achieved.

So if we realize that Newton's Law applies to the surrounding air and not to a hole in that gaseous medium, we should have no trouble understanding that a balloon is not in violation of that principle. Of course, any weight which is attached to that hole such as the balloon fabric, gondola, passengers, and even any air which might be occupying the volume of the hole is subject to Newton's Law; but these will only retard the vacancy's response to the surrounding air's readjustments.

In the following sections, this basic idea will be described by equations of physics.

A. Archimedes' Principle

The lift on a hot air balloon system is based on the Law of Archimedes which states that the net upward lift, L, supporting the balloon at a fixed altitude is equal to the weight of air, W_o, displaced by the balloon minus the weight of air, W_i, contained in it. The following is a derivation of that law (Ref. 2).

Consider the element of fluid shown in Figure 2. In a sense, this fluid element is like a "microballoon" in that the net external aerostatic pressure must be such that it can support the weight of the "microballoon."

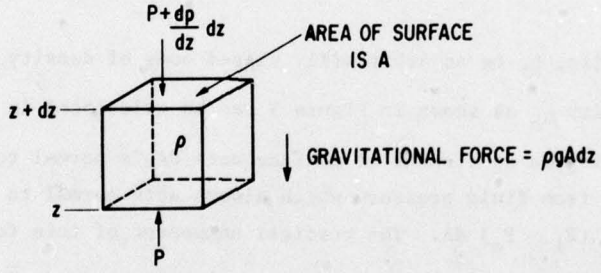

Figure 2. Fluid Element in Equilibrium

In the vertical Z-direction, the total force acting on the fluid element by pressure from adjacent fluid elements above and below is A [P - (P + d P)] = -AdP. If the element is at rest, then this force must be equal to the weight, ρ g AdZ, of the element. This is expressed in the relation

$$\frac{d\,P}{d\,Z} = -\rho g \qquad (1)$$

called the Equation of Aerostatic Equilibrium. This shows that gravity induces a slight pressure gradient in an otherwise homogeneous and uniform static fluid.

Eqn (1) can be integrated over distances where ρ does not change appreciably to yield

$$P(z) = \bar{P} - \rho g Z \tag{2}$$

where the arbitrary constant $\bar{P}$ is the value of pressure, P, at Z=0.

This equation with constant ρ is valid in calculating the net lift on a hot air balloon, i.e., Archimedes' Principle, since over the height of a balloon (much smaller than the scale height of the atmosphere), ρ changes negligibly.

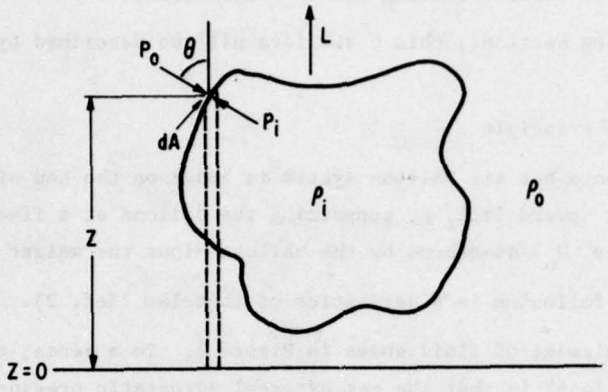

Figure 3. Calculation of Buoyant Forces on Arbitrarily Shaped Body

The upward lift, L, on an arbitrarily shaped body of density ρ_i immersed in a reservoir of density ρ_o as shown in Figure 3 can be calculated in the following manner. The net force acting on an element of surface area dA is normal to that element (because this force arises from fluid pressure which always acts normal to any arbitrary surface) and has magnitude $(P_i - P_o)\,dA$. The vertical component of this force, dL, is $(P_i - P_o)\,dA\ \cos\theta$. From Eqn (2), $dL = (\rho_o - \rho_i)\,g\,Z\,\cos\theta dA + (\bar{P}_i - \bar{P}_o)\,\cos\theta dA$, and

$$L = \int dL = \int_{\substack{\text{closed}\\ \text{surface}\\ \text{area}}} (\rho_o - \rho_i)\,gZ\,\cos\theta dA \tag{3}$$

where the term containing $(\bar{P}_i - \bar{P}_o)$ integrates to zero. This can be easily seen by noting: $\int (\bar{P}_i - \bar{P}_o)\,\cos\theta dA = (\bar{P}_i - \bar{P}_o) \int \cos\theta dA = (\bar{P}_i - \bar{P}_o) \int_{\substack{\text{closed}\\ \text{surface}\\ \text{area}}} \text{vertical projection of surface element} = 0$.

Now, $Z\,\cos\theta\,dA$ is the volume element, dV, of a tube of cross-sectional area $|\cos\theta\,dA|$ extending from a horizontal plane located at Z = 0 to the surface element, dA. Eqn (3) can be integrated with respect to dV (noting that dV has the same sign as $\cos\theta$) resulting in an integration over the net volume of the body:

$$L = g \oint_{\text{volume}} (\rho_o - \rho_i)\, dV \quad . \tag{4}$$

This is Archimedes' Law; $g \oint \rho_o\, dV$ is the weight, W_o, of fluid displaced by the body and $g \oint \rho_i\, dV$ is the weight, W_i, of the fluid contained. The reason for the buoyant force is now clear: if the pressure on the outside of the body decreases more rapidly with altitude than the pressure inside of the body, then there is a net upward force and the body is "buoyed up," as it were.

B. Lift Equation for a Hot Air Balloon

With ρ_o and ρ_i, the constant densities of air outside and inside the hot air balloon of volume, V, Eqn (4) becomes

$$L = (\rho_o - \rho_i)\, g\, V \quad . \tag{5}$$

These densities are related to pressure and absolute temperature outside and inside by the air equation of state,

$$P \approx B\, T\, \rho \quad . \tag{6}$$

In a hot air balloon, the mouth at the bottom of the envelope bag is open to allow insertion of hot air from the burner just below it. Thus, at the open mouth, the pressure inside must equal the pressure outside. According to Eqn (2) the pressure inside (and outside) the balloon cannot vary more than ρgD where D is the balloon diameter. Since the ratio $\rho gD/\bar{P} \simeq 10^{-5}$, it is easily seen that the pressure inside (and outside), P_i (and P_o), is very nearly constant. However, as has been pointed out above, this slight pressure variation when integrated over the surface of the balloon is responsible for the balloon's lift. Since the pressures and densities (inside and outside) are essentially constant over the height of a balloon, then according to Eqn (6) the temperature must also be very nearly constant within the balloon envelope (and outside of it). Since P_i and P_o are equal, it follows from Eqn (6) that $\rho_o T_o = \rho_i T_i$ and Eqn (5) becomes the lift equation for a hot air balloon:

$$L = \rho_o\, V\, g\, \left(1 - \frac{T_o}{T_i}\right) \quad . \tag{7}$$

This relation implies that the lift is zero if $T_i = T_o$. If, however, $T_i \gg T_o$, then $L = \rho_o V g$, the maximum possible lift for a hot air balloon system.

For the standard balloon, the lift equation is plotted in Figure 4 as a function of T_o and T_i.

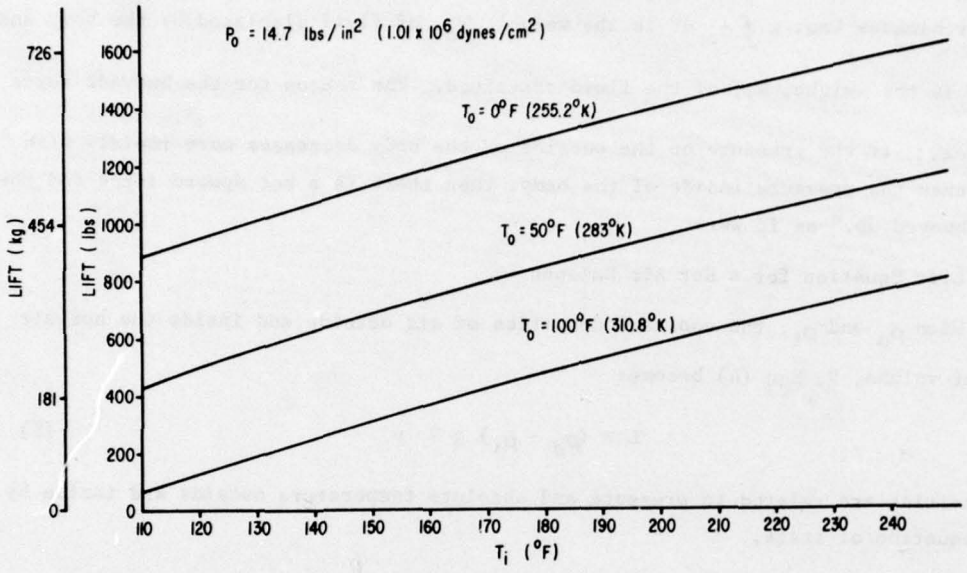

Figure 4. Lift of a Standard Hot Air Balloon Versus Temperature of Air Inside

III. Thermodynamics of Hot Air Ballooning

A. Energy Considerations of a Hot Air Balloon.

Within a hot air balloon of volume, V, the total amount of thermal energy E (measured by the internal temperature, T_i, and density, ρ_i) is given by the expression

$$E = C_p \rho_i V T_i \tag{8}$$

where C_p is the specific heat at constant pressure. A fundamental thermodynamic principle of any hot air balloon system of constant volume which can freely transfer air between the inside and external environments at constant altitude is that, regardless of temperature, E always remains constant in time; that is,

$$\frac{dE}{dt} = 0 \quad . \tag{9}$$

This can easily be seen from the requirement that, except for very small vertical gradients (induced by gravity - see Eqn (2)), the pressures inside and outside, P_i and P_o, are very nearly the same. This implies that the density and temperature vary inversely with one another so that P_i is always very close in magnitude to P_o. For an ideal gas,

$$P = (\gamma - 1)\, e \tag{10}$$

where e is the energy/volume and γ is the ratio of specific heats at constant pressure and volume. Therefore, for a hot air balloon of constant volume, V, the internal pressure's being nearly uniform implies, by Eqn (10), that the internal energy density, e = E/V, is also. Hence,

$$E = P_o\, V/(\gamma - 1) = \text{const.} \tag{11}$$

When no changes in altitude are occurring, $P_o \simeq$ const. and Eqn (9) follows immediately. When the balloon is changing altitude, the total energy, E, changes in proportion to the vertical velocity. This effect will be considered later.

Thus, the purpose of adding heat to a balloon envelope in flight is not to increase its thermal energy content but to reduce the density of air inside (by air flow exiting through the mouth) which, according to Eqn (8), can only be accomplished by a corresponding increase in temperature. By making the air inside the balloon less dense, the balloon becomes buoyant as explained in the previous section.

In flight, a hot air balloon exchanges energy with its environment and receives energy from its burner system. This is depicted in Figure 5.

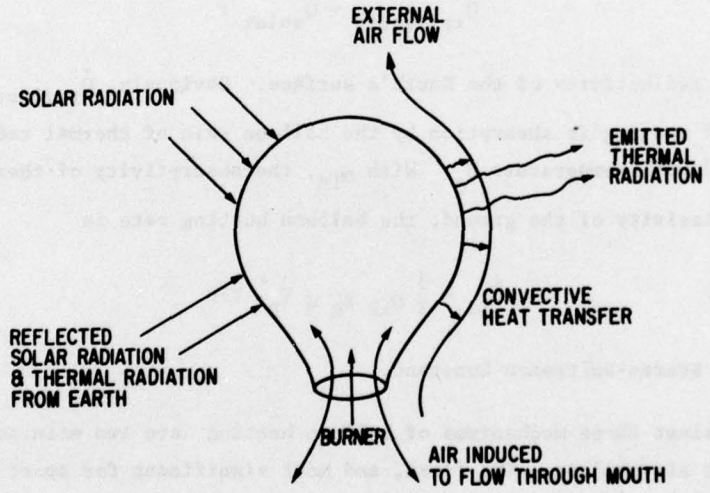

Figure 5. Energy Changes Within a Hot Air Balloon
Sources of Heating: Flight Burner, Absorption of Solar and Terrestrial Radiation
Sources of Cooling: Thermal Radiation, Heat Conduction from Balloon

As energy is lost or gained from within the envelope, air is passed through the mouth (to maintain pressure equilibrium) which changes the density of the contained air and hence the lifting force of the balloon.

The various modes of energy exchange are discussed below.

The most obvious energy exchange mechanism is from the flight burner which supplies heat at a rate

$$\dot{Q}_{burner} = F\ N \tag{12}$$

where F is the power output of the burner specified by the manufacturer (BTU/hr or erg/sec) and N the fraction of time the burner is on in order to compensate for heat losses from the balloon.

Other sources of balloon heating are as follows (References 3, 6, and 7). First, and most important for normal-sized sport balloons, is direct absorption of the solar radiative flux (power/area), S. If the absorptivity for this radiation by the balloon fabric is γ_s, then the power absorbed is

$$\dot{Q}_{solar} = \frac{3}{2}\ \gamma_s S\ V/D \tag{13}$$

where D is the balloon diameter. The factor 3/2 V/D is simply the cross-sectional area of the balloon which intercepts the parallel solar flux. A second source of balloon heating is also from the sun but by diffuse reflection from the earth's surface. In this case the heating rate is

$$\dot{Q}_{reflected} = \dot{Q}_{solar}\ r \tag{14}$$

where r is the reflectivity of the Earth's surface. Obviously, $\dot{Q}_{reflected} \leq \dot{Q}_{solar}$. A third source of heating is absorption by the balloon skin of thermal radiation emitted from the ground with temperature T_g. With α_{IR}, the absorptivity of thermal radiation and ϵ_g, the emissivity of the ground, the balloon heating rate is

$$\dot{Q}_{IR} = \frac{3}{2}\ \alpha_{IR}\ \epsilon_g\ \sigma\ T_g^4\ V/D \tag{15}$$

where σ is the Stefan-Boltzmann Constant.

Acting against these mechanisms of balloon heating are two main sources of heat loss from a hot air balloon. The first, and most significant for sport balloons, is the emission of thermal radiation given by

$$\dot{Q}_{thermal} = -6\ \epsilon_b\ \sigma\ T_s^4\ V/D \tag{16}$$

where T_s is the skin temperature of the balloon fabric and ϵ_b is the balloon emissivity; this loss occurring over the entire surface of the balloon is expressed in terms of the ratio V/D as in the previous terms. According to Reference 3, T_s varies only a few degrees less than the inside temperature of the balloon, so $T_s \simeq T_i$.

The other loss mode is by heat conduction to the surrounding air. Except when the balloon is moving relative to the surrounding air (such as in rising or encountering a wind shear in flight, for example), the conductive heat loss is by free convection where air that is heated is induced to flow over the surface thereby removing heat emanating from the balloon skin. A simple formula for the heat power loss by free convection is (Ref. 10)

$$\dot{Q}_{conv} = -6H_o\ (T_s - T_o)\ V/D \tag{17}$$

where H_o, the heat transfer coefficient, is given by

$$H_o = h\left(\frac{T_s - T_o}{D}\right)^{1/4} \tag{18}$$

where h is a constant of proportionality given in the list of symbols. Eqn (18) comes from consideration of free convection around a cylinder of diameter D but with the coefficient h modified so as to approximate the spherical geometry of the balloon. However, when a hot air balloon is in the presence of an external air flow, the nature of the convective heat transfer is termed "forced" and Eqn (17) remains valid if the heat transfer coefficient is modified to the forced value (Ref. 10)

$$H_o = Nu\ \lambda/D \tag{19}$$

where λ is the thermal conduction coefficient at temperature $(T_s + T_o)/2$ and the Nusselt Number, Nu, is given by

$$Nu = C\ (Re)^{.57}\ (Pr)^{.4}\ . \tag{20}$$

In Eqn (20), C is a constant of proportionality (see list of symbols). Pr is the Prandtl Number of the air, and Re is the Reynolds Number characteristic of the flow configuration, given by

$$Re = \rho_o\ D\ v/\mu \tag{21}$$

where μ is the viscosity of the air given by

$$\mu = \lambda\ Pr/C_p\ . \tag{22}$$

Eqns (17) thru (22) take into account that the heat transfer by thermal conduction occurs over a boundary layer set up over the balloon envelope either by free or forced air flow.

In the limit of zero air velocity, v, the Reynolds Number, Re, goes to zero implying that the heat transfer for forced convection vanishes. However, before that limit is reached, the Eqn (19) becomes inapplicable giving way to Eqn (20) since the heat transfer is accomplished by free convection at zero external air flow velocity.

The final mode of energy transfer into the balloon volume is by the passing of air (which contains thermal energy of its own) through the mouth. This particular mechanism of energy exchange is different from those discussed previously in that it depends directly upon the net power loss or gain rates of the above-mentioned mechanisms of heat transfer. Clearly this must be so; according to Eqn (9), there is no overall change in the heat content, so the rate of energy spillage of air, $\dot{Q}_{air}$, through the mouth must balance the totality of heat transferred by the other mechanisms. That is,

$$\dot{Q}_{air} = -\dot{Q} \tag{23}$$

where

$$\dot{Q} = \dot{Q}_{burner} + \dot{Q}_{solar} + \dot{Q}_{reflected} + \dot{Q}_{IR} + \dot{Q}_{\substack{thermal \\ rad}} + \dot{Q}_{conv} \cdot$$

As mentioned before, if the balloon is changing altitude, the air inside still seeks pressure equilibrium but, in this case, the outside pressure to which the inside air pressure is trying to adjust is changing. Then dE/dt is not equal to zero but is found by differentiating Eqn (11) where now the pressure environment changes with altitude (see Eqn (11)).

$$\frac{dE}{dt} = \frac{V}{\gamma-1}\frac{dP}{dt} = \frac{V}{\gamma-1}\frac{dP}{dZ}\frac{dZ}{dt} = \left(\frac{\rho_o V_g}{\gamma-1}\right)\frac{dZ}{dt} \tag{24}$$

Thus, when a balloon is changing altitude, -dE/dt given by Eqn (24) must be added to the expression for $\dot{Q}$ given in Eqn (23). This will, by Eqn (23), modify the energy flow rate, $\dot{Q}_{air}$, into or out of the mouth of the balloon. However, the unmodified relation for $\dot{Q}$ can be used whenever dZ/dt is small enough so that |dE/dt| is sufficiently smaller than the magnitude of any of the terms comprising $\dot{Q}$ in Eqn (23).

$\dot{Q}_{air}$ can be related to the mass flow rate dm/dt induced to flow into or out of the mouth of the balloon to maintain pressure balance by

$$\dot{Q}_{air} = C_p \frac{dm}{dt} T_k \tag{25}$$

where

$$T_k = \begin{cases} T_i & \text{if flow is out of balloon; } \dot{Q} > 0 \ (\dot{Q}_{air} < 0) \\ T_o & \text{if flow is into balloon; } \dot{Q} < 0 \quad (\dot{Q}_{air} > 0) \end{cases} .$$

The transfer of mass, dm, into the balloon results in a change of internal density, ρ_i according to

$$\frac{d\rho_i}{dt} = \frac{-\dot{Q}}{C_p T_k V} . \tag{26}$$

Using Eqn (7) and (26) above, one can find the equation governing the temperature, T_i, within the balloon.

$$\frac{dT_i}{dt} = \begin{cases} \dfrac{\dot{Q} B T_i}{C_p V P_o} , & \text{if } \dot{Q} > 0 \ (\dot{Q}_{air} < 0) \\ \dfrac{\dot{Q} B T_i^2}{C_p T_o V P_o} , & \text{if } \dot{Q} < 0 \ (\dot{Q}_{air} > 0) \end{cases} \tag{27}$$

For any open hot air balloon system of constant volume, $\dot{Q}$ can be calculated by Eqn (12) thru (22) and (24). In particular, for the "Standard Hot Air Balloon" defined in Table 1, the various components of $\dot{Q}$ given in Eqn (23) are given in Figures 6 and 7.

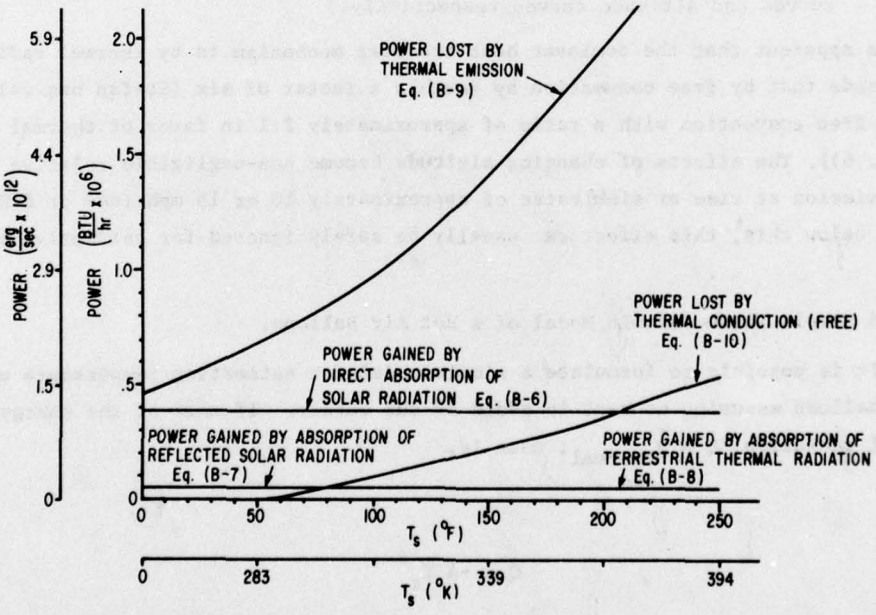

Figure 6. Power Gains and Losses by Standard Hot Air Balloon

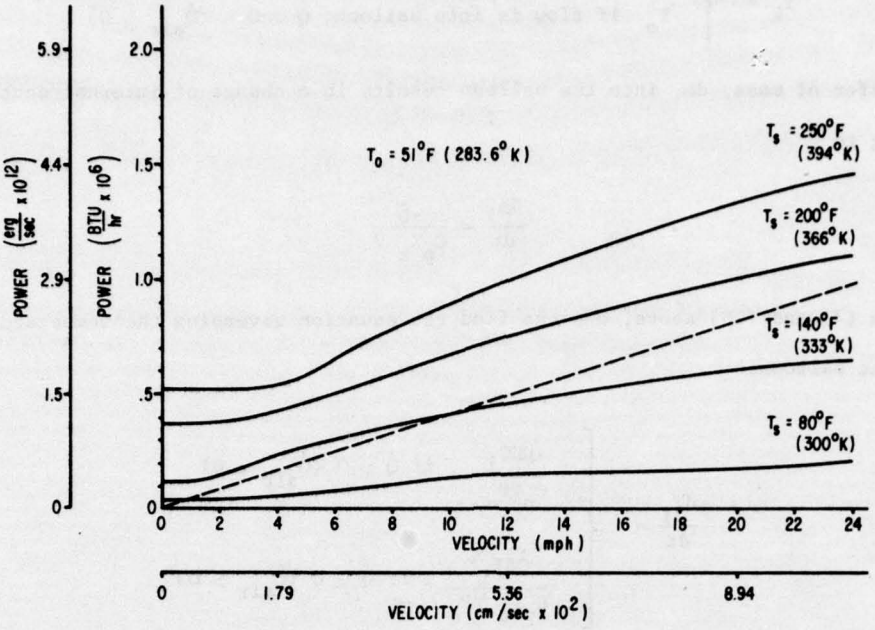

Figure 7. Power Loss by Forced Convection, Eqn (19), for Standard Hot Air Balloon (solid lines); and Power Loss (Gain) by Balloon Changing Altitude, Eqn (24), for Standard Hot Air Balloon (dashed Line)

(Velocity means wind velocity and balloon's vertical velocity for convection curves and altitude curves respectively.)

It is apparent that the dominant heat transfer mechanism is by thermal radiation which exceeds that by free convection by roughly a factor of six (Stefan has calculated a greater free convection with a ratio of approximately 2:1 in favor of thermal radiation (Ref. 6)). The effects of changing altitude become non-negligible relative to thermal emission at rise or sink rates of approximately 10 or 15 mph (447 or 670 cm/sec). At speeds below this, this effect can usually be safely ignored for estimative calculations.

B. A Simple Thermodynamic Model of a Hot Air Balloon.

It is possible to formulate a simple model for estimating temperature changes within a balloon assuming no heat is added by the burner. If most of the energy lost is by thermal radiation, $\dot{Q} \simeq \dot{Q}_{\substack{\text{thermal} \\ \text{rad}}}$; that is,

$$\dot{Q} \simeq -A\, T_s^4 \tag{28}$$

where $A = 6\ \epsilon_b\ \sigma\ V/D$. If we assume $T_s = T_i$ for simplicity (Ref. 3 indicates that $\frac{T_s - T_i}{T_i} \simeq 3\%$), and since $\dot{Q} < 0$, Eqn (27) gives

$$\frac{dT_i}{dt} = -U\ T_i^6 \tag{29}$$

where $U = \dfrac{6\ \epsilon_b\ \sigma}{D\ C_p\ \rho_o T_o^2}$.

This has the solution

$$T_i = \frac{1}{\left(5Ut + \frac{1}{T^5}\right)^{1/5}} \tag{30}$$

where T is the initial flight temperature.

For the standard balloon, $U = 1.16 \times 10^{-17}$ $(°F^5\ sec)^{-1}$ $(2.18 \times 10^{-16}$ $(°K^5\ sec)^{-1})$ which for a temperature of 105°F (313.6°K) gives $dT_i/dt = .37°F/sec$ (.21°K/sec). This agrees nicely with data taken by the author which gives $dT_i/dt = .20°F/sec$ (0.11°K/sec) at the same temperature and zero wind velocity.

According to Eqn (25), the air mass flow rate of air into the balloon is (using this simplified model)

$$\frac{dm}{dt} = \frac{6\ \epsilon_b\ \sigma V T_i^4}{DC_p\ T_o} \tag{31}$$

For the standard balloon, this amounts to dm/dt = 3.0 lbs/sec (1.36 kg/sec) or 39.4 ft^3/sec (1.12 m^3/sec). Given a mouth area of roughly 64 ft^2 (5.9m^2), the flow velocity into the mouth is .62 ft/sec (18.8 cm/sec).

For level flight, buoyancy must be maintained by keeping the flight temperature constant. This means that $\dot{Q} = 0$. Assuming again that the power loss is by emission of thermal radiation, we find that the burner must balance this loss rate so that $\dot{Q}_{burner} \simeq -\dot{Q}_{\substack{thermal \\ rad}}$ or

$$FN = A\ T_i^4 \tag{32}$$

For the standard balloon, this gives a value for N of .33 which means that the burner must be on for 33% of the time to hold level flight.

If the lift Eqn (8) is differentiated with respect to time, the following relation results.

$$\frac{dL}{dt} = \frac{g\rho_o V T_o}{T_i^2} \frac{dT_i}{dt} \tag{33}$$

Assuming dT_i/dt is given by Eqn (29), Eqn (33) becomes

$$\frac{dL}{dt} = \frac{-6gV\epsilon_b T_i^4}{DC_p T_o} \quad . \tag{34}$$

For the standard balloon, this corresponds to a loss of lift at 3 lbs/sec, the rate which we already calculated that mass is flowing into the balloon system, making it heavier. In particular, from Eqn (34) and (31), the mass flow rate is related to the rate of lift, L, by

$$\frac{dm}{dt} = -\frac{1}{g}\frac{dL}{dt} \quad . \tag{35}$$

Indeed, this relation can also be shown true for a general $\dot{Q}$ (see Eqn (23)) by combining Eqn (8), (25) and (27). Thus, as illustrated in Figure 8, the balloon mass within the envelope becomes heavier as mass is taken in from the external environment as a result of heat loss.

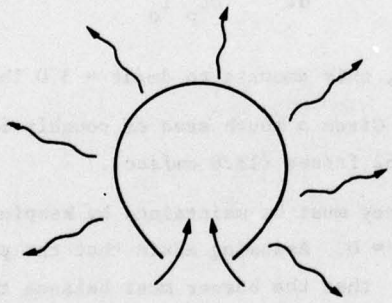

Figure 8. A Cooling Hot Air Balloon Takes in Air Containing Thermal Energy at a Lower Temperature and Greater Density to Compensate for the Energy Loss. As this Happens, the Balloon Becomes Heavier and Will Start to Move Downward.

IV. Aerodynamics of Hot Air Ballooning

A. Equation of Motion for a Hot Air Balloon

The aerodynamics of hot air ballooning is based on Newton's Law of Motion,

$$\bar{F} = m \frac{d\bar{V}}{dt} \quad . \tag{36}$$

The net external force, $\bar{F}$, a vector acting on the balloon consists of three terms, a vertical lift force, $\bar{L}$, a wind resistance force, $\bar{R}$, and a vertical weight force, $\bar{W}$, which includes the weight of the balloon envelope, gondola, etc. That is,

$$\bar{F} = \bar{L} + \bar{R} + \bar{W} \quad . \tag{37}$$

$\bar{L}$ can be expressed as

$$\bar{L} = L\bar{Z} \tag{38}$$

where $\bar{Z}$ is a unit vector pointing vertically upward and L is given by Eqn (8). $\bar{R}$ is given by

$$\bar{R} = -\frac{3}{2} C_D \rho_o \left(\frac{V}{D}\right) |\bar{V} - \bar{V}_w|(\bar{V} - \bar{V}_w) \tag{39}$$

where C_D is the drag coefficient (taken in this paper to be 1/2); ρ_o, the density of the external air; V, the velocity of the balloon; and V_w, the velocity of the wind acting on the balloon.

In Eqn (36), the mass of the balloon is expressed by the following relation:

$$m = \rho_1 V + M + \frac{1}{2} \rho_o V \quad . \tag{40}$$

The first term, $\rho_1 V$, is the mass of the enclosed air which, along with the rest of the balloon, is acted upon by $\bar{F}$. The second term, $M = |\bar{W}/g|$, is the mass of the balloon equipment such as the envelope, fuel, gondola, passengers, etc. The final term, $1/2\ \rho_o V$, is the mass of the external air dragged by the balloon. For a perfectly buoyant balloon, it is easy to show that

$$m = \frac{3}{2} \rho_o V \quad . \tag{41}$$

Another way to describe the terms which comprise $\bar{F}$ in Eqn (37) with the exception of $\bar{R}$, is to say that $\bar{F}$ is comprised of the weight of the various mass components,

described above. For example, the weight of the enclosed air is $\bar{L}$ (a sort of negative weight), the weight of the balloon equipment is $\bar{W}$, and the weight of the dragged external air is zero since this air is perfectly buoyant.

B. Buoyant Balloon in an External Air Flow

Consider a balloon acted upon by an external air flow as shown in Figure 9.

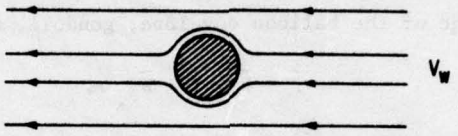

Figure 9. Balloon in External Air Flow

If the balloon is buoyant, $\bar{L} = -\bar{W}$ and

$$\bar{R} = m \frac{d\bar{V}}{dt} \quad . \tag{42}$$

Since the acceleration, dV/dt, takes place in the direction of the air flow, Eqn (42) becomes the scalar equation (using Eqns (39) and (41))

$$\frac{(C_D)}{D} (v - v_w)^2 = \frac{dv}{dt} \quad . \tag{43}$$

The solution of Eqn (43) is

$$v = v_w \left[1 - \frac{1}{(at + 1)} \right] \tag{44}$$

where $a = C_D v_w/D$. From this relation it can be seen that a balloon starting from rest at time $t = 0$, will acquire one half the velocity of the external air flow in a time $t = 1/a$. This time is then a measure of the dynamic response of a balloon to an impinging wind.

As an example, consider a standard balloon, traversing over the ground, which encounters a slowly rising or sinking air (a "thermal") which has a vertical speed of 5 cm/sec (.16 ft/sec). The dynamic response time is 568 sec. However, for a balloon encountering a wind shear of 15 mph (6.7 m/sec) the response time is 4.2 sec.

The distance traveled from time $t = 0$ to a time t is the integral of Eqn (44):

$$x(t) = v_w \left[t - \frac{1}{a} \ln (at+1) \right] \quad . \tag{45}$$

At the response time,

$$x\left(\frac{1}{a}\right) = \frac{D}{C_D} \left[1 - \ln (2) \right] \quad , \tag{46}$$

which is independent of v_w. Thus, a balloon will always traverse the same distance in the response time regardless of the speed of the external air flow. For the standard balloon, this distance is 28.6 ft (8.7 m), just over half its diameter. This means, in words, that a buoyant balloon will always respond to any wind over a distance of roughly half its diameter but in a time proportional to the speed of the air flow.

C. Response of a Balloon to Loss of Heat

As a balloon cools, air flows in the mouth to maintain pressure equilibrium as shown in Figure 10. The weight of the balloon thereby increases at the rate at which weight is added.

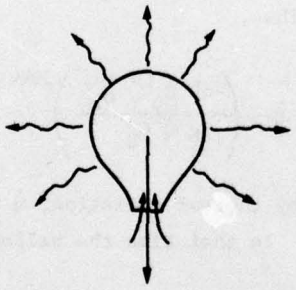

Figure 10. Air Flow in and out of Balloon Mouth as a Response to Heat Transfer

According to Eqns (25), (26) and (35)

$$\frac{dL}{dt} = \frac{\dot{Q}\, g}{C_p\, T_o} \tag{47}$$

where $\dot{Q}$, a negative rate, is the power loss from the balloon by all processes other than mass flow through the mouth. For $\dot{Q}$ constant and if at time t = 0, L = W, then

$$L = \frac{\dot{Q}\, g}{C_p\, T_o}\, t + W \quad . \tag{48}$$

If short times only are considered, such that the drag force can be neglected, then Eqn (36) becomes

$$\left(\frac{\dot{Q}\, g}{C_p\, T_o}\right) t = m\, \frac{dv}{dt} \tag{49}$$

where $m \simeq \frac{3}{2}\, \rho_o\, V$. The solutions for v(t) and x(t) are

$$v(t) = \left(\frac{\dot{Q}\, g}{3\, C_p T_o\, \rho_o V} \cdot t^2\right) \tag{50}$$

$$x(t) = \left(\frac{\dot{Q}\, g}{9\, C_p T_o\, \rho_o V} \cdot t^3\right) \quad . \tag{51}$$

The time $\bar{t}$ over which Eqns (50) and (51) are valid can be estimated by equating the drag force to the lift force, that is, when

$$\left(\frac{\dot{Q}\, g}{C_p T_o}\right)\bar{t} = -\frac{3}{2}\, C_D\, \rho_o \left(\frac{V}{D}\right) v^2 \tag{52}$$

where v is given by Eqn (50). Thus,

$$\bar{t} \simeq \left(\frac{-6D\, C_p T_o\, \rho_o V}{g\, \dot{Q}\, C_D}\right)^{1/3} \quad . \tag{53}$$

If most of the cooling is by thermal radiation, $\dot{Q}$ is given by Eqn (16) and for the standard balloon, $\bar{t} = 28.6$ sec. In that time the balloon falls 62.2 ft (18.97m) according to Eqn (50).

For times $t > \bar{t}$, the drag force is equal to the lift force, and in that case,

$$v = \left(\frac{-2\dot{Q} g\, D\, t}{3\, C_p T_o C_D\, \rho_o V}\right)^{1/2} \quad . \tag{54}$$

The relations in Eqns (50) and (54) indicate that a balloon, initially at a stationary altitude, will start to sink with a velocity proportional to the time squared until it reaches terminal velocity, but because of continued cooling, mass is constantly added to the balloon so that its terminal velocity increases slowly with the square root of time.

D. Response of Balloon to Loss of Ballast

If the balloon suddenly loses an amount of weight, $\bar{W}$, it will accelerate upwards until a limiting velocity, v_{max}, is reached. As in the previous section, this critical velocity can be calculated by equating the drag force to the net upward force which is equal to $\bar{W}$.

That is,

$$\frac{3}{2} C_D \rho_o \left(\frac{V}{D}\right) v_{max}^2 = \bar{W} \tag{55}$$

or

$$v_{max} = \sqrt{\frac{2 \bar{W} D}{3 C_D \rho_o V}} \quad . \tag{56}$$

As an example, assume a parachutist of weight 160 lbs (72.6 kg) jumps from the standard balloon. The balloon should acquire a maximum ascent rate, according to Eqn (56) of 534 ft/min (271 cm/sec).

E. Envelope Dimpling Limit (Ref. 3)

Consider a balloon under the influence of an external air flow shown in Figure 11. The question is, at what wind velocity, v_D, will the balloon no longer be able to withstand the aerodynamic pressure, R_s, and thereby cease to be rigid?

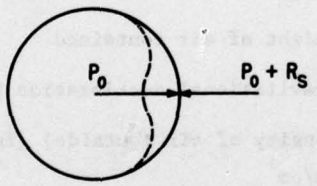

Figure 11. Pressure Conditions Effecting Dimpling

Such a problem is of importance in determining what wind speeds are possible for inflation. If the wall of the balloon could be displaced, the wall could be burnt by the burner during inflation. The condition for collapse to occur is

$$P_o + R_s = P_i \tag{57}$$

where R_s is the stagnation pressure which according to Reference 2 is $1/2\ \rho_o\ v_D^2$ at the center of the balloon. At the mouth of the balloon, P_o and P_i are equal and according to Eqn (2) the pressure difference $P_i - P_o$ at one half the height of the balloon must be

$$P_i - P_o = (\rho_o - \rho_i)\ g\ D/2 \quad . \tag{58}$$

Using Eqn (6), we can rewrite this relation as

$$P_i - P_o = \rho_o\ g\ D/2\ \frac{T_i - T_o}{T_i} \quad . \tag{59}$$

The critical wind speed, v_D, can be calculated from Eqns (39), (57) and (59) to give

$$v_D = \sqrt{gD\ (T_i - T_o)/T_i} \quad . \tag{60}$$

For the standard balloon, this speed is 10 mph (448 cm/sec). This means that for wind speeds greater than v_D, the upwind side of the balloon will begin to collapse because of the pressure loading by the air flow.

Symbols

In order of appearance in text

L	Lift
W_o	Weight if air displaced
W_i	Weight of air contained
g	Gravitational acceleration 980 cm/sec^2
$\rho_{(o)\ (i)}$	Density of air (outside) (inside) at sea level = 1.22×10^{-3} gm/cm^3
V	Volume of balloon
$T_{(o)\ (i)}$	Temperature (outside) (inside)
B	Constant of proportionality in gas equation of state = 2.87×10^6 cm^2/(sec^2 °K)
E	Thermal energy inside balloon
C_p	Specific heat at constant pressure (1.01×10^7 ergs/gm °K)
$\dot{Q}_{burner}$	Power output of burner
S	Solar flux 442 BTU/hr ft^2 (1.4×10^6 erg/cm^2 sec)
α_s	Solar absorptivity of envelope

e	Internal energy/volume inside envelope
γ	Ratio of specific heats = 1.667
$\dot{Q}_{solar}$	Solar power absorbed by balloon
$\dot{Q}_{reflected}$	Reflected solar power absorbed by balloon
r	Reflectivity of earth's surface $\sim$.06 for most of earth
T_g	Ground temperature
γ_{th}	Absorptivity of thermal radiation by balloon
ϵ_g	Emissivity of ground .9
σ	Stefan-Boltzmann Constant 5.673×10^{-5} ergs/cm^2 sec °K^4
ϵ_b	Emissivity of balloon
$\dot{Q}_{conv}$	Power loss by convection
H_o	Heat transfer coefficient
h	A constant of proportionality in heat transfer by free convection, .27 when T is in °F and D in feet.
λ	Thermal conductivity 2.69×10^3 erg/°K cm sec
Nu	Nusselt number
C	Dimensionless number = .4 in expression for Nusselt number
μ	Viscosity of air $2.0/x\ 10^{-4}$ gm/cm sec
Pr	Prandtl Number = .7 for air
$\dot{Q}_{air}$	Power gain or loss by air through mouth of balloon
m	Mass
A	$6\epsilon_b \sigma V/D$
U	$6\epsilon_b \sigma/(D\ C_p\ \rho_o\ T_o^2)$
R	Drag force
C_D	Drag coefficient, assumed to be .5
v	Velocity of balloon
v_w	Wind velocity
a	(Response time of balloon to wind)$^{-1}$
t	Time
$\bar{W}$	Weight of ballast lost
v_{max}	Terminal velocity
R_s	Stagnation pressure on balloon
v_D	Critical wind speed for envelope dimpling

References

1. Jackson, John P. and Rudolph J. Dichtl. The Science & Art of Hot Air Ballooning. Albuquerque, NM: Sun Publishing Co., 1977.

2. Prandtl, L. and O. G. Tietjens. Fundamentals of Hydro and Aeromechanics. New York: Dover Publications, Inc., 1934.

3. Stefan, Karl. "Technical Discussion." Ballooning, Vol. 7 (Winter 1973-1974), 14-17.

4. Meyers, Philip F. Tethered Balloon Handbook. Cambridge, MA: Goodyear Aerospace Corp., Project No. AF-6665, AD685183, 31 December 1968.

5. Warner, Edward P. Aerostatics. New York: Ronald Press Co., 1926.

6. Stefan, Karl. "Performance Theory for Hot Air Balloons." Unpublished paper, National Center for Atmospheric Research, Boulder, Colorado, April 1971.

7. Chapman, Alan J. Heat Transfer. New York: Macmillan, 1967.

8. Weast, R. C. Handbook of Chemistry and Physics. 53rd ed. Cleveland, OH: CRC Press, 1972.

9. Keenan, Joseph H. and Joseph Kaye. Gas Tables. New York: John Wiley and Sons, 1948.

10. Jumper, Eric. Private communication. Aeronautics Department, USAF Academy, Colorado 80840.

SECTION II

FLUID MECHANICS

STREAMLINE PLOTTING FOR AXISYMMETRIC CONE IN SUPERSONIC FLOW

Michael P. Baudhuin*

Abstract

This paper describes the development and application of a direct method of plotting streamlines around an axisymmetric cone in supersonic flow. The method first uses the Taylor-Maccoll theory to determine the flow properties along any ray. Once the flow properties are defined, the continuity equation is applied to determine the path of the streamlines. The combination of continuity and the Taylor-Maccoll theory thus results in a direct method to completely define the flow and plot the streamlines around the cone. It is a method which is easily programmed with the only required inputs being upstream Mach number and cone half-angle.

I. Introduction

Although a number of methods exist for describing two-dimensional supersonic flow past a wedge, no direct method is available to describe the flow past an axisymmetric cone. The absence of a direct method can be attributed to the non-uniform flow downstream of a conical shock wave (Ref. 1). Rather than a simple flow deflection at the shock followed by a uniform flow field, as in the two-dimensional case, only a part of the turning takes place at the conical shock with the remainder taking place through continuous isentropic compression; the flow field downstream of the conical shock then, though isentropic, is not uniform (Ref. 2). The solution for this flow, first given by Busemann and in a different form by Taylor and Maccoll, consists of fitting an isentropic conical flow field to the conical shock. Taylor and Maccoll showed that conditions were constant on each ray from the vertex of the cone, which allowed them to write the three-dimensional equations for the isentropic flow in terms of the single conical variable theta (Ref. 1). This resulted in an ordinary, non-linear differential equation which had to be solved numerically.

Once the flow field was defined through numerical techniques the streamlines could be plotted through a method called isoclines. This method involves laying off straight line segments from point to point in the direction specified by the flow properties along rays of uniform properties. Although relatively accurate, this method requires interpolation and cross-referencing between tables and graphs, a method not well suited to computer techniques. Further, it is not possible to enter a table or figure with only upstream Mach number and cone half-angle, the usual parameters known by investigators.

Because of the indirect approach to solving the flow equations, and the inapplicability of previous methods to computer techniques, the purpose of this paper is to

---

*Cadet, USAFA, presently 2nd Lt, USAF, Williams AFB, AZ

describe the development and application of a new, direct method for plotting these streamlines. The method herein described uses a variation of the Taylor-Maccoll theory to define the flow properties at every point from the shock to the cone surface. The mass continuity equation is then employed to derive an expression for the position of a streamline as a function only of upstream Mach number and cone half-angle. This method does lend itself to computer controlled plot routines, and various computer generated plots are included to demonstrate its applicability.

II. Theory

As mentioned above, the method requires that the flow be defined at every point from the cone surface to the shock wave. One of the results of the Taylor-Maccoll solution is the needed description of the flow field in this region, but, little of this information has been previously published. We will start by examining the Taylor-Maccoll solution, and how it may be applied to completely define the flow.

Taylor and Maccoll started with the non-linear differential equation for flow around a cone. This equation can be written as,

$$\left[\frac{d^2\left(\frac{u}{c}\right)}{d\theta^2} \frac{\gamma+1}{2} \left(\frac{d\frac{u}{c}}{d\theta}\right)^2 - \frac{\gamma-1}{2}\left(1-\frac{u^2}{c^2}\right)\right] =$$

$$(\gamma-1)\left(1-\frac{u^2}{c^2}\right)\frac{u}{c} + \frac{\gamma-1}{2}\left(1-\frac{u^2}{c^2}\right)\cot\theta\,\frac{d\frac{u}{c}}{d\theta} - \gamma\frac{u}{c}\left(\frac{\frac{u}{c}}{d\theta}\right)^2 - \frac{\gamma-1}{2}\cot\theta\left(\frac{d\frac{u}{c}}{d\theta}\right)^3 \quad , \quad (1)$$

where u is the flow velocity along a ray, θ is the angle measured from the cone centerline to the ray, and c is a constant equal to the velocity the flow would achieve if allowed to expand adiabatically into a vacuum (Ref. 3).

This equation relies on the assumption that the flow is isentropic ahead of the shock as well as behind it. At the shock itself there is a discontinuity which remains constant along the ray. This condition that properties are constant along each ray was first presented by Busemann and is suggested by the fact that the shock wave is straight with constant pressure behind it and that the cone surface pressure is constant (Ref. 4).

With these assumptions Taylor and Maccoll proceeded to arrive at a solution of Equation (1) by selecting a value for the cone half-angle, δ, and assuming a value for u/c at the cone's surface. They then integrated the equation stepwise for small steps in θ by replacing the differential equation by a finite-difference equation where the first value of θ was the cone half-angle and the value for u/c was the assumed value on the surface. The final step was to determine the appropriate value of θ which corresponded to the actual shock. This was done by trial and error. For each value

of θ during the integration there was a corresponding flow angle, ϕ, and Mach number, M. The values for ϕ and M were compared to the values found by two-dimensional flow analysis. When the Mach number and turning angle for both two-dimensional and three-dimensional cases agreed, the limit of integration had been reached and the correct shock strength found. They then found the value of upstream Mach number from the two-dimensional shock relationships. Thus Taylor and Maccoll defined the shock angle, the upstream Mach number, and the flow properties at the shock. Another of the results of their solution which Taylor and Maccoll did not, however, address is the possibility of describing the flow on every cone-vertex-eminating ray from behind the shock to the cone surface itself (Ref. 4). Other authors, however, have used the results produced by the Taylor-Maccoll solution to describe the flow field in this region.

The Department of Electrical Engineering Center of Analysis at the Massachusetts Institute of Technology has published a book containing over 500 pages of tabulated results prepared under the direction of Zdenek Kopal (Ref. 3). Although these results define the flow very accurately everywhere from the cone surface to the shock, they are of limited application here since Mach numbers are not the values commonly used in these calculations. The upstream values of Mach number found in Kopal's calculations correspond to a given value of cone half-angle and cone surface velocity. The free stream values are therefore Mach numbers such as 3.2383 or 2.7349 and of little direct use in most cases. As Kopal describes in his book (Ref. 3):

> We begin with a known semi-apex angle ϑ_s of solid cone and an assumed value of u_s/c; but the corresponding Mach number cannot be determined until after we have crossed the shock wave... It does not seem possible to carry out a solution numerically or otherwise with preassigned values of θ_s and u/a.

So Kopal, using the Taylor-Maccoll method, gives the flow properties on every ray from the cone surface to the shock with five-digit accuracy. This provides more information than Taylor and Maccoll, but again, lists the flow properties at values of upstream Mach number that are not always the values desired. Since Kopal's calculations could not provide the data for an arbitrary value of Mach number, we found it necessary to create a numerical program which could.

The program we developed follows much along the line of the Taylor-Maccoll method in that it integrates the non-linear second order differential equation that describes the flow. It differs from Kopal's method, however, in that an upstream Mach number is chosen, and the flow turning angle and downstream Mach number are computed at each ray as a function of this Mach number. Our program starts by assuming a value for u/c on the surface and integrates the equation stepwise for small steps in θ. It then compares the values against the turn angle and Mach number that would be obtained if the chosen upstream Mach number were to pass through a two-dimensional shock at the given angle θ. If there is not a ray where the two values match, then the program

changes u/c at the surface and proceeds in an iterative fashion until the two-dimensional and three-dimensional cases agree. These values are then stored, and the result is a complete description of the flow from cone surface to shock wave for any value of upstream Mach number and cone half-angle.

Once we defined the flow (velocity, pressure, and temperature) at every ray from the cone surface to the shock wave, we devised a method to accurately determine the streamline positions as a function of those properties. As mentioned earlier, we did this through the application of the mass continuity equation. To successfully apply the equation, we found it necessary to describe all its terms as functions of the properties defined by our solution of the Taylor-Maccoll equation. The following section describes how this was accomplished.

We first considered a cone in supersonic flow with a control volume defined along two arbitrary rays extending from the vertex of the cone to some, also arbitrary, streamline as is shown in Figure 1.

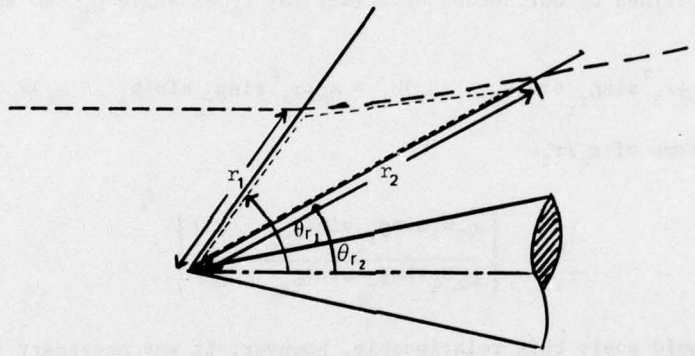

Figure 1. Axisymmetrical Cone

Since mass cannot be transported across a streamline, it became apparent that the mass transported across the conical surface area defined by r_1 and θ_{r_1} must exactly equal the mass transported across the conical surface area defined by r_2 and θ_{r_2}, the downstream closure of our control volume. For this reason the reference area A_1 was chosen as the conical surface area described by r_1 and θ_{r_1} so that,

$$A_1 = \pi r_1^2 \sin \theta_{r_1} \cdot \qquad (2)$$

Since flow properties are constant along any ray the mass flow across area A_1 could be written as

$$\dot{m}_1 = \rho_1 \pi r_1^2 \sin\theta_{r_1} V_{n_1} , \tag{3}$$

where V_{n_1} is the component of velocity normal to the ray. This velocity, V_{n_1}, could then be written in terms of the variables given in our Taylor-Maccoll solution by the observation that

$$V_{n_1} = W_1 \sin(\theta_{r_1} - \phi_1) , \tag{4}$$

where W_1 is the total velocity at ray θ_{r_1} and ϕ_1 is the flow turning angle, or streamline angle at ray θ_{r_1}. The mass flow equation now became

$$\dot{m}_1 = \rho_1 \pi r_1^2 \sin\theta_{r_1} \sin(\theta_{r_1} - \phi_1) W_1 . \tag{5}$$

As was mentioned earlier, however, this mass flow must exactly equal the mass flow across the area defined by our second arbitrary ray r_2 at angle θ_{r_2} so that

$$\rho_1 \pi r_1^2 \sin\theta_{r_1} \sin(\theta_{r_1} - \phi_1) W_1 = \rho_2 \pi r_2^2 \sin\theta_{r_2} \sin(\theta_{r_2} - \phi_2) W_2 \tag{6}$$

or, written in terms of r_2/r_1,

$$\frac{r_2}{r_1} = \left\{ \frac{\rho_1 W_1 \sin\theta_{r_1} \sin(\theta_{r_1} - \phi_1)}{\rho_2 W_2 \sin\theta_{r_2} \sin(\theta_{r_2} - \phi_2)} \right\}^{\frac{1}{2}} . \tag{7}$$

Before we could apply this relationship, however, it was necessary to obtain an expression for ρ_1 and ρ_2 in terms of those properties already known from our Taylor-Maccoll solution. To express the density in terms of these properties we used the energy equation for a perfect gas which we wrote as

$$\tfrac{1}{2}W^2 + C_p T = C_p T_o = \tfrac{1}{2}c^2 , \tag{8}$$

where W and c remain as defined earlier, C_p is the specific heat at constant pressure, T is the local temperature, and T_o is the temperature which would be obtained by isentropic flow to a stagnation point. Dividing equation (8) by $C_p T_o$, or its equivalent $\tfrac{1}{2}c^2$ gives

$$\frac{T}{T_o} = 1 - \frac{W^2}{c^2} \tag{9}$$

and, by applying the isentropic relationship, we obtained

$$\frac{\rho}{\rho_o} = \left(1 - \frac{W^2}{c^2}\right)^{\frac{1}{\gamma-1}} \quad . \tag{10}$$

But, since ρ_o is a constant regardless of which ray is being considered, our final relationship became

$$\frac{\rho_1}{\rho_2} = \left\{ \frac{1 - \left(\frac{W}{c}\right)_1^2}{1 - \left(\frac{W}{c}\right)_2^2} \right\}^{\frac{1}{\gamma-1}} \quad . \tag{11}$$

With this relationship for density we could rewrite equation (7) as

$$\frac{r_2}{r_1} = \left\{ \left(\frac{1 - \left(\frac{W}{c}\right)_1^2}{1 - \left(\frac{W}{c}\right)_2^2} \right)^{\frac{1}{\gamma-1}} \frac{\left(\frac{W}{c}\right)_1 \sin\theta_{r_1} \sin(\theta_{r_1} - \phi_1)}{\left(\frac{W}{c}\right)_2 \sin\theta_{r_2} \sin(\theta_{r_2} - \phi_2)} \right\}^{\frac{1}{2}} \quad , \tag{12}$$

where, as you recall, θ_{r_1} and θ_{r_2} can be any arbitrary rays. To make the relationship useful, however, we set θ_{r_1} as the shock wave angle and varied θ_{r_2} from the shock to the cone surface. By programming this equation and finding r_2 for each ray we were able to follow a streamline from the time it contacted the shock, to any desired distance downstream. Also, since the ratio r_2/r_1 does not depend upon the value of r_1, the same equation could be used to find any number of streamlines simply by varying the value of r_1. Thus, a streamline, or any number of streamlines, could be plotted as a function only of upstream Mach number and cone half-angle.

III. Results

In order to demonstrate the applicability of the above method we wrote a program which would plot streamlines directly. As mentioned, the only required inputs were upstream Mach number, cone half-angle, and the accuracy desired. The program as it presently exists computes the flow properties to within a separate degree of accuracy in either Mach number or turning angle. The plots which follow are based upon a difference in two-dimensional to three-dimensional Mach number of 0.005 and a difference in two-dimensional to three-dimensional turning angle of 0.003 radians, or 0.15 degree. The results obtained exceed the accuracy available from Dailey (Ref. 4), but are not

as accurate as the results found by Kopal's (Ref. 3) calculations. It should be noted, however, that the capability exists to obtain results more accurate even than those given by Kopal.

Our program was run for a varied range of Mach numbers and cone half-angles to assure its accuracy and applicability for the entire range of cone-Mach number combinations. A representative sample of the results follows with the first plot drawn for a Mach number of 1.8 and cone half-angle of 10.0 degrees. Our program calculated the shock wave to be at 34.8 degrees and drew the plot shown in Figure 2.

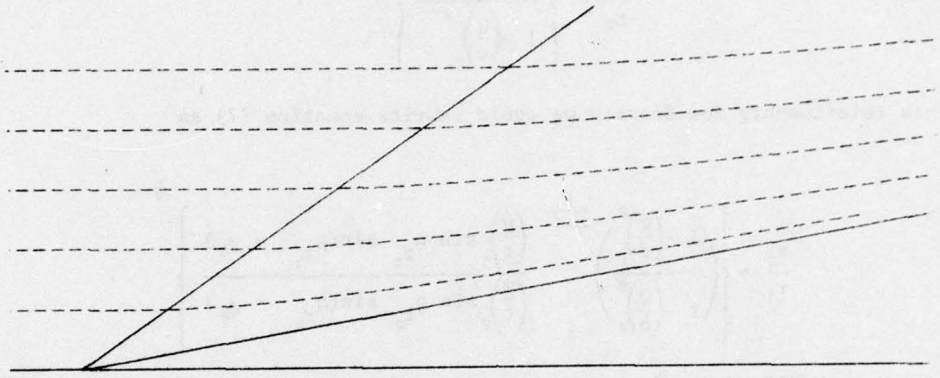

Figure 2. Cone of 10 Degree Half-Angle, M = 1.8

Figure 3 presents a cone of 36° half-angle in an upstream flow of Mach 4.0. The program computed the shock wave angle at 43.8 degrees and plotted the flow as is shown in Figure 3.

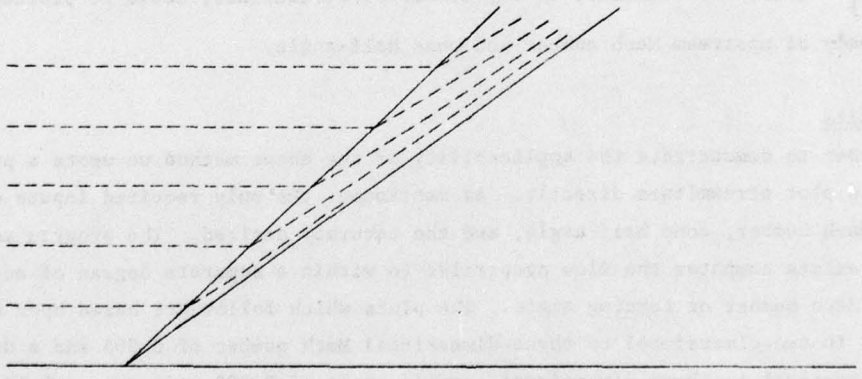

Figure 3. Cone of 36 Degree Half-Angle, M = 4.0

The final example, Figure 4, shows a cone of 8° half-angle and an upstream Mach number of 2.6. The program computed the wave angle at 23.6 degrees and plotted the flow as is shown in Figure 4.

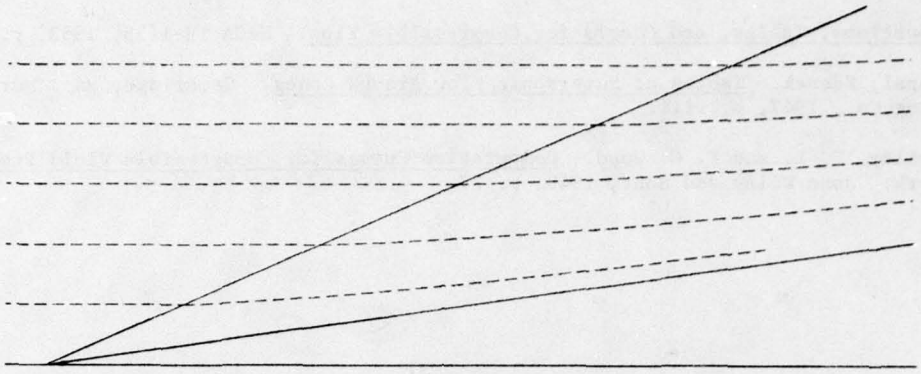

Figure 4. Cone of 8 Degree Half-Angle, M = 2.6

These plots are representative examples of what can be done with our method of defining streamlines. The plots are accurate to within .025% which is considerably better than what can be accomplished using the method of isoclines.

IV. Conclusion

We have presented the development and application of a direct method for plotting streamlines around an axisymmetric cone in supersonic flow. The method uses a variation of the Taylor-Maccoll solution and the mass continuity equation to generate a ratio r_2/r_1 which can be applied to a plotting routine. The plots produced are more accurate than previous methods and require only upstream Mach number and cone half-angle as inputs. The computer generated results eliminate the need for cross-referencing, and use as inputs the variables commonly known by investigators. Thus, we believe, we have presented a new method to plot streamlines which has many significant advantages over the method of isoclines.

Acknowledgement

I wish to express appreciation to Lt Col William A. Edgington for his guidance and support throughout this project.

References

1. Liepmann, H. W. and A. Roshko. Elements of Gas Dynamics. New York: John Wiley and Sons, 1957, p. 120.

2. Equations, Tables, and Charts for Compressible Flow. NACA TR-1135, 1953, p. 20.

3. Kopal, Zdenek. Tables of Supersonic Flow Around Cones. Cambridge, MA: Murray Printing Co., 1947, p. viii.

4. Dailey, C. L. and F. C. Wood. Computation Curves for Compressible Fluid Problems. New York: John Wiley and Sons, 1949, p. 27.

SECTION III

THERMODYNAMICS AND HEAT TRANSFER

OPTIMIZATION OF LOW QUALITY ENERGY CONVERSION

Robert C. Winn*

Abstract

This paper analyzes the use of low quality energy resources as the input to drive a heat engine. The relationship between the energy conversion efficiency of the engine and the amount of energy removed from the source is discussed. This relationship is used to develop an expression for the engine temperature which will result in the maximum power output. Results of the analysis as applied to two Colorado geothermal resources are shown.

I. Introduction

As fossil fuels become increasingly more expensive and hard to find, low quality (i.e., low temperature) energy sources are being considered as the supply for heat engines. These sources include hot water from geothermal activity, waste heat from an industrial application, the output of solar collectors, etc. Typical characteristics of many of these energy sources are a relatively low temperature and a fixed mass flow rate. The low temperature dictates a low energy conversion efficiency; the fixed mass flow rate limits the amount of energy available to the heat engine.

There is a relationship between the energy conversion efficiency of the engine and the amount of energy removed from the source. The fluid from the energy source enters a heat exchanger and is cooled by the heat engine. Because the mass flow rate is constant, the amount of energy removed is directly related to the decrease in the temperature of the source fluid. The temperature in the hot portion of the heat engine can be no greater than the lowest temperature of the source fluid because the heat transfer is from the source fluid to the engine. The temperature in the hot portion of the heat engine, along with the temperature in the cold portion, determines the energy conversion efficiency of the engine. If a small amount of energy is taken from the source fluid, a relatively high efficiency results, but the engine power output is low because not much energy is available to the engine. Conversely, if a large amount of energy is made available to the engine, the engine efficiency will be low, resulting in low power output. There is one combination of energy extracted and engine efficiency which will result in the maximum power output of the engine.

II. Theoretical Analysis

Any heat engine which can be driven by a low quality energy source can be analyzed in terms of a Carnot engine. The real engine can be expected to perform at an energy conversion efficiency which is some fraction, η_2, of the Carnot efficiency. η_2 is

*Captain, USAF, Assistant Professor of Aeronautics, DFAN

often referred to as the second law efficiency. The Carnot efficiency is calculated using the maximum and minimum temperatures of the working fluid in the engine. The minimum engine temperature is some temperature difference, β, above the temperature of the environment, T_e, assuming unlimited access to the environment. The maximum temperature, however, would be dependent on how much energy is removed from the source, $\dot{Q}_{in}$.

Because the energy is available from the source at a fixed mass flow rate, $\dot{m}$, and a fixed temperature, T_a, increasing $\dot{Q}_{in}$ decreases T, the temperature of the source fluid leaving the engine's heat exchanger. The engine's working fluid typically experiences what may be treated as a constant temperature process, such as the constant pressure boiling in a Rankine cycle. The working fluid in a Rankine cycle used for low quality energy conversion usually enters the boiler as a slightly sub-cooled liquid, is heated to the boiling temperature, boils, and perhaps, is slightly superheated. The vast majority of the heat transfer occurs with the fluid at its boiling temperature. Therefore, for the purpose of determining the engine's efficiency, the engine's maximum temperature may be treated as the boiling temperature, which is a constant throughout the heat exchanger. By the second law of thermodynamics, the temperature of the engine's working fluid must be less than T because the heat interaction is from the source fluid to the engine's working fluid. The difference between the temperature of the source fluid leaving the heat exchanger and the temperature of the hot portion of the engine is α as shown in Figure 1. Therefore, if α is constant, as more energy is made available to the heat engine, the maximum engine temperature decreases. This decreases energy conversion efficiency.

The functional relationship of engine power output, $\dot{W}$, to the temperature of the source fluid leaving the engine's heat exchanger is shown using Figure 2. The efficiency of a Carnot engine is

$$\eta_{Carnot} = 1 - \frac{T_e + \beta}{T - \alpha} . \tag{1}$$

The efficiency of the real engine is

$$\eta = \eta_2 \, \eta_{Carnot} = \frac{\dot{W}}{\dot{Q}_{in}} , \tag{2}$$

where

$$\dot{Q}_{in} = \dot{m} \, c_p \, (T_a - T) , \tag{3}$$

and c_p is the specific heat at constant pressure of the source fluid. Solving for the power output,

$$\dot{W} = \eta_2 \, \dot{m} \, c_p \, (T_a - T) \left(1 - \frac{T_e + \beta}{T - \alpha}\right) . \tag{4}$$

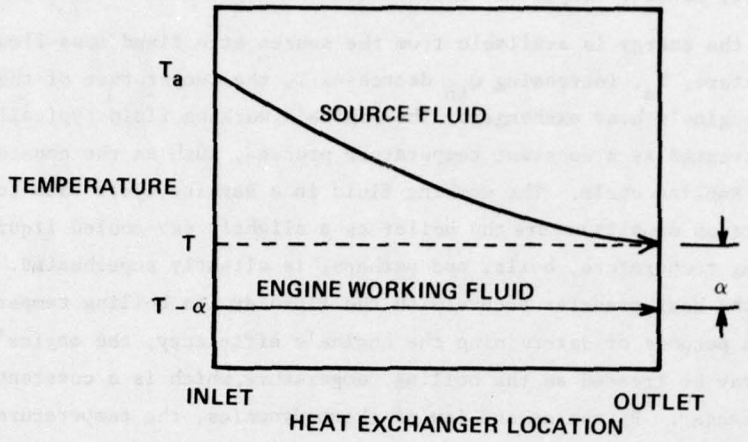

Figure 1. Temperature Variation in the Engine's Heat Exchanger

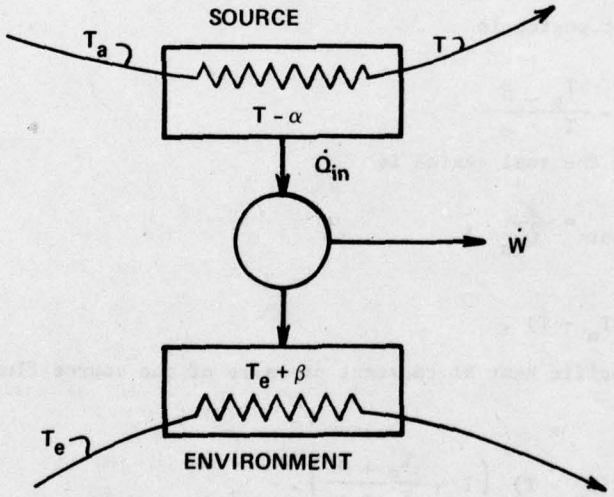

Figure 2. System Sketch

All of the variables in this power equation except T are fixed by the energy source, the environment, or the heat engine itself. T is a design choice. The one value of T which results in the maximum power output is found by setting

$$\frac{d\dot{W}}{dT} = 0. \tag{5}$$

This optimum temperature is

$$T_{opt} = \alpha + \sqrt{T_a T_e - \alpha T_e + \beta T_a - \alpha\beta} \quad . \tag{6}$$

III. Results

To demonstrate this analysis, consider the geothermal activity at Glenwood Springs, Colorado, and Hortense Hot Spring, Colorado, as energy sources for a heat engine. Glenwood Springs is an example of a source of large amounts of low quality energy, 9500 liters per minute at 321 K. Hortense Hot Spring, on the other hand, provides only 68 liters per minute of water at 355 K (Ref. 1). Assume that for both cases α is 5 K, β is 10 K, T_e is 280 K, and η_2 is 0.7. Under these conditions, T_{opt} is 307.7 K for Glenwood Springs and 323.6 K for Hortense Hot Spring. The power supplied and the engine efficiency are shown in Figure 3.

The engine for Glenwood Springs has a maximum power output of 259 kW with an engine efficiency of 2.9% while the engine for Hortense Hot Spring has a maximum power output of 9.3 kW with an engine efficiency of 6.3%. The low power output of the Hortense Hot Spring machine is a result of the very low mass flow rate out of the source. The power output is zero when the value of T is $T_e + \alpha + \beta$, which makes the engine efficiency zero, and when the value of T is T_a, which results in no energy being delivered to the engine. The maximum power output occurs when T is equal to T_{opt}.

The most important thing to notice in these results is the reduction in output if T is not adjusted to equal T_{opt}. If T is set so that it is 5 K greater than T_{opt}, the Glenwood Springs engine has an 11.3% reduction in power output, but the Hortense Hot Spring engine shows a decrease of only 2.8%. Because the Glenwood Springs geothermal energy source is such low quality energy, a severe penalty is paid for non-optimal performance.

The results indicate that an energy conversion device installed at Glenwood Springs could supply electricity to about 100 homes. If one were installed at Hortense Hot Spring, it could supply only about four homes. This does not suggest that one should be used and another not used. What the results do suggest, however, is that optimal control of the temperatures in both devices is essential, especially for the Glenwood Springs engine. As lower quality energy resources are used, the control of the engine temperatures becomes increasingly more critical.

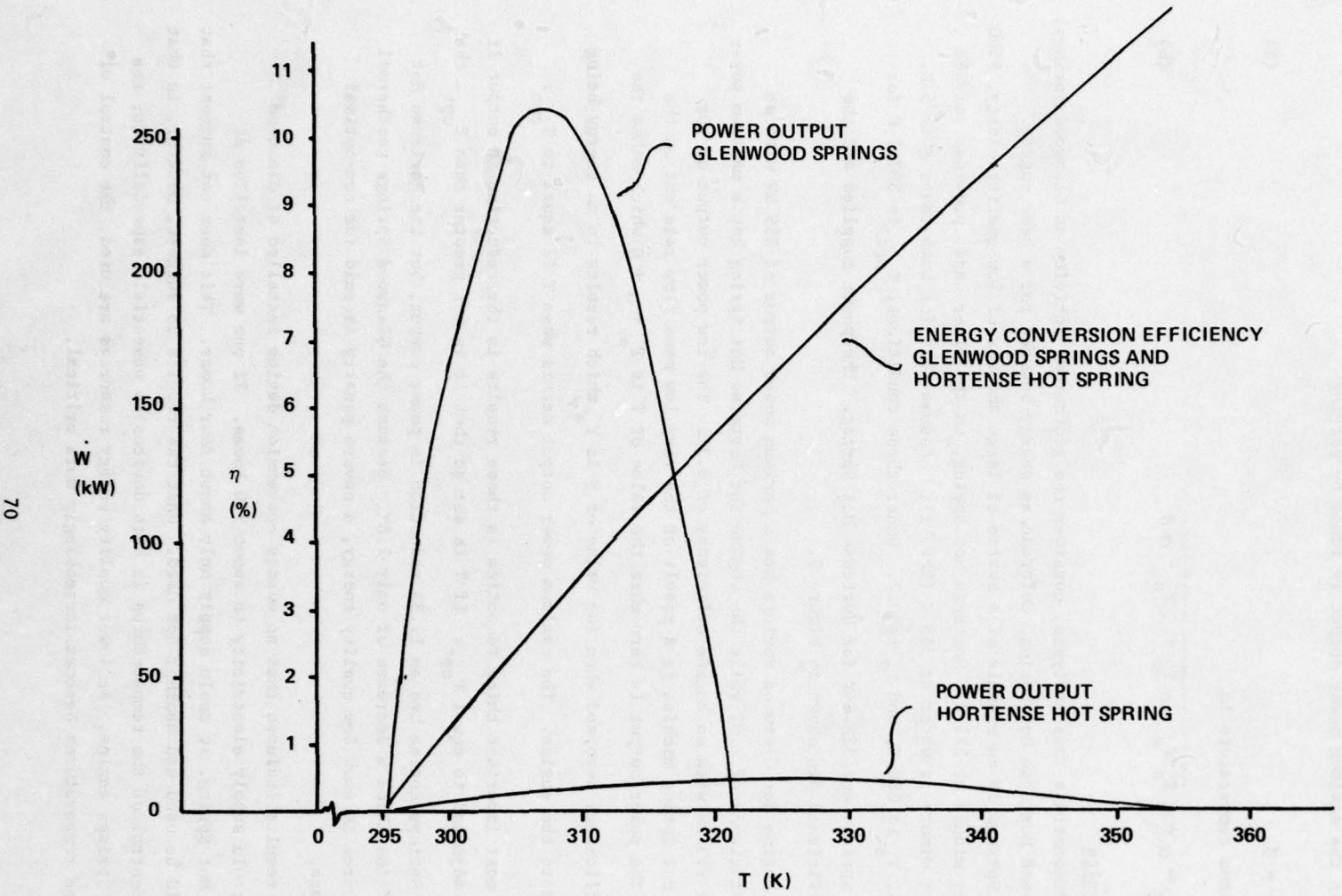

Figure 3. Power Supplied and Engine Efficiency

IV. Conclusions

In the past, heat engines were almost exclusively driven by high quality energy sources, such as a coal fire. Because of the large difference between the temperature of the source and that of the environment, a very small penalty was paid for non-optimal performance. When using low quality energy resources, however, one finds that large reductions in output result from small deviations from the optimum engine temperature. This trend was shown to become more significant when a lower quality energy resource was used. Thus, when using a low quality energy resource to drive a heat engine, one finds that optimal control is essential.

Reference

1. Department of the Interior. Energy Resources Map of Colorado. Miscellaneous Investigations Series I-1039. Arlington, VA: U.S. Geological Survey, 1977.

PERFORMANCE OF GROOVED HEAT PIPE EVAPORATORS WITH VAPOR RELEASE SLOTS

R. C. Oliver*

Abstract

The results of a theoretical analysis and an experimental investigation of the performance of a class of heat pipe evaporators are reported. The evaporators studied had grooved evaporator surfaces and employed transport wicks incorporating vapor release slots. Performance was characterized as a function of slot characteristics as well as conventional heat pipe parameters. Although a capillary limit fixes the critical heat rate (similar to non-slotted evaporators), considerable enhancement is noted for certain cases and the existence of an inverted meniscus (between the groove tips and the transport wick rather than at the base of the grooves as normally observed) is supported by the results and observations.

I. Introduction

Heat pipes with internal circumferential or axial grooves have recently become attractive as they provide high thermal conductance and high reliability at moderate costs (Ref. 1). The grooves may be constant size or may vary and even have covered sections to minimize liquid-vapor interface problems (Ref. 2). The internal evaporator grooves control intra-evaporator fluid distribution; however, they often lack the necessary permeability requirements for the high fluid transport rates required from the condenser. For this reason the design considered in this study employed a separate transport wick for fluid delivery from the condenser to the evaporator.

Initial analytical and experimental results have indicated a performance advantage for this design when compared to conventionally designed evaporators. The addition of slots in the transport wick permits the vapor generated in the evaporator to exit freely. Without slots a vapor barrier may impede fluid flow in the transport wick and lead to a premature performance limit. In addition to removing vapor barrier problems the use of slots is postulated to result in an inverted meniscus configuration as suggested by Saaski (Ref. 3). This concept leads to a thin liquid layer for a heat transfer path and a subsequently lower temperature drop, resulting in a higher heat transfer coefficient.

II. Background

Although there is a large amount of published data on heat pipes, evaporation from wicked surfaces and related phenomena, little attention has been given to configurations in which vapor is permitted to exit freely from the porous wick covered evaporator. Many past results have been configuration dependent, and perhaps for this

*Major, USAF, Assistant Professor of Aeronautics, DFAN

reason evaporator vapor blockage problems have not been widely identified. Performance below that predicted has been attributed to poor wick bonding and other evaporator characteristics even when phenomena characterizing vapor blockage (such as fluid ejection)were noted. Only recently have designers realized and actively attempted to avoid these phenomena, thereby increasing the evaporator capacity.

The heat pipe design discussed and considered in this study is illustrated in Figure 1. The object of this study was to predict the performance limits, particularly as related to the evaporator groove density (spacing), slot size and the total number of slots used. These characteristics, along with conventional heat pipe parameters including the transport wick thickness, permeability and effective pore radius, and the heat pipe effective length, were combined in a theoretical model.

III. Model Development

Heat pipe performance is governed and limited by the principles of thermal-fluid mechanics. Both hydrodynamic and heat transfer effects must be considered and evaluated. Although start up transients may be of interest in special cases, only steady-state operation is considered in this analysis. Except in unusual cases, start-up occurs naturally and its omission does not constitute a limitation to this study.

The description and results of the general approach used by most investigators are presented without development from basic principles. Emphasis is on the modifications to standard models as a consequence of the geometry and configuration of the evaporator modeled. Either the reference by Feldman (Ref. 4) or Winters and Barsch (Ref. 5) is suggested for a development of the standard heat pipe performance equations. Specifically addressed by this study are the critical heat rate and the heat transfer coefficient.

The limiting mechanism proposed for the critical heat rate is the wicking limit. This occurs when the capillary forces are insufficient to keep the evaporator surface supplied with fluid and the wick dries out. The heat pipe operates as long as the capillary surface tension pumping exceeds the sum of all pressure losses in the pipe. The condition for operation can be written as

$$\Delta P_s \geq \Delta P_\ell + \Delta P_b + \Delta P_{vv} + \Delta P_{vs} + \Delta P_{vg} \qquad (1)$$

where ΔP_s is the capillary surface tension pumping rise; the maximum rise is

$$\Delta P_{s_{max}} = \frac{2T}{r_e} \cdot \qquad (2)$$

Maximum pumping occurs with perfect wetting in the evaporator and a flooded condenser. The surface tension, T, and the effective pore radius, r_e, are characteristics of the transport wick.

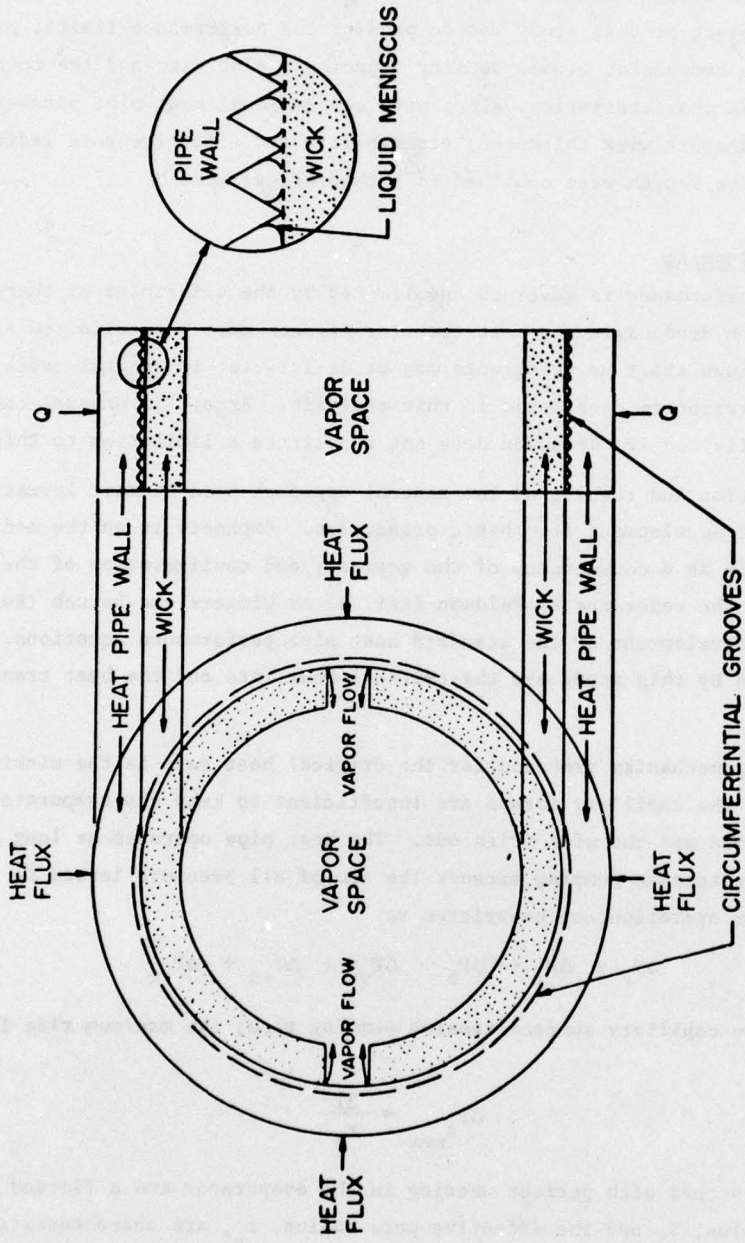

Figure 1. Cross Section of Heat Pipe Evaporator with Vapor Release Slots

The liquid pressure loss, ΔP_ℓ, for mesh, sintered power or sintered fiber wicks is given by Reference 4 as

$$\Delta P_\ell = \frac{\mu_e \dot{m}\, LP}{\rho_e k_e A_e} \quad , \tag{3}$$

where μ_e, ρ_e, and $\dot{m}$ are the liquid viscosity, density, and mass flow rate through the wick respectively. LP is the effective length of liquid travel, k_e and A_e are the wick permeability and cross section respectively.

The body force effect, ΔP_b, encompasses the effects of acceleration and gravitational field as well as electric and magnetic fields when applicable.

$$\vec{\nabla} P_b = \vec{\rho} \cdot \vec{g} \tag{4}$$

For horizontal heat pipe using a low surface tension fluid considering only gravity, Equation 3 reduces to (Ref. 6)

$$\Delta P_b = \rho_e g\, d_i \quad , \tag{5}$$

where ρ_e is the liquid density, g the gravity force, and d_i the diameter of evaporator through which fluid must be pumped.

The pressure loss for vapor space flow is

$$\Delta P_{vi} = \frac{8\, \mu_v \dot{m}\, LP_\pi}{\rho_v A_i^2} (\delta_i) \quad , \tag{6}$$

where the subscript i indicates that the formulation is valid in the vapor space (i = v), in the grooves (i = g), and in the slots (i = s). A correction factor (δ_i) is included in each regime to account for turbulent flow. The remaining terms relate to the vapor quantities of the variables described above.

Using the equality form of Equation 1 and substituting Equations 2, 4, 5, and 6, we can solve for the limiting flux as

$$\dot{Q}_{max} = \frac{(\Delta P_s - \Delta P_b)\, h_{fg}}{\frac{1}{\dot{m}} \Delta \rho_\ell + \frac{3}{2} \frac{1}{\dot{m}} \Delta \rho_{vi}} \quad , \tag{7}$$

where the fact that $\dot{Q} = h_{fg} \dot{m}$ was employed. Of course, h_{fg} is the enthalpy of phase change and $\dot{m}$ the flow rate.

Equation 7, whose development has been outlined, represents the limiting critical heat rate. Assumptions required for the developments from basic principles are enumerated and addressed in Reference 6 and pose no problem to our use of the developed equation.

In addition to the determination of the critical heat rate, the heat transfer coefficient should also be specified. Analytical predictions of the heat transfer coefficient for heat pipes have been notably unsuccessful. In fact, in a recent investigation including an extensive literature search, Barthelemy noted that "it must be concluded that the analytical prediction of the heat transfer coefficient, even in the purely grooved heat pipe, is a complex task" (Ref. 7). Notwithstanding, the coefficient and the corresponding temperature difference were deemed sufficiently important to justify an attempt at its prediction.

The heat transfer coefficient, h_e, is defined as

$$h_e = \frac{\text{flux}}{\Delta T} = \frac{\dot{Q}}{A\,(T_e - T_v)} \quad , \tag{8}$$

where $\dot{Q}$ is the applied heat rate, T_e is the evaporator temperature, T_v is the vapor temperature, and A is the heat transfer area. For this study, A is the surface area of a cylinder with a radius equal to the tip of the threads. This projected area is used regardless of the groove geometry or the wetted areas. Although the heat transfer coefficients predicted are much lower than if the wetted area were used, the results are a more useful indication of the capacity of a given surface.

The method used in this study employed the previously calculated value of the heat rate as $\dot{Q}$, leaving then the area (known) and the temperature difference to complete the specification of h_e. From heat transfer arguments the thermal fluid resistance term is

$$R_{th_f} = \frac{\Delta X}{A_w K_f} \quad , \tag{9}$$

where ΔX is the average liquid thickness over the wetted area (A_w) and K_f is the fluid thermal conductivity. Figure 2 illustrates the actual and idealized meniscus shape. The groove density and applied heat rate affect the vapor pressure and velocity in the groove affecting the meniscus shape. This variation was not estimated and an empirical ($\Delta X/A_w$) was established from initial experimental liquid thickness/wetted area ratio results. Although this is certainly not a theoretical approach no theoretical approach is known and it was felt that this method could be useful in predicting results.

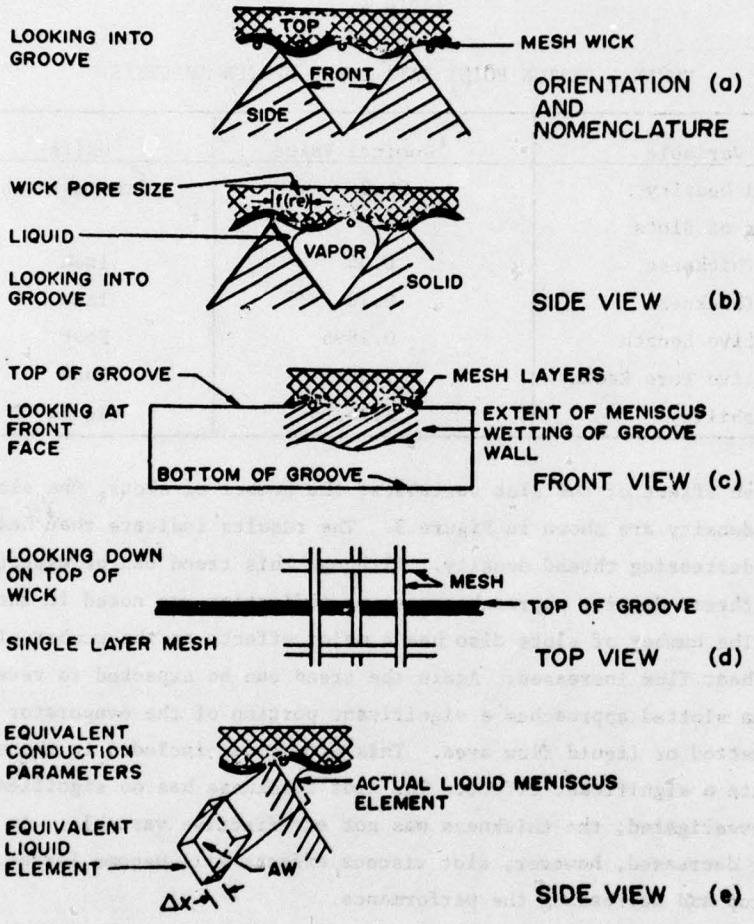

Figure 2. Meniscus Shape as a Function of Groove Density and Screen Mesh

IV. Model Predictions

The results of the described model are best presented for an arbitrary design, showing the variation in performance as a result of the selected parameters. A nominal design point was selected and is indicated in Table 1. Each of the investigated parameters was then varied analytically from 20 to 200% of the design value (Table 1) and the results calculated. Results are based on measured, not theoretical, groove areas as a considerable difference between ideal triangular teeth and threaded pipe samples was observed.

Table 1

NOMINAL DESIGN POINT DATA FOR COMPUTER ANALYSIS

Variable	Nominal Value	Units
Thread Density	96.0	Grooves/Inch
Number of Slots	2.0	
Slot Thickness	0.04	Inch
Wick Thickness	0.10	Inch
Effective Length	0.2896	Foot
Effective Pore Radius	1.0E-2	Inch
Permeability	1.64E-9	Sq Ft

The relative effect of the slot variables, the number of slots, the slot thickness, and the thread density are shown in Figure 3. The results indicate that heat rate increases with decreasing thread density. Although this trend can be expected to reverse as the thread density approaches zero, no indication was noted in the range investigated. The number of slots also has a major effect: as the number of slots is increased, the heat flux increases. Again the trend can be expected to reverse, in this case as the area slotted approaches a significant portion of the evaporator and decreases the wetted or liquid flow area. This effect was included in the model but does not indicate a significant effect. The slot thickness has no significant effect in the range investigated; the thickness was not an effective variable. As the slot size is further decreased, however, slot viscous effects will become larger, increasing the pressure drop and decreasing the performance.

The effect of the conventional variables is shown in Figure 4. Of these the most effective is pore radius. The heat rate varies directly with permeability and wick thickness and inversely with pore radius and effective length. These findings are typical for most heat pipes.

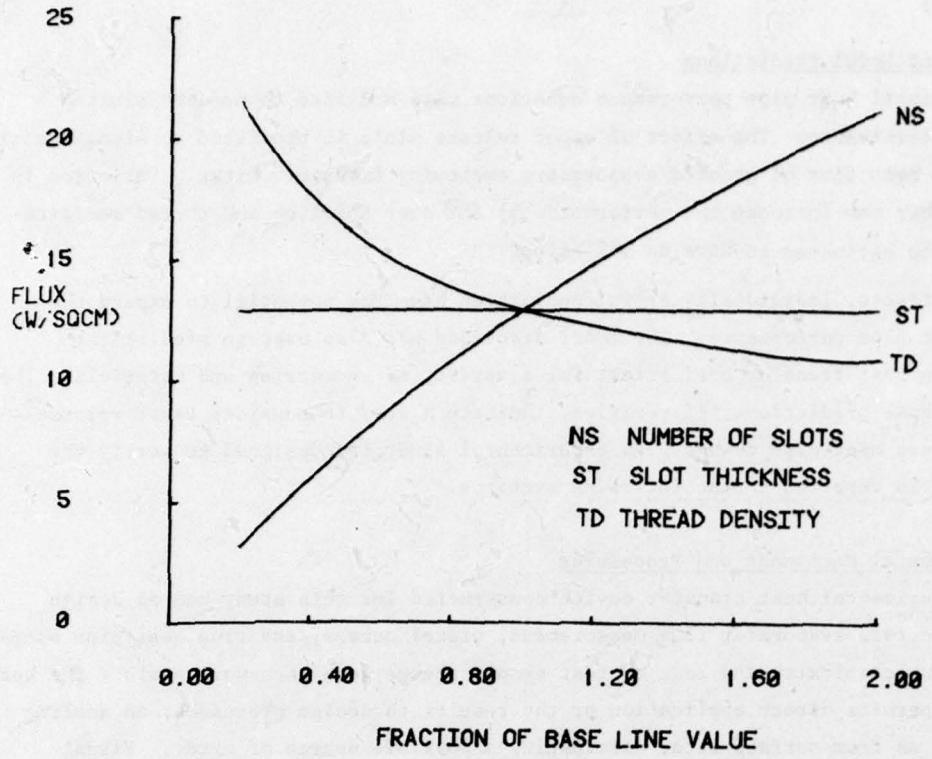

Figure 3. Relative Effect of Variable Changes for Inverted Meniscus Operation

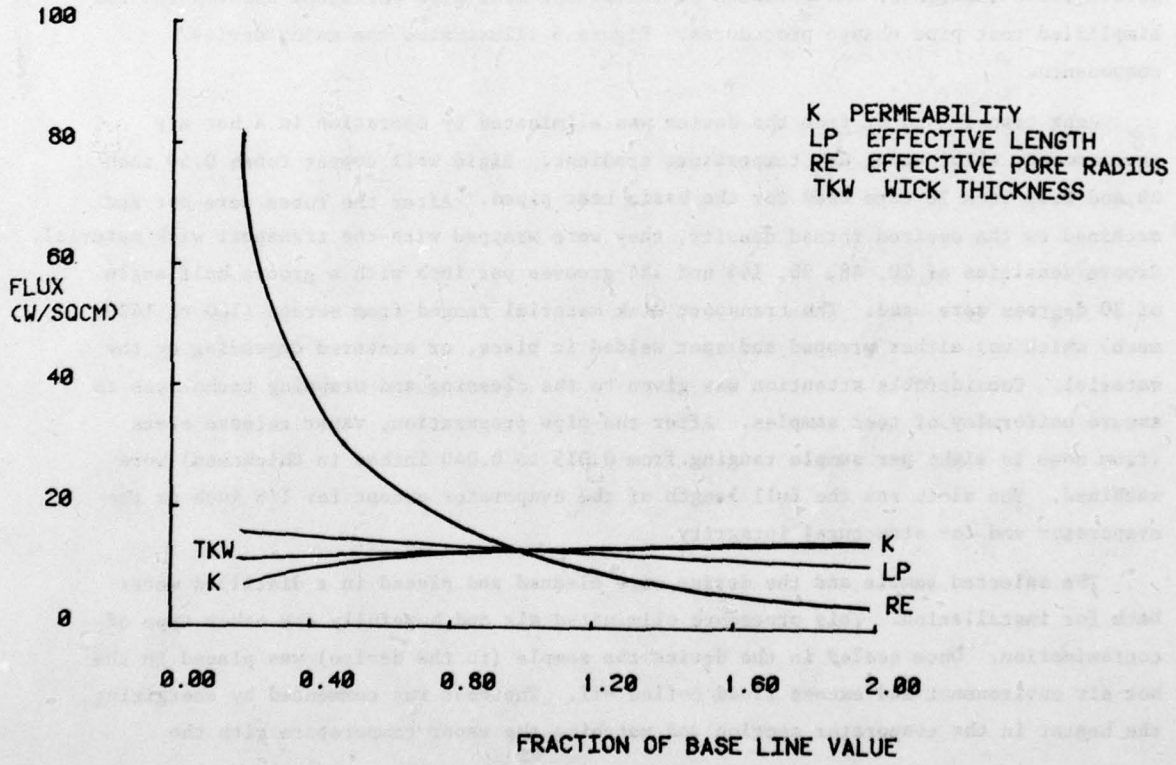

Figure 4. Relative Effect of Conventional Variable Changes

V. Summary of Model Predictions

Conventional heat pipe performance equations were modified to predict slotted evaporator performance. The effect of vapor release slots is predicted to significantly increase the heat flux of grooved evaporators employing transport wicks. Variation in the slot number can increase the performance by 80% over baseline and thread modifications are also estimated to have an 80% effect.

These effects, individually or in combination, have the potential to expand the range of heat pipe performance. The model described was also used to predict the corresponding heat transfer coefficient for a variety of geometries and materials. The results of these predictions, if verified, indicate a need to consider vapor release slots in future heat pipe design. An experimental study was designed to verify the model and it is reported in the following sections.

VI. Experimental Equipment and Procedures

The experimental heat transfer device constructed for this study had as design criteri a accurate evaporator flux measurement, visual access, and true heat pipe operation. Minimum complexity and ease of test sample change were secondary goals. The heat pipe design permits direct application of the results to design processes; no scaling is required, as from surface data, eliminating a possible source of error. Visual access was desired to permit observation of the operating characteristics as well as groove fluid locations. An inverted or inside-out heat pipe permitted observation and simplified test pipe change procedures. Figure 5 illustrates the major device components.

Heat transfer to or from the device was eliminated by operation in a hot air environment, eliminating any temperature gradient. Rigid wall copper tubes 0.50 inch OD and 0.43 inch ID were used for the basic heat pipes. After the tubes were cut and machined to the desired thread density, they were wrapped with the transport wick material. Groove densities of 20, 48, 96, 144 and 184 grooves per inch with a groove half angle of 30 degrees were used. The transport wick material ranged from screen (100 to 1400 mesh) which was either wrapped and spot welded in place, or sintered depending on the material. Considerable attention was given to the cleaning and wrapping techniques to assure uniformity of test samples. After the pipe preparation, vapor release slots (from none to eight per sample ranging from 0.015 to 0.040 inches in thickness) were machined. The slots ran the full length of the evaporator except for 1/8 inch at the evaporator end for structural integrity.

The selected sample and the device were cleaned and placed in a distilled water bath for installation. This procedure eliminated air and hopefully any other type of contamination. Once sealed in the device the sample (in the device) was placed in the hot air environment and excess fluid boiled off. The test run commenced by energizing the heater in the evaporator section and matching the vapor temperature with the

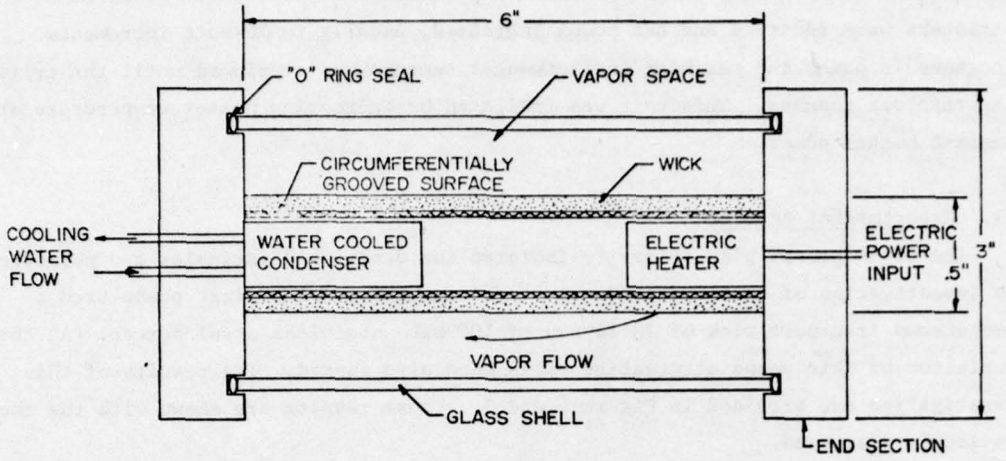

Figure 5. Schematic of the Experimental Heat Transfer Device

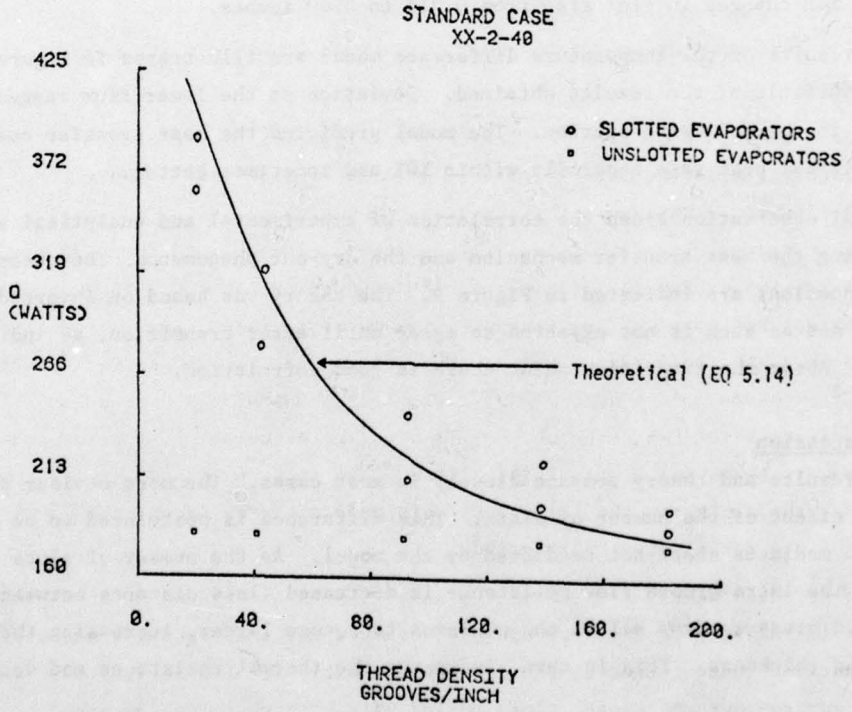

Figure 6. Comparison of Experimental Results with Theory for Groove Densities Investigated

environment. Once steady state operation was achieved at the lowest power setting all parameters were recorded and the power increased, usually in 20-watt increments. Increases in power and matching environmental temperature continued until the critical heat rate was reached. This rate was indicated by increasing heater temperature at constant heater power.

VII. Experimental Results

The experimental plan primarily isolated the designated variables and permitted the investigation of each independently. The samples for the first phase used a homogeneous transport wick of 10 layers of 100 mesh stainless steel screen. At the completion of this phase alternative wicks were also tested. The results of this investigation are provided in Figures 6 and 7. These results are shown with the theory previously discussed.

Figure 6 illustrates the theoretical and experimental results for a variation of groove density. Decreasing density results in increased flux, although not quite as much as predicted. Perhaps the most noticeable result is the uniform low flux values for unslotted evaporators. The variation due to the number of slots is shown in Figure 7. The developed theory did not accurately predict the results and an adjustment using an empirical relationship involving the number of slots is also shown. The data indicate a peak flux after which a decrease occurs. There was no measurable variation for changes in slot size from 0.015 to 0.40 inches.

The results of the temperature difference model are illustrated in Figure 8, which is characteristic of the results obtained. Deviation at the lower flux ranges is discussed in the following section. The model predicted the heat transfer coefficient at the critical heat rate generally within 10% and sometimes better.

Visual observation aided the correlation of experimental and analytical results in establishing the heat transfer mechanism and the dry-out phenomenon. The observed menisci locations are indicated in Figure 9. The theory was based on inverted meniscus operation and as such is not expected to agree until after transition, as indicated in Figure 8. Above the transition point there is good correlation.

VIII. Discussion

The results and theory compare closely in most cases. The most obvious deviation is in the effect of the number of slots. This difference is postulated to be due to changes in meniscus shape not predicted by the model. As the number of slots is increased the intra-groove flow resistance is decreased (less distance between slots); the reduced pressure drop allows the meniscus to become larger, increasing the effective liquid thickness. This in turn increases the thermal resistance and decreases

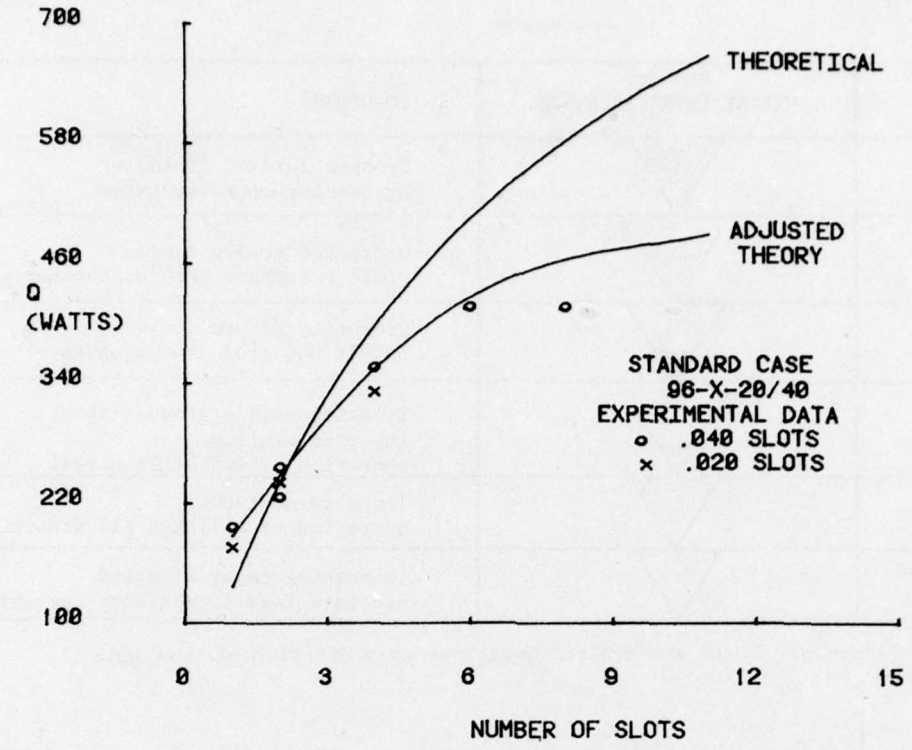

Figure 7. Comparison of Experimental Results with Theory for Various Numbers of Vapor Release Slots

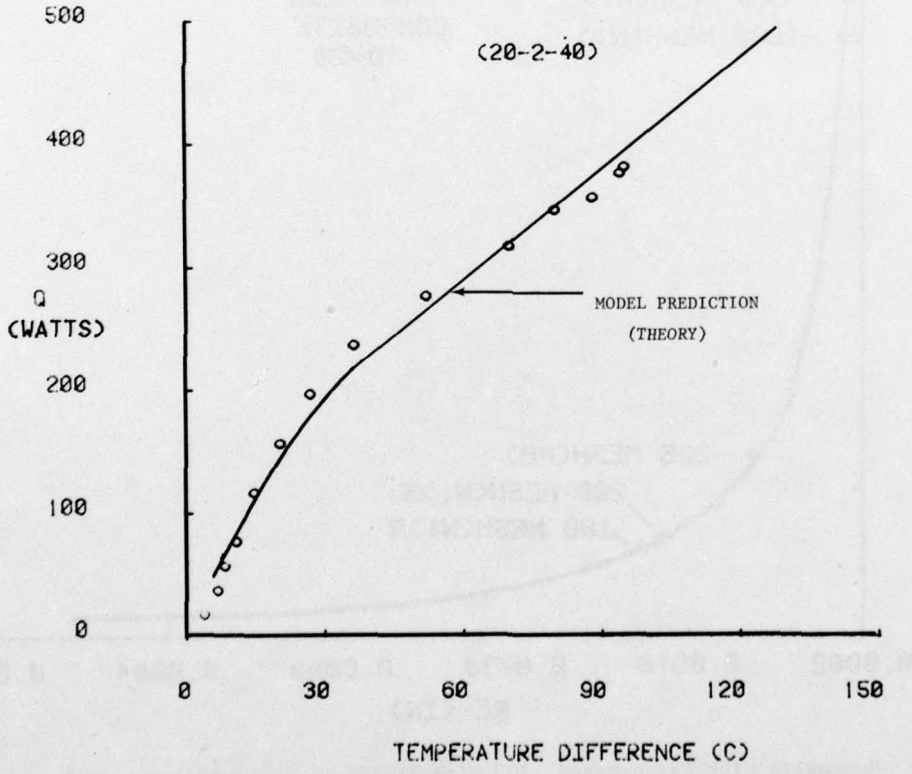

Figure 8. Comparison of Experimental Results with Model Predictions for a Heat Pipe with 20 Grooves per Inch and Two .040 Inch Vapor Release Slots

HEAT FLUX	GROOVES VISUAL REPRESENTATION	COMMENTS
None		Grooves full of fluid, Evaporator wick saturated
Low		Decreased groove fluid, Fluid recession into evaporator wick
Moderate		Decreased groove fluid Bubble ejection from grooves
Transition		Transition: some grooves in inverted meniscus operation, others still normal
Increased		Inverted meniscus operation established all grooves
Approaching Dryout	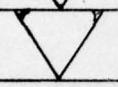	Increasing vapor flow and pressure lead to meniscus recession

Figure 9. Fluid and Menisci Locations as a Function of Heat Rate

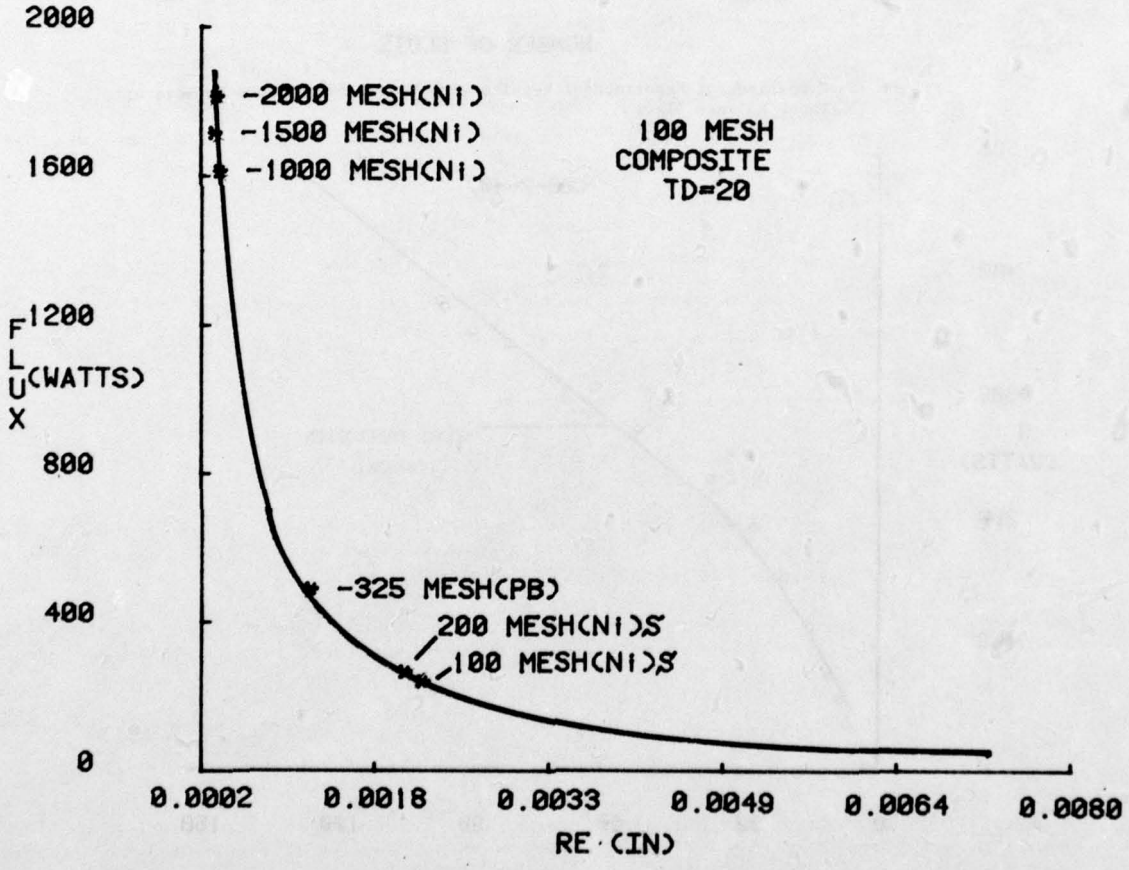

Figure 10. Composite Wick Performance, 100 Mesh Exterior, 20 Grooves per Inch, Four .040 Inch Vapor Release Slots

the flux achievable. The adjustment technique supports this phenomenon but still does not show the decrease, which is postulated to be due to the loss in wetted evaporator areas exceeding the gains due to decreased groove pressure losses.

The overall predictions of the critical heat rate and the corresponding heat transfer coefficient compare favorably with the experimental results, apparently validating the proposed mechanism.

After the basic variables were investigated several higher flux samples were constructed and evaluated to check the model validity in this range. Composite wicks, permitting a combination of permeability and pore radius not achievable by homogeneous wicks, were used. The individual adjustment of these parameters independently leads to predicted high flux wicks. Figure 10 is characteristic of the results for a 100-mesh evaporator with varying mesh transport wicks. In general, for composite wicks, the flux was slightly underestimated but the heat transfer coefficient was predicted within 4% for the samples tested.

IX. Conclusions

The results indicate that the primary mechanism of heat transfer in the evaporator of an inverted meniscus heat pipe is conduction through a thin liquid layer. The correlation supports this conclusion even though the exact liquid layer geometry and changes with slot configuration were not established. The critical heat rate was found to be wick limited.

The inclusion of slots in the transport wick increased the performance significantly over non-slotted samples. Results indicated that the slot thickness was larger than necessary and that a maximum is reached as the number of slots is increased. These results should be considered in future heat pipe designs, since performance was enhanced with no detrimental results.

References

1. Feldman, K. T. and S. Munje. "Experiments with Gravity Assisted Heat Pipes with and without Circumferential Grooves." Paper 78-378, presented at the 3rd International Heat Pipe Conference, Palo Alto, California, 22-24 May 1978, p. 15.

2. Schlitt, K. R. "Development of an Axially Grooved Heat Pipe with Non-Constant Groove Width." Paper 78-375, presented at the 3rd International Heat Pipe Conference, Palo Alto, California, 22-24 May 1978, p. 1.

3. Saaski, E. W. Investigation of an Inverted Meniscies Heat Pipe Wick Concept. NASA CR-137-724, 1975.

4. Feldman, K. T. "The Heat Pipe: Theory, Design and Applications." In Heat Pipe Technology, Short Course and Workshop presented by The College of Engineering and The Technology Applications Center, The University of New Mexico, Albuquerque, 5-9 January 1976.

5. Winters, E. R. F. and W. O. Barsch. "The Heat Pipe." Advances in Heat Transfer, Vol. 7 (1975), 219-320.

6. Oliver, R. C. and K. T. Feldman, Jr. Investigation of Evaporation from Ground Inverted Meniscus Heat Pipe Wicks. TR-ME-79 (77) KAFB-470-1. University of New Mexico, Bureau of Engineering Research, April 1977, pp. 90-91.

7. Barthelemy, R. R. "Evaporation Heat Transfer in Heat Pipes." Thesis, Ohio State University, 1975.

SECTION IV

PROPULSION

EVALUATION OF A GLUHAREFF PRESSURE JET

H. M. Brilliant*

Abstract

This paper discusses the analysis and testing of a Gluhareff pressure jet engine. The data collected during two test runs of the engine are compared with the manufacturers' claimed performance and theoretical performance predictions. Future modifications of the present test configuration and suggestions for future tests are discussed.

I. Introduction

Turbine engines (turbojets, turbofans, etc.) in the Air Force inventory are expensive and complicated. Even a small, low-cost turbojet engine, such as the one being developed by Elrod, Wright, and Wilkenson (Ref. 1) for a 200 lb_f (1kN) thrust class, will be complicated (they have taken a turbo-supercharger and added an inlet, combustor, and exit nozzle). A ramjet engine is considerably simpler, but has a problem developing thrust at low speeds. The Air Force has developed ejector ramjet and ducted rockets to overcome this problem. Because of fuel pumps or other extra equipment as well as the engine itself, these systems are still expensive.

In the early 1970's, Mr. Eugene M. Gluhareff, working independently of the Air Force, began development of an alternative system for a lightweight, inexpensive jet engine. He called his engine a pressure jet, but it is really a modified ejector ramjet. It was designed to produce thrust of 20, 40, or 80 lb_f depending on the size of the model, with the smallest engine, the G8-2-15, weighing only 5.5 lb_f.

In 1977, the United States Air Force Academy (USAFA) bought a G8-2-15 engine to test in the propulsion facilities. The purpose of the project was to evaluate the engine and its components. The project started as a theoretical analysis performed by Cadet Douglas N. Barlow** for an Aero 462 (Propulsion II) project. The next semester he built the engine from a kit with the help of the Academy's Civil Engineering Division. The cost of the kit without accessories was approximately $400.00. Accessories (fuel tank, ignition system, etc.) cost another $250.00. In 1978, Cadet John C. Omahen** and Mr. Fred E. Jayne*** designed and built the test set-up and stand. In 1979, the engine was run approximately five times for course demonstrations in Aero 450 (Aeronautical Laboratory).

---

*Captain, USAF, Associate Professor of Aeronautics, DFAN

**Cadet, USAFA, presently 2nd Lt, USAF

***Engineering Technician, DFAN

This report represents a progress report of work performed to date, with some results and some suggestions for future work.

II. Description of Engine Operation

The Gluhareff pressure jet is basically an ejector ramjet which runs on propane as fuel. A schematic of the engine is shown in Figure 1. The basic parts of the engine are the fuel tank, throttle, heat exchanger coil, supercharger system, combustion chamber with an ignition system, and the exit nozzle.

The fuel tank houses the propane and feeds the fuel to the engine. Because, at room temperature, propane has a vapor pressure of approximately 125 psia, the tank is self-pressurizing; therefore, no fuel pump is required. This is why Mr. Gluhareff calls the engine a "pressure jet" and is part of the reason the engine is so simple. The propane is removed from the fuel tank as a liquid so rapid pressure reduction in the tank does not occur.

From the fuel tank, the propane flows through a needle valve throttle, which controls the flow rate, to the heat exchanger coil. The coil is housed in the combustion chamber so that, when the engine is operating stably, the propane is vaporized and heated to approximately 1000°F (Ref. 2).

The high temperature, high pressure propane then goes to the supercharger system. The fuel has cooled to 600°F by the time it arrives at the supercharger. This supercharger system is basically an ejector system, which is used in ramjets to supplement ram compression so that the engine can operate statically. The fuel is first accelerated to a supersonic speed through a convergent-divergent (CD) nozzle. At this speed the static pressure of the fuel flow is lower than the atmospheric pressure so the propane stream entrains air. The three stages of supercharging are designed to produce a near stoichiometric fuel-air mixture in the combustor. The major difference between this supercharged pressure jet and an ejector ramjet is that the inlet in the pressure jet is designed to let in air from the side so that there will be no ram compression if the engine is moving. This substantiates the Air Force's experience with ejector systems, which showed reduced performance of ejector ramjets as the vehicle using the engine moved faster. This supercharger system is also part of the reason that the engine is so simple.

From the supercharger, the fuel-air mixture flows into the combustor. Here, the side-mounted intake design is most important. Combustion requires a low velocity recirculation zone for flame stabilization. The dome ahead of the inlet to the combustor does this job (Figure 2). If the inlet were in front rather than to the side, there would have to be a more complicated means of flame stabilization. The fuel is ignited by the ignition system, a simple spark ignitor fed by a 23,000 volt supply. Once the mixture is burning, the ignition is not needed to maintain combustion except when the flame is blown out.

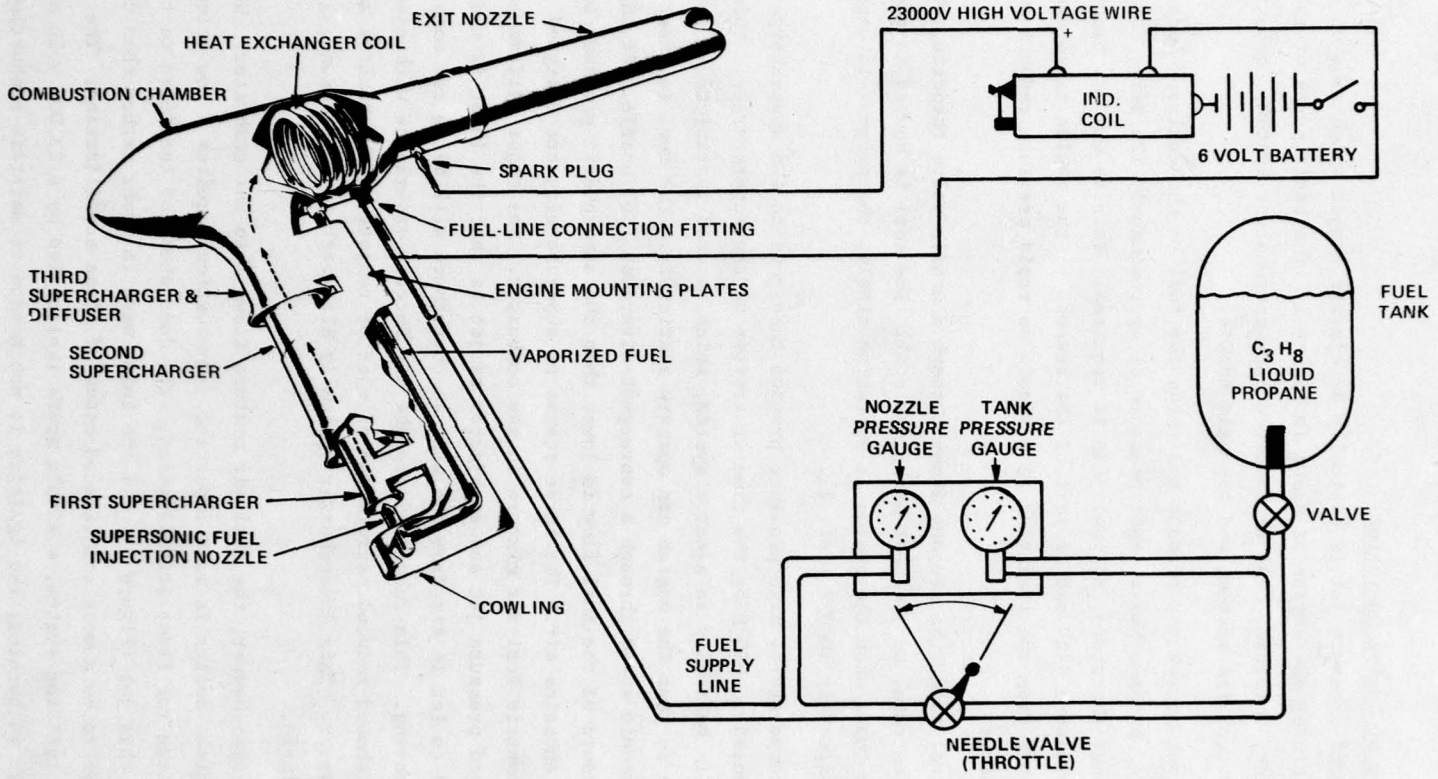

Figure 1. Schematic Diagram of the Gluhareff Pressure Jet (Ref. 2 and 3)

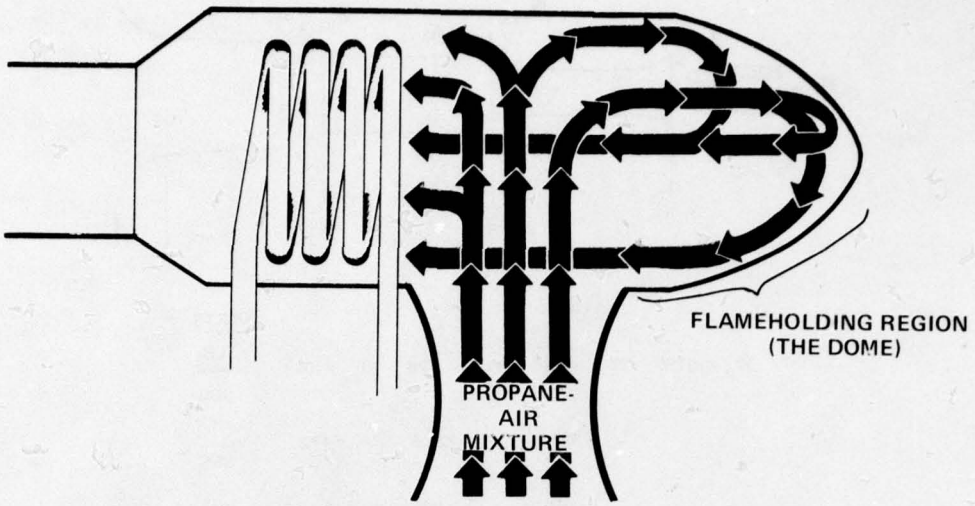

Figure 2. Flameholding in the Combustor

From the combustor, the products of combustion go through a convergent nozzle. The end of the nozzle is supposed to be V-notched as shown in Figure 1. In our preliminary tests, this was not done. The designer claims that this notch will reduce the noise level by about one-half and increase thrust by 3 lb_f (Ref. 3).

III. Theoretical Analysis

The primary analysis performed on the engine was on the supercharger system and the exit nozzle. This work was performed by Cadet Barlow as an application of equations studied in two propulsion courses and has been updated for this report. At the time of the studies, no good methods for accurate calculations of heat exchanger and combustor operations were available.

A. Supercharger System

The supercharger system as mentioned above is divided into three stages. The equations used for analysis of this system were developed by Dr. Oates (Ref. 4). The primary assumption in the analysis was that complete mixing occurs so that uniform gas streams enter and exit each stage. While this assumption was not satisfied, it did provide a good starting point for analysis. Testing could be performed to check the validity of the assumption and provide data for future analysis.

The goal of this analysis was to determine the total pressure of the gas exiting the supercharger system. The analysis was performed for the engine operating at sea level (standard day) with a nozzle total pressure of 95 psia and a nozzle total temperature of 1060°R. At this condition, the designer claimed that the engine produces 8 lb_f of thrust. The input to each stage was obtained from G8-2 Technical Handbook (Ref. 2), as shown in Figure 3.

AD-A075 419 AIR FORCE ACADEMY CO F/G 20/4
AIR FORCE ACADEMY AERONAUTICS DIGEST. SPRING 1979.(U)
JUL 79 E J JUMPER, M M TOWE
UNCLASSIFIED USAFA-TR-79-7 NL

2 OF 2
AD
A075419

END
DATE
FILMED
11-79
DDC

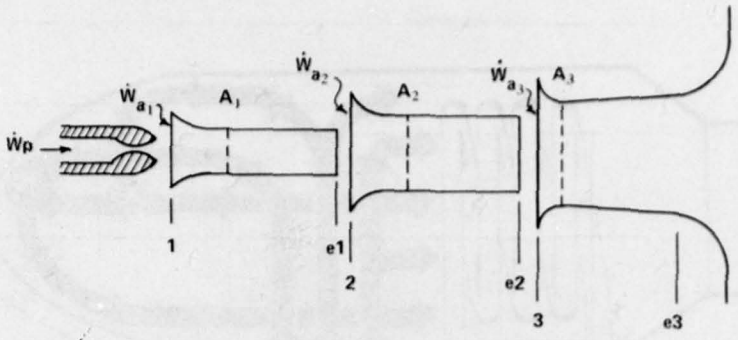

				UNITS
$\dot{W}_p = .0195$	$\dot{W}_{a_1} = .115$	$\dot{W}_{a_2} = .129$	$\dot{W}_{a_3} = .041$	$-\frac{LB_f}{SEC}$
	$V_1 = 384$	$V_2 = 225.5$	$V_3 = 172$	$-\frac{FT}{SEC}$
	$A_1 = 0.66$	$A_2 = 2.20$	$A_3 = 3.30$	$-FT^2$

Figure 3. Supercharger Parameters (Ref. 2)

The inputs and results of the analysis for each stage are shown in Table 1. The mass flow ratios shown in Table 1 were obtained from Figure 3. The value of the specific heat ratio, γ, in the table is an average value based on the average properties of the gas leaving the stage. A conservative assumption was that the flow from the CD nozzle encountered a normal shock wave prior to entering the mixing section. The exit static pressure was varied until the exit velocity of the mixture (V_e) agreed with the results of Figure 3. The net result of the analysis was that the total pressure exiting the supercharger/diffuser was 15.69 psia.

B. Nozzle Calculations

The combustion gases entering the exit nozzle were assumed to have a total pressure of 15.69 psia (i.e., the same as leaving the supercharger) and a total temperature of 4060°R. While there should be some loss of total pressure in the burner due to combustion and turning and viscous losses, it was assumed to be small because of the low velocity of the gases entering the combustor. The value for the total temperature was probably high; it was obtained from the G8-2 Technical Handbook because we had no procedure for calculating it accurately. The properties of the products of combustion were $\gamma = 1.286$ and $R = 1714 \frac{ft - lb_f}{slug - R}$.

The exit conditions were obtained from a standard exit nozzle analysis (see Ref. 4). Since the nozzle was convergent and the velocities were relatively low, the nozzle flow was assumed to be unchoked with the exit static pressure equal to atmospheric pressure. From the static to total pressure ratio, the Mach number was determined to be .320 and the exit velocity was 950 ft/sec.

Table 1

SUPERCHARGER ANALYSIS

a. Inputs

STAGE	WEIGHT AND MASS FLOW RATIO	TOTAL TEMPERATURE RATIO	TOTAL PRESSURE RATIO	γ	M_{in}	$\frac{p_e}{p_{t_{in}}}$
1	$\frac{\dot{W}_{a_1}}{\dot{W}_p} = 5.90$	.5	.2333	1.335	.536	varied
2	$\frac{\dot{W}_{a_2}}{\dot{W}_{e_1}} = .959$	≈ 1	.9313	1.366	.361	varied
3	$\frac{\dot{W}_{a_3}}{\dot{W}_{e_2}} = .156$	≈ 1	.9327	1.370	.206	varied

b. Outputs

STAGE	$V_{a_{in}} \frac{FT}{SEC}$	p_{t_e}(psia)	$V_e \frac{FT}{SEC}$	T_e (°R)
1	111.6	15.78	384.0	$\approx$ 530°R
2	166.9	15.76	225.5	$\approx$ 530°R
3	68.6	15.69	172.0	$\approx$ 530°R

The thrust was calculated by multiplying the total mass flow (.305 lbm/sec) times the exit velocity. This yielded a thrust of 9.0 lb_f. This is slightly higher than the 8 lb_f claimed. The assumptions for the total pressure and temperature entering the nozzle could explain the difference.

IV. Experimental Results

A. Test Set-Up

Figure 4 shows the test stand built to house the engine and required instrumentation. The preliminary design was done by Cadet John C. Omahen. The test stand and instrumentation were built by Mr. Fred Jayne. The set-up was built on a portable cart so that it could be operated in the test cell or outside of the building.

The engine was mounted on a hinge so that it could rotate freely and transmit a force to a calibrated load cell. The calibration results are shown in Figure 5. During calibration a hysteresis error was noted at less than 1%, but a slight zero shift was noted ($< 2\%$). During engine operation, these errors increased: hysteresis, 5-10% ; and

a zero shift greater than 5%. After some refinements, the zero shift was reduced to approximately 5% of full-scale deflection. The averages of the zero thrust levels before and after the run were used to determine the thrust. All thrust data were recorded on strip charts.

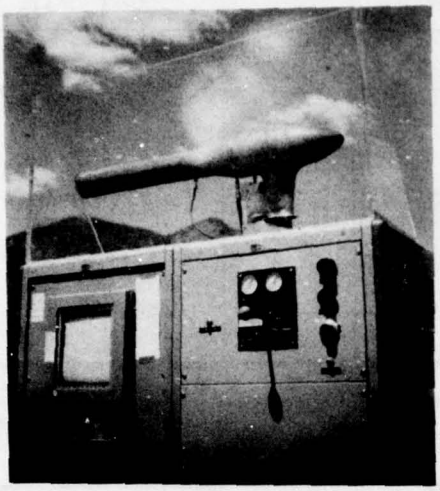

Figure 4. Photograph of the Engine and Test Stand

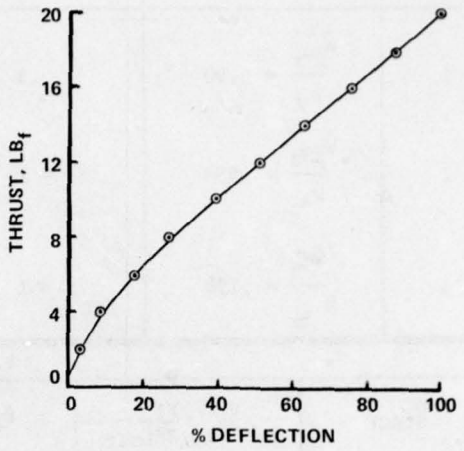

Figure 5. Thrust Calibration Curve

The only other measurements were two pressures. One was the tank pressure and was used to sense the rate that the propane vaporizes. It read 122 psig during operation; the ambient temperature was 65°F. The second pressure, the nozzle total pressure, was measured downstream of the throttle ahead of the heat exchanger. It was used to sense fuel flow rate (this will be discussed in more detail below).

B. Test Results

The test results are summarized in Table 2. The data were taken by various cadets enrolled in Aero 450 during two test periods on different days. The measured "nozzle" pressure and percent deflection were recorded during these tests. The remainder of the results presented was obtained from these data. During the two days, the air temperature varied from 45°F to 65°F. A third day of operation was cancelled because the engine would not operate above idle; on that day, the air temperature was below 40°F.

Because the "nozzle" pressure was measured ahead of the heat exchanger, as shown in Figure 1, it had to be corrected for losses due to friction, heat addition, and vaporization. The total effect of these losses was approximated to be 5% of the absolute pressure. Corrected values are shown in Table 2.

Table 2
TEST RESULTS

MEASURED "NOZZLE" PRESSURE (psig)	PERCENT DEFLECTION (THRUST)	CORRECTED NOZZLE PRESSURE (psig)	THRUST (LB_f)	MASS FLOW RATE (LB_M/HR)	TSFC $\left(\frac{LB_M/HR}{LB_f}\right)$
* 60	3	56	1.8	61.6	34.2
+ 65	10	61	4.3	65.9	15.3
+ 67	15	63	5.6	67.7	12.1
* 80	5	75	2.6	78.9	30.4
+ 83	45	78	11.0	81.5	7.4
+ 95	50	90	11.8	91.9	7.8
*100	35	94	9.3	96.3	10.4
+105	60	99	13.4	100.6	7.5
+105	70	99	15.1	100.6	6.7
*110	40	104	10.2	104.9	10.3

Barometric pressure - approximately 11.3 psia
Air temperature - approximately 65°F(+) or 45°F(*)

The mass flow rate was obtained using

$$\dot{m} = \frac{p_t}{\sqrt{RT_t}} \sqrt{\gamma} M \left[1 + \frac{\gamma-1}{2} M^2\right]^{-\left(\frac{\gamma+1}{2(\gamma-1)}\right)}$$

evaluated at the supercharger fuel injection nozzle, where the propane is a gas. The nozzle throat diameter was 0.13 in. (i.e., area, A, was 0.0133 in^2). The nozzle total temperature (T_t) was assumed to be 1060°R as discussed earlier. The Mach number, M, at the throat of the CD nozzle was 1.0, since the nozzle was choked. For propane (assumed to be a calorically perfect gas), $R = 1127 \frac{ft - lb_f}{slug - R}$ and $\gamma = 1.2$. The nozzle total pressure (p_e) used was the corrected value obtained from test data. Because all the other parameters in the mass flow rate equation were constant, the nozzle total pressure was a direct measure of the propane flow rate.

The thrust specific fuel consumption (TSFC) (simply, the mass flow rate in lb_m/hr divided by the thrust in lb_f) was used as an indicator of the overall efficiency of the engine. The TSFC for the tests is shown in Table 2. For comparison, a modern turbojet at full throttle has a TSFC below 1 $lb_m/hr/lb_f$.

C. Discussion of Results

The results for thrust versus nozzle pressure are presented in Figure 6. These results are compared with data presented in the G8-2 Technical Handbook (Ref. 2). The handbook data have been multiplied by the ratio of atmospheric pressure at the USAFA to that at sea level to correct for altitude effects; these effects should reduce the air mass flow rate and, thus, the thrust. As shown in Table 2 and in Figure 6, there appear to be two levels of performance to the engine for the two days of operation. Drifts in the load cell between the two days could not account for this since the load cell was rezeroed and recalibrated on the second day and no change was noted in the calibration curve from the first day to the second day. The two levels of performance appear to be related to the air temperature; the engine operated better on the hotter day. In fact, on a very cold day, the engine would not operate above idle (nozzle pressure of 60 psig); whenever the throttle was advanced to increase the nozzle pressure, the flame would blow out. Generally, our engine performed better than the designer claimed, and, in fact, this result is surprising since a V-notched exit is supposed to increase the thrust (Ref. 3) and we did not notch our nozzle.

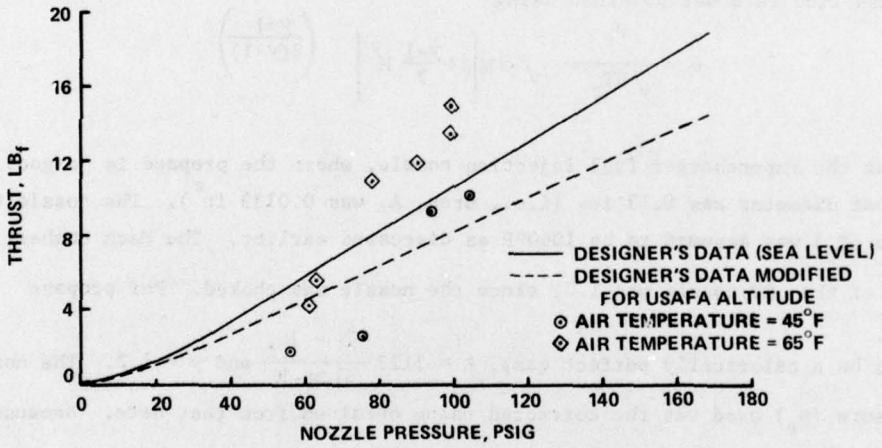

Figure 6. Thrust versus Nozzle Pressure

The TSFC versus thrust is shown in Figure 7. Again, two levels of performance are obvious. The TSFC decreased as the thrust increased. At all conditions, the TSFC was very high compared to turbojet engines, a not-so-surprising result since the designer's only claims for the engine were that it is lightweight and low costing. He did not claim fuel economy.

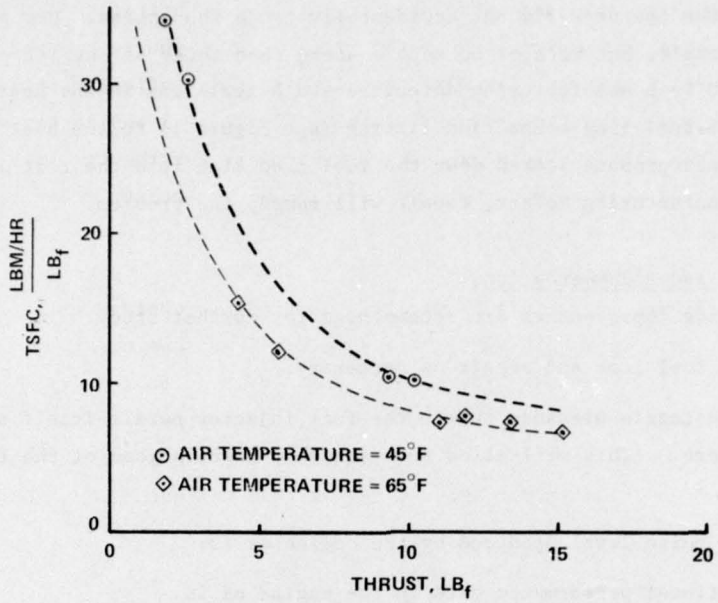

Figure 7. TSFC versus Thrust

D. Additional Comments on Engine Operation

In addition to thrust and TSFC, two engine characteristics were also noted: noise generation and ease/safety of operation.

The noise generated by the engine was significant. While the engine was operating, all people in the vicinity had to wear ear protectors. The engine could be heard a mile away. The sound was typical of combustion screech, caused by rotating detonations in the combustor. While no noise level measurements were taken, the engine probably exceeded safe noise levels for general use. The V-notched tailpipe is claimed to cut the noise in half (Ref. 3); this should be checked out in future testing. If the majority of the noise is due to screech, however, we would expect no significant reduction from V-notching the tailpipe.

The engine is not easy to operate; it must be allowed to warm up for a minute or more before operating stably. Even then, flame-out on throttle advance was experienced on cold days. On warmer days, the throttle could be advanced without flame-out, but only slowly. The throttle was extremely sensitive, and settings between idle and full power were extremely difficult. Future use of the engine will require a new throttle.

The following safety of operation characteristics were noted. The most telling consideration was that during operation, the combustor section was noted to be glowing-red, indicating extremely high temperatures. Melting did not occur, however, and from

the appearance of the glow, the engine appeared to reach a steady state temperature. Even if melting should occur, because of the low combustor pressures, no explosion would be expected. The main safety consideration related to the metal temperature was to insure that the operator did not accidentally touch the engine. Hot gases were ejected from the exit nozzle, but were of no more concern than those of any jet exit stream. What appeared to be a manufacturing defect caused a fuel leak in the heat exchanger; the weld for the fuel-line connection fitting (see Figure 1) to the heat exchanger cracked and liquid propane leaked down the fuel feed line into the test stand. If this was simply a manufacturing defect, repair will remedy the problem.

V. Conclusions and Recommendations

The following improvements are recommended for further study:

1. Examine the fuel leak and repair as necessary.

2. Relocate the nozzle pressure tap to the fuel injector nozzle itself and add a thermocouple there. (This will allow more accurate calculations of the fuel mass flow rate.)

3. Measure the noise level produced by the engine as is.

4. Obtain additional performance data on the engine as is.

5. Add a V-notch to the tailpipe and test for performance and noise. (This should be done only after there are enough experience and data obtained without the notch per recommendations 3 and 4.)

6. Study the supercharger system by measuring the total pressure profile at the end of each stage.

7. Replace the throttle valve if it continues to be sensitive.

While we would be somewhat reluctant to recommend this engine for use in any applications recommended by its designer (Ref. 5), the engine is ideal as a learning tool for alternative propulsion systems. It could also be used as a vehicle to demonstrate problems of measurement in high temperature environments, including measurements of metal temperature, exhaust gas temperature, pressure, and combustion products.

Acknowledgement

The author wishes to thank Captain C. H. Steiling, who "discovered" the engine in an advertisement in Popular Science.

References

1. Elrod, W. C., M. E. Wright, and D. B. Wilkinson. "The Development of a Low Cost Turbojet Engine in the 1 kN Thrust Class." AIAA Paper 78-966, presented at the 1978 AIAA/SAE 14th Joint Propulsion Conference, Las Vegas, Nevada, 25-27 July 1978.

2. EMG Engineering Co. G8-2 Gluhareff Pressure Jet Engine Technical Handbook. Gardena, CA: EMG Engineering Co., date unknown.

3. Thoms, Wayne. "A Jet You Can Build in Your Own Shop." Mechanics Illustrated, Vol. 71 (January 1975), 28-29.

4. Oates, Gordon C. Notes on Rockets and Airbreathing Engines. Vol 1 & 2. USAF Academy, Colorado, Aeronautics Department, 1976 (Revised Periodically).

5. EMG Engineering Co. Uses of G8-2 Jet. Gardena, CA: EMG Engineering Co., date unknown.

SECTION V

INSTRUMENTATION AND HARDWARE

USAFA-TR-79-7

CALIBRATION OF FIVE-HOLE PROBES FOR ON-LINE DATA REDUCTION

K. W. Barker,* R. W. Gallington,** and S. N. Minster***

Abstract

This paper discusses the calibration of a five-hole conical pressure probe. A computer-aided technique to find the three components of velocity and the static and total pressures is described. The application of this technique to a five-hole probe is described and results given and discussed. An evaluation of the calibration accuracy is also given.

I. Introduction

The problem with measuring flow with any probe is that the probe itself disturbs the flow field. Sometimes the flow disturbance is relatively unimportant and the probes can be large, as is the case with pitot-static tubes on aircraft for airspeed measurement. In most laboratory experiments with relatively small flow test sections, however, size is important as is the number of probes in the flow. For these applications, small probes (1-3mm in diameter) have been constructed with a single forward hole surrounded by a number of holes on a conical surface eminating from the forward hole. This paper concerns itself with the calibration of small five-hole conical probes (i.e., four holes on the conical surface surrounding the center hole).

The objective of any five-hole conical probe calibration scheme is to develop explicit equations for the desired outputs of total and static pressure, angle of attack (α), and angle of sideslip (β) as functions of measurable probe pressures. Breyer and Pankhurst (Ref. 1) describe this type of calibration. The calibration involves describing the desired explicit functions by polynomials in two pressure coefficients which are roughly proportional to the two flow angles, α and β.

Finding the pressure coefficients to best fit a large data set was once a tedious procedure fraught with the possibility of human error. Computer-aided data acquisition has the ability to collect data and at the same time perform large matrix operations on it. With the advent of these computer data collection techniques, finding the calibration coefficients has become much more practical. This paper describes one such computer-aided five-hole conical probe calibration scheme.

Because of their very small size, all probes have manufacturing imperfections which require unique calibration of each probe. The pressure coefficients of calibration polynomials are essentially, then, the unique calibration constants of the probe.

---

*Cadet, USAFA, presently 2nd Lt, USAF, Eglin AFB, FL

**Lt Col, USAF, Associate Professor of Aeronautics, DFAN

***Cadet, USAFA, presently 2nd Lt, USAF, DFAN

An example of the type of five-hole probe the technique described here can be applied to can be found in Reference 2. Application of the technique with fourth-order polynomials using probes from Reference 2 produced accuracies of ± 1 degree in flow angles, $\pm 2\%$ in dynamic pressure, and $\pm 2.5\%$ in total pressure for flow angles of up to 28° off probe axis. The certainty of measurement was 95%.

II. Theoretical Section

A. Theory

We must first define four pressure coefficients in terms of the coordinate system shown in Figure 1. The figure shows the end of the pressure probe (showing only the forward hole). For a given test, the sting angle, θ (angle the flow or velocity vector makes with the probe axis), and the roll angle, ϕ (describing the orientation of the four holes on conical surface), are fixed. The direction cosines of the velocity vector with respect to the probe can then be written in terms of θ and ϕ as follows:

$$u/V = \sin\theta \sin\phi \tag{1}$$

$$w/V = \sin\theta \cos\phi \tag{2}$$

where the y direction cosine is given by u/V, u being the y component of velocity with respect to the probe axis, V being the magnitude of the velocity, and the z direction cosine is given by w/V, w being the z component of velocity with respect to the probe axis.

Four pressure coefficients can be defined in terms of the pressures measured from each of the five holes or pressure ports.

$$C_a = \frac{(P_3 - P_1)}{\left[3(P_5 - \frac{1}{4}P_\Sigma)\right]} \tag{3}$$

$$C_b = \frac{P_2 - P_4}{\left[3(P_5 - \frac{1}{4}P_\Sigma)\right]} \tag{4}$$

$$C_o = \frac{(P_o - P_5)}{(P_5 - \frac{1}{4}P_\Sigma)} \tag{5}$$

$$Cq = \frac{(P_5 - \frac{1}{4}P_\Sigma)}{(P_o - P_\infty)} \tag{6}$$

where P_1 through P_5 are the pressures obtained from pressure ports 1 through 5 shown in Figure 2; P_Σ is the sum of P_1, P_2, P_3 and P_4; P_o is the tunnel total pressure; and P_∞ is the tunnel static pressure.

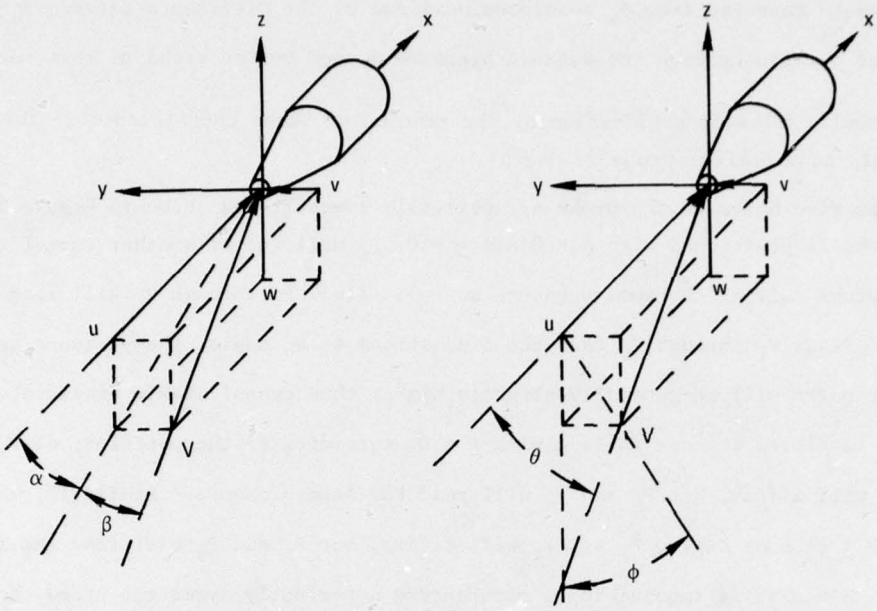

$u = V \cos \alpha \cos \beta$
$v = V \sin \beta$
$w = V \sin \alpha \cos \beta$

$u = V \cos \theta$
$v = V \sin \theta \sin \phi$
$w = V \sin \theta \cos \phi$

Figure 1. Body-Fixed Coordinate Systems

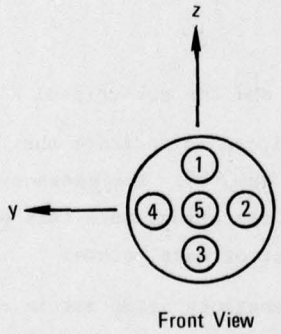

Front View

Figure 2. Port Numbering System

For small angles, the coefficient C_a is roughly proportional to w/V and C_b is roughly proportional to u/V. C_o is the difference between tunnel total pressure and total pressure measured from P_5 nondimensionalized by the difference between P_5 and $\frac{1}{4}P_\Sigma$. C_q provides a ratio between the dynamic pressure sensed by the probe to that measured by the tunnel. A better explanation of the meaning of these coefficients is that their relationship to a perfect probe is useful.

If the five holes on the probe are perfectly symmetric as shown in Figure 2, and if the probe is positioned with $\alpha = 0$ and $\beta = 0$, P_5 will act as another tunnel total pressure probe (giving the same pressure as P_o). Also, P_1 through P_4 will read the same pressure. Since P_1 through P_4 face the free stream at an angle, the pressure sensed by these four ports will be generally slightly higher than tunnel static pressure, P_∞. If the probe is placed at some angle α with $\beta = 0$, according to the positions of P_1 - P_4, P_1 and P_3 will differ, but P_2 and P_4 will read the same pressure. Similarly, when $\alpha = 0$ with β at some angle, P_2 and P_4 will differ, but P_1 and P_3 will read the same pressure. Since it is impossible to manufacture a perfectly symmetric probe, however, a calibration process must be accomplished to provide "correction factors" to convert actual pressures measured to accurate values for u/V and w/V. Experience has shown that a fourth-order curve fit is necessary to calibrate the five-hole probe.

The following is the fourth-order equation for C_o, C_q, u/V and w/V:

$$A = K_{00}^{A} + K_{10}^{A} C_a + K_{01}^{A} C_b + K_{20}^{A} C_a^2 + K_{11}^{A} C_a C_b + K_{02}^{A} C_b^2 + K_{30}^{A} C_a^3 + K_{21}^{A} C_a^2 C_b + K_{12}^{A} C_a C_b^2 + K_{03}^{A} C_b^3 + K_{40}^{A} C_a^4 + K_{31}^{A} C_a^3 C_b + K_{22}^{A} C_a^2 C_b^2 + K_{13}^{A} C_a C_b^3 + K_{04}^{A} C_b^4 \quad (7)$$

where

A = C_o, C_q, u/V, w/V as applicable and the subscripted K's are constants to be solved for. The K's are further superscripted to indicate that they are different for each of the four equations obtainable from Eqn (7). The essence of the calibration process is obtaining these constants. Matrix operations make this process simple and, therefore, are used for reducing a large number of data points.

The method of obtaining the constants using matrix operations is discussed by Neter and Wasserman (Ref. 3). They also discuss how, by solving for the constants

using matrix operations, a least squares fit is automatically incorporated. Nine matrices are required in this calibration process:

$$\left[R\right] = \begin{bmatrix} 1 & C_{a_1} & C_{b_1} & C_{a_1}^2 & C_{a_1}C_{b_1} & C_{b_1}^2 & \cdots & C_{b_1}^4 \\ 1 & C_{a_2} & C_{b_2} & C_{a_2}^2 & C_{a_2}C_{b_2} & C_{b_2}^2 & \cdots & C_{b_2}^4 \\ 1 & C_{a_3} & C_{b_3} & C_{a_3}^2 & C_{a_3}C_{b_3} & C_{b_3}^2 & \cdots & C_{b_3}^4 \\ \vdots & \vdots & \vdots & \vdots & \vdots & \vdots & \vdots & \vdots \\ 1 & C_{a_n} & C_{b_n} & C_{a_n}^2 & C_{a_n}C_{b_n} & C_{b_n}^2 & \cdots & C_{b_n}^4 \end{bmatrix} \tag{8}$$

where the subscripts on C_a and C_b denote the particular data point.

$$\left[u/V\right] = \begin{bmatrix} u/V_1 \\ u/V_2 \\ \vdots \\ u/V_n \end{bmatrix} \qquad \left[K_{u/V}\right] = \begin{bmatrix} K_{u/V_1} \\ K_{u/V_2} \\ \vdots \\ K_{u/V_n} \end{bmatrix}$$

$$\left[w/V\right] = \begin{bmatrix} w/V_1 \\ w/V_2 \\ \vdots \\ w/V_n \end{bmatrix} \qquad \left[K_{w/V}\right] = \begin{bmatrix} K_{w/V_1} \\ K_{w/V_2} \\ \vdots \\ K_{w/V_n} \end{bmatrix} \tag{9}$$

$$\left[C_o\right] = \begin{bmatrix} C_{o_1} \\ C_{o_2} \\ \vdots \\ C_{o_n} \end{bmatrix} \qquad \left[K_{C_o}\right] = \begin{bmatrix} K_{C_{o_1}} \\ K_{C_{o_2}} \\ \vdots \\ K_{C_{o_n}} \end{bmatrix}$$

$$\left[C_q\right] = \begin{bmatrix} C_{q_1} \\ C_{q_2} \\ \vdots \\ C_{q_n} \end{bmatrix} \qquad \left[K_{C_q}\right] = \begin{bmatrix} K_{C_{q_1}} \\ K_{C_{q_2}} \\ \vdots \\ K_{C_{q_n}} \end{bmatrix}$$

The matrix operations discussed by Neter and Wasserman apply to this case through the derivation which follows.

If one uses the u/V matrix

$$\left[u/V\right] = \left[R\right]\left[K_{u/V}\right] \quad . \tag{10}$$

each side is multiplied by the transpose of the R matrix, Eqn (8):

$$\left[u/V\right]\left[R\right]^T = \left[R\right]^T\left[R\right]\left[K_{u/V}\right] \quad . \tag{11}$$

Each side is further multiplied by the inverse of the newly formed (R^TR) matrix

$$\left[R^TR\right]^{-1}\left[u/V\right]\left[R\right]^T = \left[R^TR\right]^{-1}\left[R^TR\right]\left[K_{u/V}\right] \quad . \tag{12}$$

If one recalls that the product of a matrix and its inverse gives the identity matrix, Eqn (12) becomes

$$\left[K_{u/V}\right] = \left[R^TR\right]^{-1}\left[u/V\right]\left[R\right]^T \quad . \tag{13}$$

By performing this series of matrix operations, one can easily find the $\left[K_{u/V}\right]$ matrix. To find the $\left[K_{w/V}\right]$, $\left[K_{C_o}\right]$, and $\left[K_{C_q}\right]$ matrices, one can follow the same procedure substituting w/V, C_o, and C_q into the right side of Eqn (13).

B. Assessment of Accuracy

Since the R matrix contains 15 columns, each of the K matrices will have 15 elements. When the K's have been found, they are used in Eqn (7) to find the desired output u/V, w/V, C_o and C_q. Having these K's thus constitutes a calibration. The validity of the calibration process can be shown by comparing the values of u/V, w/V, C_o, and C_q obtained initially using equations (1), (2), (5), and (6) (experimental values) with the values obtained using Eqn (7).

The accuracy as defined by the validity test of the calibration is dependent upon the physical properties or manufacturing anomalies as well as the various associated equipment of the probe; but, accuracy is also dependent on the way the calibration data samples are taken. If we assume that a systematic ϕ and θ schedule is followed in taking data (meaning that a certain number of constant ϕ and varying θ sweeps are made, taking data at regular intervals, fixed ϕ and θ), the number of data points or density of data points will be greatest near the $\theta = 0$ position. Although the calibration procedure itself is insensitive to the way in which the data are sampled, greater accuracy is afforded in the region of high density. Like any curve fitting routine, a more exact fit is provided in the region where most of the data lie. If constant accuracy over the entire range of data points is necessary, some measure must be taken to insure that the density of data points is everywhere the same.

An overall idea of the accuracy can be obtained by computing the standard deviations associated with the four desired outputs, by comparing the experimental values to those calculated using Eqn (7) by

$$Q_A = \left(\frac{\sum (A_e - A_c)^2}{n} \right)^{\frac{1}{2}}$$

where A = w/V, u/V, C_o and C_q in turn, n the number of data points being compared, and the e and c subscripts refer to experimental and calculated, respectively. Assuming the errors are normally distributed, one finds a 95% probability that the actual value will be within 1.96% of that calculated from the curve fit.

It should further be noted that the values of K depend directly upon C_a and C_b, which are pressure coefficients and, as such, are dependent upon Mach number; therefore, this calibration process is limited to incompressible flow.

III. Experimental Section

A. Apparatus

The experiment was conducted in the 2 by 3 foot subsonic wind tunnel at the United States Air Force Academy. A selected five-hole probe (Ref. 2) was mounted on a variable pitch string mount which allowed the probe a $\pm 30°$ range of movement in θ. This movement was controlled electronically through a DEC Laboratory peripheral system-11 (LPS-11), in coordination with a DEC PDP 11/45 Data Acquisition System. Changes in ϕ were accomplished manually. Pressures P_1 - P_4 were taken using four Barocel pressure transducers and P_5 was taken using a Statham transducer.

The five-hole probe had a diameter of 0.125 in. with each of the five tubes having an inside diameter of 0.020 in. (see Figure 3). The probe tip had a conical half-angle of 35°.

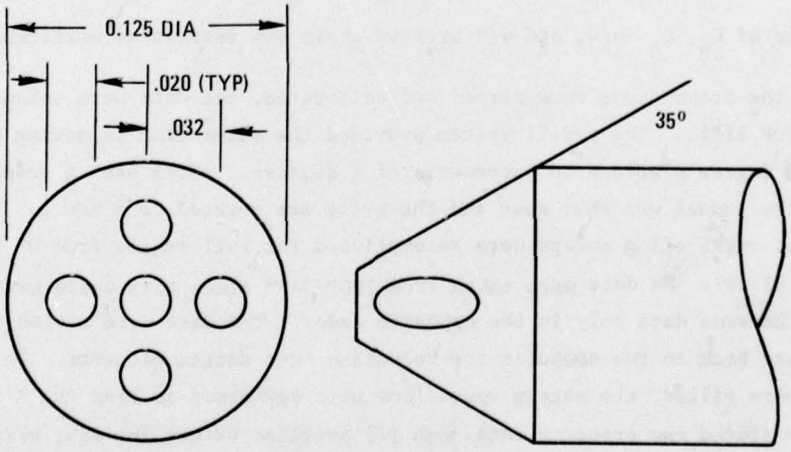

Figure 3. Probe Dimensions

B. Procedure

The procedure conveniently separates into initial calibration, and data acquisition and reduction.

1. Initial Calibration

The probe was carefully leveled in the wind tunnel by viewing it head-on from the stilling chamber through a surveyor's transit and a five-power magnifying glass located about one foot in front of the probe. The resulting image nearly filled the reticle and the probe was rotated until the bottom edges of the three holes across the horizontal coincided with the horizontal line on the reticle. This established the position for $\phi = 0$ and $\theta = 0$.

Keeping the probe clean in the wind tunnel environment was quite troublesome. Touching the end of the probe tended to deposit flakes of skin in and around the pressure ports. Reverse air flow through the tubes was sometimes effective in removing debris. At other times, small drill bits had to be used to mechanically remove the debris. We have found it practical to keep close-fitting dust covers on the probes when they were not in use.

2. Data Acquisition and Reduction

Just before data were taken, the static voltage was read from each pressure transducer for a "zeroing factor." The transducers were then calibrated against oil manometers. For this calibration, each data point taken consisted of twelve measurements: θ, P_1, P_2, P_3, P_4, P_5, P_0, P_∞, ϕ, free stream velocity, temperature, and barometric pressure. Although free stream velocity, temperature, and barometric pressure were never used in the data reduction, they were included as a part of each data point for classification purposes. Each data point (consisting of these twelve measurements) could therefore be reduced into C_a, C_b, C_o, C_q, u/V, and w/V using Eqn (1) through (6). The calculations of C_a and C_b created the R matrix while the calculations of C_o, C_q, u/V, and w/V created their own respective matrices.

After the transducers were zeroed and calibrated, the data were taken and stored using the PDP 11/45. The LPS-11 system provided the automation in moving the probe through $\pm$28 degree θ sweeps in increments of 4 degrees. After each θ sweep was complete, the tunnel was shut down and the probe was rotated to a new ϕ. This procedure was followed until all θ sweeps were accomplished for roll angles from 0° to 165° in increments of 15°. No data were taken from 180°-345° since this would have generated the same data only in the opposite order. The data were stored on a disk and were then read back to the computer for reduction into matrix elements. Once all matrices were filled, the matrix operations were performed to find the K's. Given the K's and the stored raw pressure data, Eqn (7) provided values for u/V, w/V, C_o, and C_q.

IV. Discussion

A. Flow Angles

Figure 4 provides a comparison between the actual and predicted (using the polynomials) values of u/V and w/V. An error band is represented by the difference in the two values. By examining this figure, one finds that the fit is most accurate near the origin (this corresponds to $\alpha = 0$). This is not surprising since, as noted earlier, data sample density was greater near the origin thus forcing greater accuracy in that area. The figure also shows that the actual values and the predicted values differ in an unpredictable way, that is, the position of the cross with respect to the dot for any particular data point differs in relative position from one data point to another. Figure 4 also shows that error tends to be least for positive values of u/V. Since no more data were taken in these quadrants than in the others, probe geometry inaccuracies are probably responsible.

Figure 5 is a u/V versus w/V plot showing constant C_a and C_b lines. Generally, these constant C_a and C_b lines tend to be vertical and horizontal. In the case of the constant C_a lines, the relative verticalness, especially for small angles, shows that C_a is relatively independent of v/V. Similarly, the relative levelness of the constant C_b lines, especially for small angles, shows that C_b is relatively independent of w/V. As the angles get larger (moving to the outside edges of the plot), C_a becomes more dependent on u/V and C_b becomes more dependent on w/V. An interesting peculiarity of this plot is the $C_b = -.5$ contour. The primary reason this contour line has such an odd shape is that most of the contour falls outside of the curve fit range.

B. Total and Dynamic Pressures

Constant contours of C_o plotted against C_a and C_b are shown in Figure 6. The contours are drawn using Eqn (7). According to the definition of C_o, these contours represent the difference between the total pressures measured by the tunnel and by the pressure port P_5. The plot shows that, for small angles, P_5 acts as another tunnel total pressure probe. The larger the angles, the larger the difference between P_o and P_5. The points labeled throughout the plot are experimental values of C_o at that specific C_a and C_b position. The position of these points with respect to the constant C_b contours provides another measure of the accuracy of the curve fit procedure. These contours are not perfectly circular, with equal C_a and C_b radii, which is another indication of slight probe asymmetry. In Figure 7 constant C_q contours are plotted against C_a and C_b.

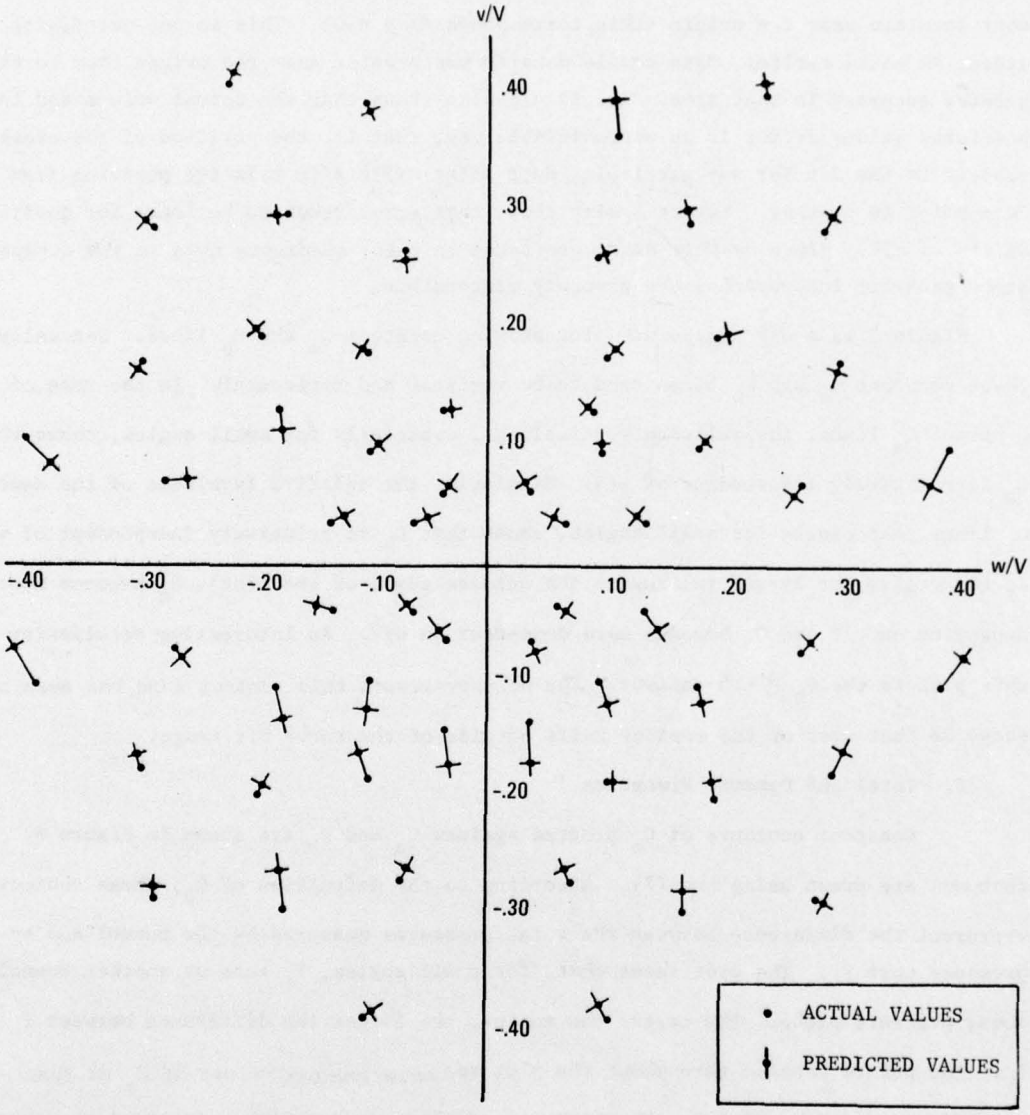

Figure 4. Comparison Between Actual and Predicted Values of u/V and w/V

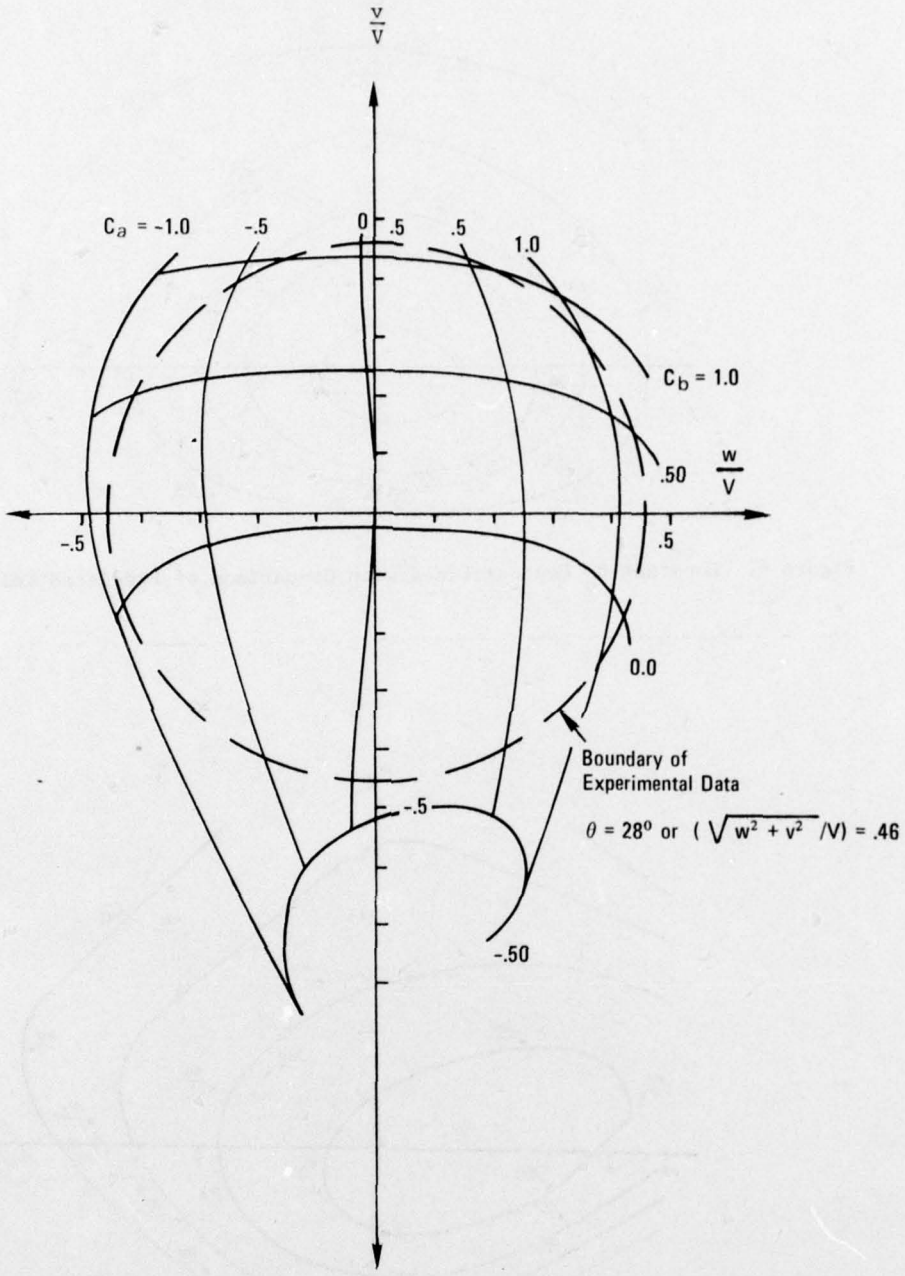

Figure 5. Constant C_a and C_b Contour Lines

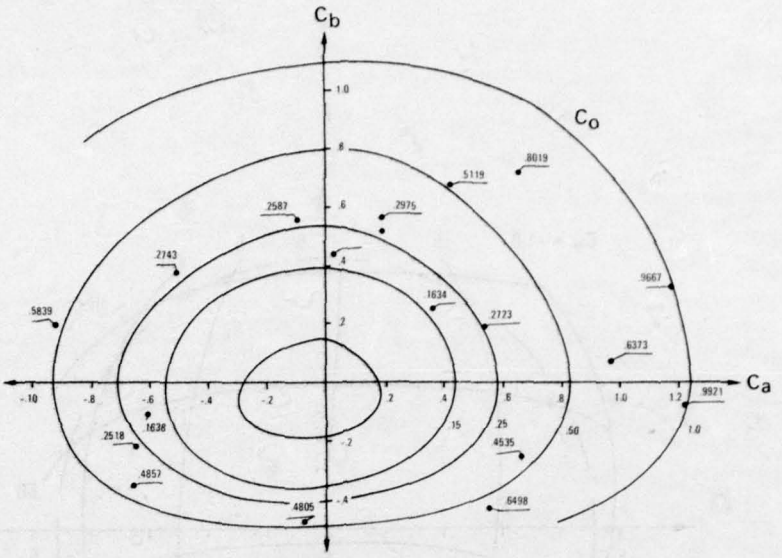

Figure 6. Constant C_o Contour Lines with Comparison of Predicted Values of C_o

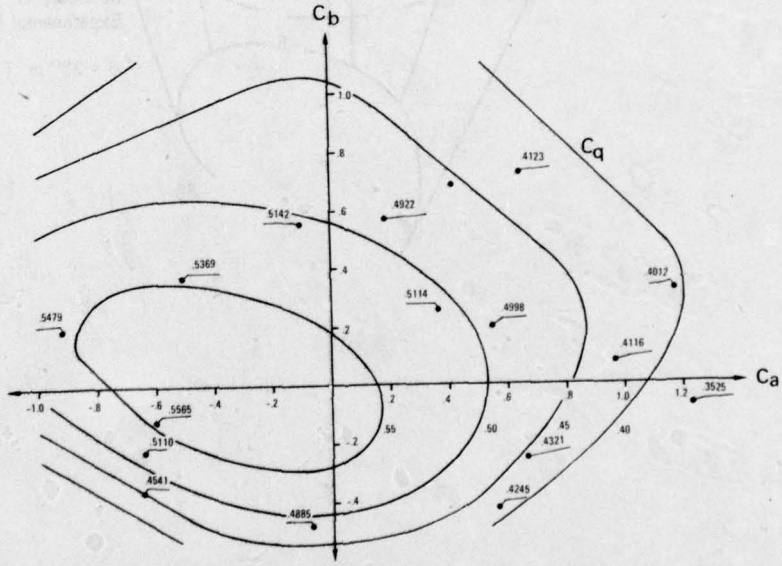

Figure 7. Constant C_q Contour Lines with Comparison of Predicted Values of C_q

Again, these contours were made using Eqn (7) while the individual points on the plot are experimental values. Cq is a ratio of the dynamic pressures measured by the probe to the total minus static pressure of the tunnel. This ratio decreases as the angles increase because the quantity $P_5 - \frac{1}{4}P_\Sigma$ decreases while $P_0 - P_\infty$ remains constant. More specifically, as the relative probe angle increases, P_5 decreases significantly and P_Σ remains relatively constant. The flat portions of the outer contours provide the major motivation for use of a fourth-order equation in curve fitting. As in the previous figure, an indication of the accuracy of the curve fit is the position of the theoretical values with respect to those obtained by Eqn (7).

C. Accuracy

Table 1 describes the average accuracy achieved over the full data set of all four parameters.

Table 1
PARAMETER ACCURACY

Variable	$1.96\ \sigma$
C_ϕ	0.049
C_q	0.019
u/V	1.14°
w/V	0.40°

With 95% certainty, angles are indicated to about the nearest degree and total pressure is indicated to about 5% of $P_5 - \frac{1}{4}P_\Sigma$ or 2.5% of the dynamic pressure. The dynamic pressure is indicated to about 2% of $P_5 - \frac{1}{4}P_\Sigma$ or 1% of the dynamic pressure.

References

1. Breyer, D. W. and R. C. Pankhurst. Pressure Probe Methods for Determining Wind Speed and Direction. London: Her Majesty's Stationery Office, National Physical Laboratory, 1971.

2. Gallington, R. W. and C. F. Hollenbaugh. "A Fast Method for Accurate Manufacture of Small Five-Hole Probes." Aeronautics Digest - Spring 1979, USAFA-TR-79-7, USAF Academy, Colorado, July 1979.

3. Neter, J. and W. Wasserman. Applied Linear Statistical Models. Homewood, IL: Richard D. Irwin, Inc., 1974.

A FAST METHOD FOR ACCURATE MANUFACTURE OF SMALL FIVE-HOLE PROBES

Roger W. Gallington* and Claude F. Hollenbaugh**

Abstract

A mechanical design and minimum effort manufacturing procedure is presented which results in close conformance to the desired nose shape for small conical five-hole probes. The probe consists of five tubes fitted inside a barrel with the interstitial positions filled with properly sized rods. The whole assembly is soldered together and ground to a conical shape.

I. Introduction

Small five-hole probes of various nose shapes have been used for many years. By proper calibration Breyer & Pankhurst (Ref. 1) point out that one can extract total pressure, static pressure, and all three components of velocity using the five pressures obtainable from these probes. The details of such a calibration are given in a companion paper in this issue of the Aeronautics Digest (Ref. 2).

As is the case for all flow-measuring instruments there is a strong motivation for miniaturization, since the goal is that the probe be used in flows of significantly larger scale than the probe itself. There are two important limits to miniaturization of five-hole probes. First the flow areas of the pressure ports and the connecting tubes can eventually become small enough to seriously limit the time response of the probe even when connected to the best available transducers. Secondly, with extremely small sizes it is very difficult to maintain dimensional control during manufacture.

It is the purpose of this paper to describe a probe design and manufacturing procedure which we believe combine to nearly approach the practical lower limit of probe size.

II. Design

Apparently the five-hole probe with the largest ratio of individual tube diameter to overall outside diameter is the one described by Breyer & Pankhurst (Ref. 1) and Dudinski and Krause(Ref. 3). This design is illustrated in Figure 1. In passing it is interesting to note that the five tubes can actually be packaged inside a slightly smaller outside diameter by using the configuration of Figure 2. The tube that eventually becomes the nose, however, must somehow get to the middle of the tube bundle, this requiring an increase in the overall diameter from that of Figure 2 to that of Figure 1.

---

*Lt Col, USAF, Associate Professor of Aeronautics, DFAN

**Engineering Technician, DFAN

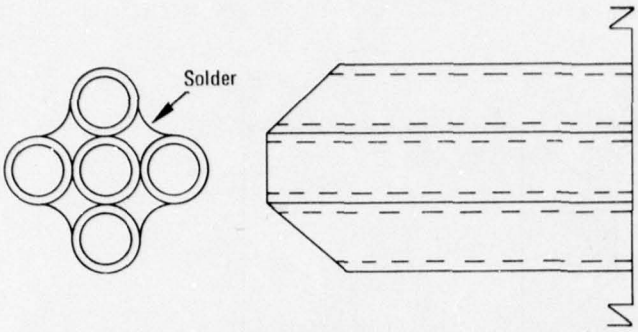

Figure 1. Five-Hole Probe Assembled From Tubes

Figure 2. Five Tubes in the Smallest Circumscribed Circle

Accurate manufacture of the probe design of Figure 1 is hindered by three major difficulties: (1) it is very difficult to hold the tubing parallel, in contact, and in perfect azimuthal position for soldering; (2) there is no guarantee that the size of the four solder fillets will be equal or nearly equal; (3) assuring equal chamfer on the four side tubes requires very careful work under a high power magnifier (Ref. 1).

An operational disadvantage of the probe design of Figure 1 is that there is no convenient surface for alignment as on a cylindrical barreled probe. The outside edges of the outer tubes could, in principle be used; however, they occur only every 90 degrees. Also, an alignment procedure would require maintaining perfect azimuthal position of the outer tubes for some distance down the probe as well as at the tip.

By automatically holding the parts in correct alignment, the probe geometry shown in Figure 3 overcomes all the aforementioned problems in probe design and construction with a penalty of only a ten percent increase in outer diameter. If one manufactures a probe of the Figure 3 design, the internal diameter of the barrel must be exactly three times the outer diameter of the tubes, and the diameter of the fillers must be 0.6796 times the outer diameter of the tubes as is shown by the law of cosines in Figure 4. Since drill bits can be bought in finely graduated small sizes, we used them for fillers. We used cone half angles of 30° to 45°.

III. Construction

The five tubes were initially clamped in a jig as shown in Figure 5. A special jig was made with a groove sized to hold the five tubes in approximately the correct position (groove size varied for each specific tube size design). Perfect positioning by this method is, of course, impossible; the five tubes are tack silver-soldered together at the gap in the jig only to prevent them from falling into the configuration of Figure 2.

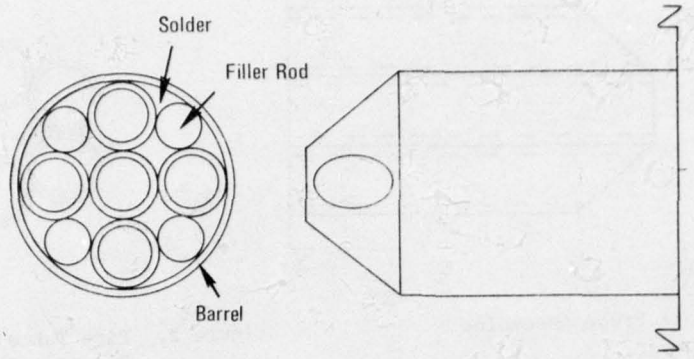

Figure 3. Convenient Probe Design

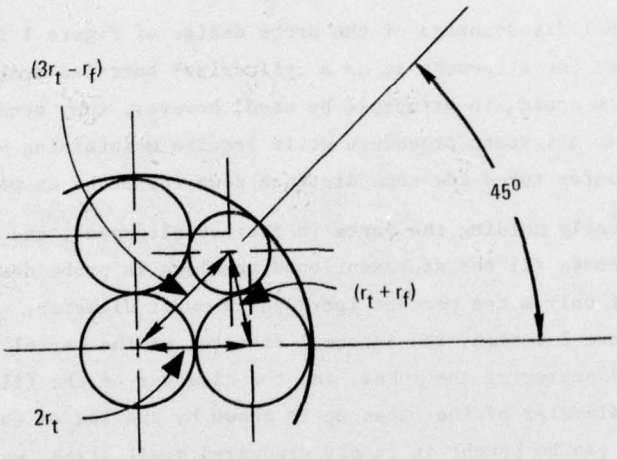

$$(r_t + r_f)^2 = (2r_t)^2 + (3r_t - r_f)^2 - 2\,(2r_t)\,(3r_t - r_f)\,\text{Cos}\,45^0$$

$$\frac{r_f}{r_t} = \frac{6 - 3\sqrt{2}}{4 - \sqrt{2}} = .6796$$

Figure 4. Filler Rod Size

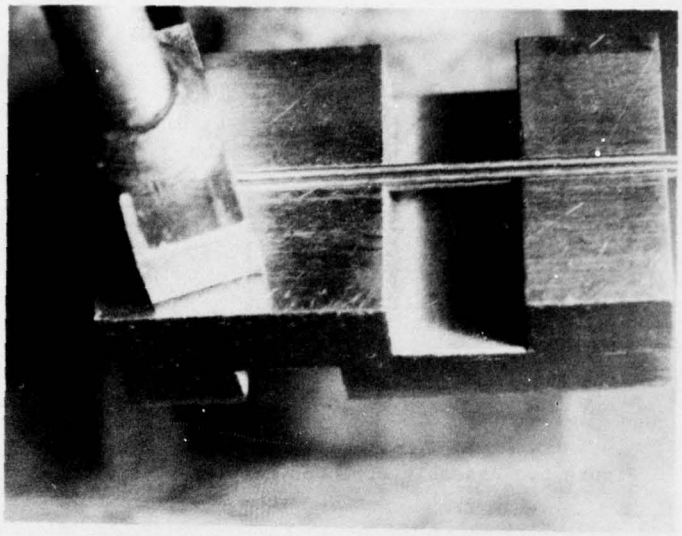

Figure 5. Jig for Holding Tubes for Soldering

The tack-soldered tubes are then inserted part way into the barrel. Drill bits (or other hard spacers) are then inserted into the four voids to accurately create and maintain the required geometry. The entire bundle is slid into the barrel allowing about 3/16 inch of the shanks to remain outside the barrel as shown in Figure 6. The whole assembly is then soldered together. Careful cleaning and correct use of flux are required to assure that the voids are filled. After soldering, the tubes are cut off even with the drill bit ends, having been left long until now to prevent filling with solder. The desired nose shape is then formed on a lathe using a tool-post grinder. Finally the tubes are cleaned or reamed with a proper diameter drill.

The probe is inspected, under 30-power magnification, for imperfections and cleanliness. If imperfections are found the grinding and cleaning operations can be repeated. Care must be taken to avoid touching the probe tip after cleaning as the sharp edges of the tubes tend to scrape off small bits of skin which plug the ports.

The probe shown in Figure 7 was made by this method. Its outer diameter is 0.109 inches or 2.7 mm. Limited only by available tubing sizes, probes as small as 1.0 mm diameter can be made using this method.

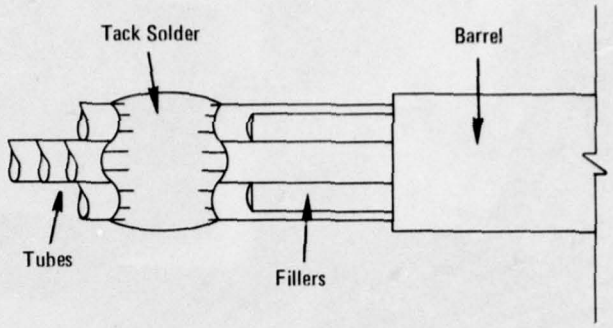

Figure 6. Assembly of Tubes, Fillers, and Barrel

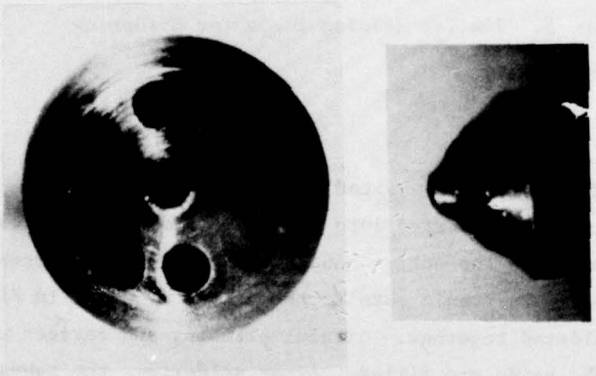

	ID	OD
TUBES	0.020	0.028
BARREL	0.084	0.109
FILLERS		0.019

Figure 7. Example Probe (Dimensions in Inches)

IV. Conclusions

A miniature five-hole probe design consisting of five tubes fitted inside a barrel with the interstitial positions filled with properly sized rods, the whole assembly being soldered together and ground to a conical shape, is much easier and faster to construct accurately than previous designs. The design described here requires about ten percent larger diameter for the same flow area in the tubes compared to previous designs.

The smallest probe we have constructed to date has an outside diameter of 2.7 mm; however, the technique can probably be applied to probes as small as 1 mm outer diameter.

References

1. Breyer, D. W. and R. C. Pankhurst. *Pressure Probe Methods for Determining Wind Speed and Direction*. London: Her Majesty's Stationery Office, National Physical Laboratory, 1971.

2. Barker, K., R. W. Gallington, and S. Minster. "Calibration of Five-Hole Probes for On-Line Data Reduction." Aeronautics Digest - Spring 1979, USAFA-TR-79-7, USAF Academy, Colorado, July 1979.

3. Dudinski, T. J. and L. N. Krause. Flow Direction Measurements with Fixed-Position Probes in Subsonic Flow Over a Range of Reynolds Numbers. NASA TMX-1904, N69 40059, 1969.

A LASER DOPPLER VELOCIMETER SYSTEM TO INVESTIGATE UNSTEADY FLOW SEPARATION

George W. Sparks, Jr.,* John P. Retelle, Jr.,**
John E. Keesee,*** Michael S. Francis,*** and James M. Lind***

Abstract

The adaptation of multi-component Laser Doppler Velocimetry (LDV) techniques for the measurement of flow velocity in regions of unsteady separation is discussed. A positionable, two-color backscatter LDV system was employed in conjunction with a disk-based minicomputer to assess unsteady flow separation generated on an airfoil surface behind a controlled, oscillating, fence-type spoiler in a subsonic wind tunnel environment. The solutions to significant optical noise problems created by limited optical access and the nature of the experimental configuration are described. The acquisition of discontinuous data signals provided by the LDV counters using an asynchronous sampling technique is also addressed. The determination of time-varying mean values of the velocity components has been effected through the adaptation of a phase-locked ensemble-averaging scheme originally developed for use with continuous (analog) signals. Interactive computer control of the positioning of the measurement volume using a two-dimensional traversing mechanism is also described. The resultant measurements using this system are compared with those obtained by a hot-wire anemometer in an unsteady, non-reversing flow environment compatible to both techniques.

I. Introduction

The Laser Doppler Velocimeter (LDV) has demonstrated its capabilities as a versatile, non-intrusive flow measurement tool for assessing the detailed behavior of complex flow fields. Despite its current popularity and widespread application, the potential of the LDV has not been fully exploited in flow environments exhibiting unsteady mean motion and separation. The ensuing discussion is directed toward the adaptation and implementation of multi-component LDV techniques to flows of this nature.

While the LDV concept can be traced to the mid-1960's (Ref. 1), its application to a wide range of fluid mechanics problems has occurred only recently. The advantages of the technique over other flow velocity measurement schemes has been well documented (Ref. 2). As with all laboratory tools, these advantages are balanced, to some extent, by a few negative factors which can limit the usefulness of the method in some cases. Among the more commonly recognized shortcomings are optical alignment problems, accuracy dependence on particle scattering centers of the proper size, and high initial system cost. A serious problem encountered with the backscatter system described in the next section was that of optical noise generated by laser beam reflections as a result of the limited optical access afforded by the experimental configuration.

---

*Captain, USAF, Assistant Professor of Aeronautics, DFAN
**Major, USAF, Associate Professor of Aeronautics, DFAN
***Captain, Frank J. Seiler Research Laboratory (AFSC)

Perhaps the most detrimental single characteristic which limits application of the LDV concept to complex unsteady flows is the discontinuous nature of the data signal. Sometimes referred to as signal "drop-out," this inability of the LDV to generate continuous signals which characterize the velocity field represents a potentially serious drawback in extracting "ensemble averages" which are representative of the unsteady mean motion, yet capable of excluding the random (noise and turbulence) portion of the flow variable. Methods developed previously to obtain this time-varying mean behavior from data available from common analog instruments (e.g., pressure transducers, hot-wire anemometers) have relied on synchronous sampling capabilities common to today's high speed data acquisition systems. The development of a sampling algorithm compatible with the discontinuous nature of the LDV signal while retaining the desirable features of synchronous sampling methods is required for the assessment of these unsteady mean flow characteristics.

The sampling and phase-locked ensemble averaging scheme described below was developed for use with a wind tunnel experiment where the harmonic unsteadiness of the flow field was controlled and where more classical flow measurement techniques had limited application. The determination of the unsteady mean velocity field in this manner, for example, is a prerequisite to the evaluation of the time-varying mean vorticity field using the contour integration technique previously suggested by Keesee, et al. (Ref. 3). The discussion of this algorithm follows a brief description of the nature of the experiment and a discussion of the LDV system and related experimental components employed in this case.

II. Description of the Experiment

The application of LDV techniques to complex unsteady flows is illustrated by an experiment in which controlled unsteady flow separation is generated behind an oscillating fence-type spoiler located on one surface of an airfoil immersed in a subsonic freestream. A sketch of the airfoil, spoiler and resulting generalized flow field is provided in Figure 1. With the capability to adjust spoiler geometry parameters (stroke and mean height), frequency characteristics, and mean flow Reynolds number, this configuration provided for control of the size of the separated region while fixing the separation point with respect to the freestream coordinate direction. The assessment of velocities in local regions of energetic, intermittently reversing flow near the airfoil surface required the application of LDV technology as the only means of obtaining a quantitative description of the velocity field.

The experiment employed a NACA 0012 airfoil model with the spoiler protruding from one surface at the mid-chord location. The apparatus was installed in the USAF Academy 0.61 meter (2 foot) x 0.91 meter (3 foot) subsonic wind tunnel with the model spanning the shorter dimension (vertically). The spoiler oscillation mechanism used a DC motor drive system to generate sinusoidal oscillations which can be characterized by the following equation:

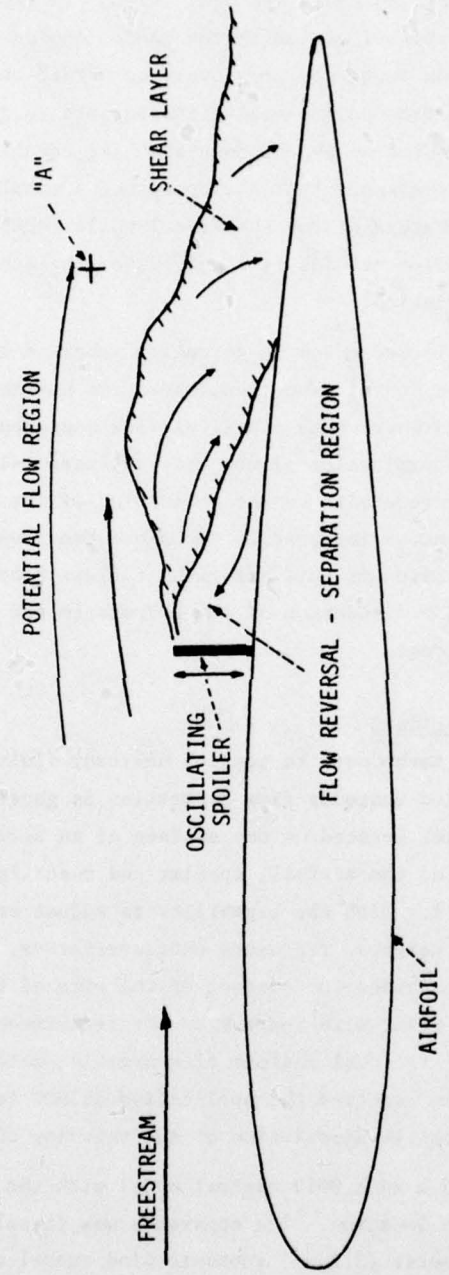

Figure 1. Generalized Flow Field Structure During the Spoiler Upstroke

$$h_s(t) = \frac{h_{s_{max}}}{2} (1 - \cos \omega t) \qquad (1)$$

where $h_s(t)$ is the instantaneous spoiler height (above the surface); $h_{s_{max}}$ is the maximum extension of the spoiler.

The maximum fractional perturbation to the flow, therefore, can be expressed as a ratio of the spoiler height to the wing semi-chord and is equal to a value of 0.1 in this case. Spoiler oscillation frequencies could be varied between 0 and 20 Hz to within 0.01 Hz resolution. The drive apparatus was physically located beneath the wind tunnel test section.

An opto-electronic triggering device was attached to the spoiler oscillation mechanism to provide a pulsed output which corresponded to a prescribed (usually minimum) value of the spoiler height. The signal was employed as a triggering source to provide a phase lock on the initiation of data sampling.

Freestream velocities for these experiments were maintained in the subsonic regime and ranged from approximately 15 m/sec (50 ft/sec) to 41 m/sec (135 ft/sec).

An assessment of the velocity and vorticity fields in the outer shear layer region adjacent to the spoiler has previously been made by Francis, et al. (Ref. 4) using more conventional hot-film anemometry techniques. These experiments involved the use of an "X"-geometry hot-film probe oriented to provide two orthogonal components of velocity from which other flow characteristics such as vorticity were inferred. The hot-film probe was supported on a multi-dimensional traversing mechanism capable of evaluating flow characteristics over a large portion of the tunnel test section. The measurements obtained with this system were employed to form the basis of a systematic comparison between the hot-film and LDV methods. Previous algorithms for hot-film measurements had been developed to evaluate the time varying mean flow velocity field using synchronous sampling techniques. The limitations of hot-film methods in regions of intermittent flow reversal near the airfoil surface are, however, immediately apparent, necessitating the use of a measurement tool capable of satisfying the demanding measurement requirements of this region.

The availability of a disk-based minicomputer data acquisition system (DEC PDP 11/45) greatly simplified the problems of data acquisition and storage from all sources. The system was configured with a laboratory peripheral system (DEC LPS-11) which included a high speed real time clock, Schmitt triggers, relays, and other hardware interface subsystems designed for application to general laboratory problems possessing a capability for either analog or digital external inputs. A functional schematic of the overall instrumentation system employed in the experiment is provided in Figure 2. The figure depicts both the hot-wire anemometry system and the LDV.

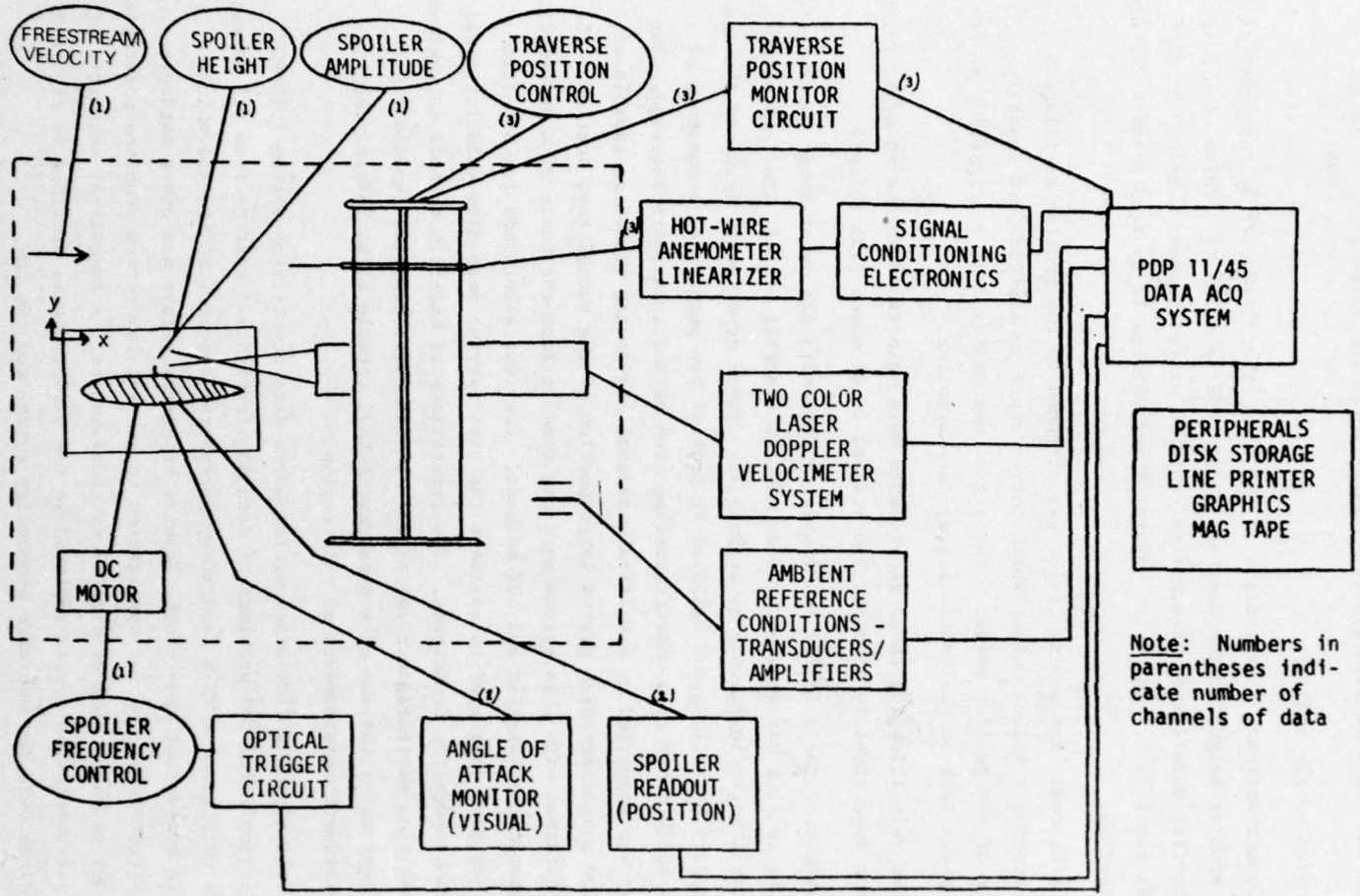

Figure 2. Functional Schematic of Experimental Apparatus

III. Laser Doppler Velocimeter (LDV) System

The design of the LDV system employed in conjunction with the experiment described above was constrained not only by the nature of the flow under investigation but also by the configuration of the experimental facility and apparatus. Optical access, for example, was restricted to a single window in the ceiling of the wind tunnel test section. For this reason, the dual beam backscatter mode (Ref. 5) was determined to be the only logical choice for the LDV system since both the incident beams and scattered signals were required to pass through the same optical port. In this mode, monochromatic laser light is divided into two parallel beams of equal power and focused to a point within the flow, called the measurement volume. Particles passing through this region scatter light back through the transmitting/collecting lens and into a photomultiplier tube, providing an output frequency proportional to the particle velocity. An additional advantage of the dual beam backscatter concept was that it allowed both the transmitting and collecting optics to be located on the same support structure as the laser, thereby requiring only a single drive system. This arrangement also eliminated the need for a slaved optics detector unit that would have been required for a forward scatter optical system.

The dual beam backscatter system described thus far fails to discriminate particle direction since the measured Doppler frequency is proportional to an inner product of the velocity vector with itself. That is, two particles with equal speeds but traveling in opposite directions could produce identical output frequencies. This ambiguity was removed by frequency shifting one of the two dual beams with an acousto-optic Bragg cell, causing the interference fringes in the measurement volume to move. A particle in this region at zero velocity would, therefore, emit a Doppler frequency equal to the frequency shift imposed by the Bragg cell, while a particle with a negative velocity would provide a Doppler frequency lower than that of the frequency shift. Two Bragg cells, one for each of the two beams, were incorporated into the optical arrangement employed in the present case. Figure 3 shows the optical system designed to meet the constraints of the wind tunnel environment while satisfying the measurement requirements of the unsteady flow field. Results discussed below were obtained using only particles naturally occurring within the flow which acted as scattering centers. This natural seeding provided data rates of 5-50 per second depending upon the flow velocity and the measurement position with respect to the airfoil model. Artificial seeding is currently being investigated to provide higher data rates, especially when attempting measurements in reversed regions near the surface.

An argon-ion laser which provided strong lasing lines at 4880 Å (blue) and 5145 Å (green) was employed to permit simultaneous measurement of two velocity components. The integrated optics assembly spatially separated the blue and green beams, frequency shifted them, and then focused the four resulting beams to form a measurement volume at approximately the midspan position in the test section. The beams entered the test

section through an AR-coated, optical-quality glass window. The scattered light from particles passing through the measurement volume was received by a collection optics/photomultiplier system housed in the integrated optics assembly.

Two counter-type signal processing units (TSI model 1990) were used to analyze the photomultiplier signals and provided both analog and digital outputs representing the time (or frequency) for a particle to cross a specified number of fringes within the probe volume. The counters also employed an operator-selected data validation scheme which provided for rejection of spurious signals, thus reducing the data error caused by noise. Velocity bias caused by large particles could be reduced by a variable attenuator which rejected large amplitude signals. The counter processors also contained digital displays to monitor the analog output and data rate in real time.

The drive system and optical support structure (Figure 3) consisted of a dual-axis optical bench truss for orthogonal translation of the probe volume throughout the flow region. This design was mechanically quite stable and could be repositioned to within 0.025mm (0.001 inch). An interactive, computer-based system controlled the two DC motor drive units and thus positioned the measurement volume at specified locations within the flow.

IV. Data Sampling and Averaging Scheme

Perhaps the most difficult task encountered in applying this system to the unsteady flow environment involved the correlation of randomly occurring data samples in a manner which could effectively describe the local time-varying velocity characteristics. The inability to synchronously sample the data "signal" represented a major obstacle in generating a phase-locked ensemble averaging scheme comparable to those employed with continuous data signals. The algorithm described in the flow charts in Figure 4 was developed in an attempt to reconcile the best features of the synchronous data sampling concept with the irregular digital signals which would be obtained in a lightly seeded flow using an LDV.

To execute the algorithm, one must obtain a precise determination of the actual sampling time synchronized to the driving oscillation of the experiment. For this reason, an external clock was used which is controlled through hardware by a periodic event associated with the motion in the flow. In the experiment described above, a pulsed output initialized the clock at a prescribed value of the spoiler height.

After the program has been initialized and the necessary variables and arrays defined, the sampling subroutine is initiated. The LDV counter processor provides a "data ready" pulse to the computer when a valid data word is latched into the processor's output register. The data word, which represents the time for a particle to cross a specified number of fringes in the measurement volume, is then read into the computer input buffer. Almost simultaneously, the system clock is read, providing a

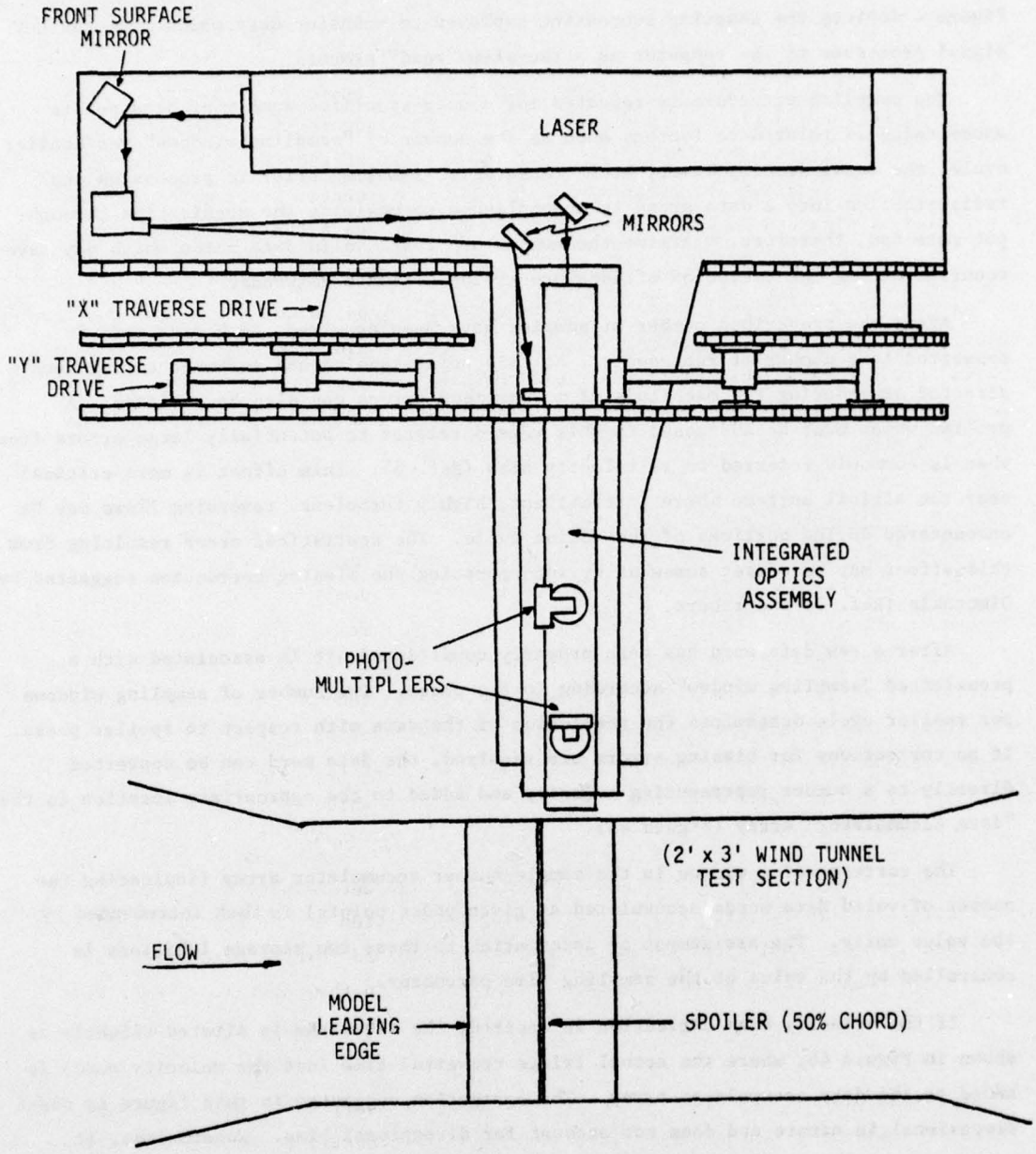

Figure 3. LDV Optical System and Wind Tunnel Test Section, Side View

measurement of the spoiler position when that particular data word occurs. This information is read in the form of an integer word representative of the fractional period of motion defined by the phase-locked clock. It becomes apparent that increased system clock resolution results directly in increased phase-locked measurement accuracy. Figure 4 depicts the sampling subroutine employed to transfer data words from the LDV signal processor to the computer as a two-step "read" process.

The sampling procedure is repeated for a user-specified number of data points whose value is related to factors such as the number of "sampling windows" per spoiler cycle, the local seeding level, etc. Consecutive sampling prior to processing and redistribution into a data array is accomplished to maximize the acquisition throughput rate and, therefore, minimize the number of "lost" valid data words which may have occurred during the execution of data processing software commands.

After the prescribed number of samples have been acquired, each data word is converted to a number it represents. At this point, additional software corrections directed at reducing the magnitude of measurement errors can also be utilized. A problem which must be addressed in this regard relates to potentially large errors from what is commonly referred to as velocity bias (Ref. 6). This effect is more critical near the airfoil surface where intermittent, highly turbulent, reversing flows may be encountered during portions of the motion cycle. The statistical error resulting from this effect may be offset somewhat by incorporating the biasing correction suggested by Dimotakis (Ref. 7) and others.

After a raw data word has been properly conditioned, it is associated with a preselected "sampling window" according to its phase. The number of sampling windows per spoiler cycle determines the resolution of the data with respect to spoiler phase. If no corrections for biasing errors are required, the data word can be converted directly to a number representing velocity and added to the appropriate location in the "data accumulator" array (Figure 4a).

The corresponding window in the sample-number accumulator array (indicating the number of valid data words accumulated at given phase points) is then incremented by the value unity. The assignment of information to these two storage locations is controlled by the value of the sampling time parameter.

If the velocity bias correction is desired, the algorithm is altered slightly as shown in Figure 4b, where the actual fringe traversal time (not the velocity word) is added to the data accumulator array. The correction suggested in this figure is one-dimensional in nature and does not account for directional bias. Nonetheless, it serves to illustrate the method and can be used to reduce the magnitude of the bias error. In both cases, with or without the bias correction, the appropriate location in the sample number accumulator array is incremented for a valid data word. In the case of the data that are uncorrected for velocity bias, averaging is accomplished by dividing the contents of the data accumulator array by the number of corresponding

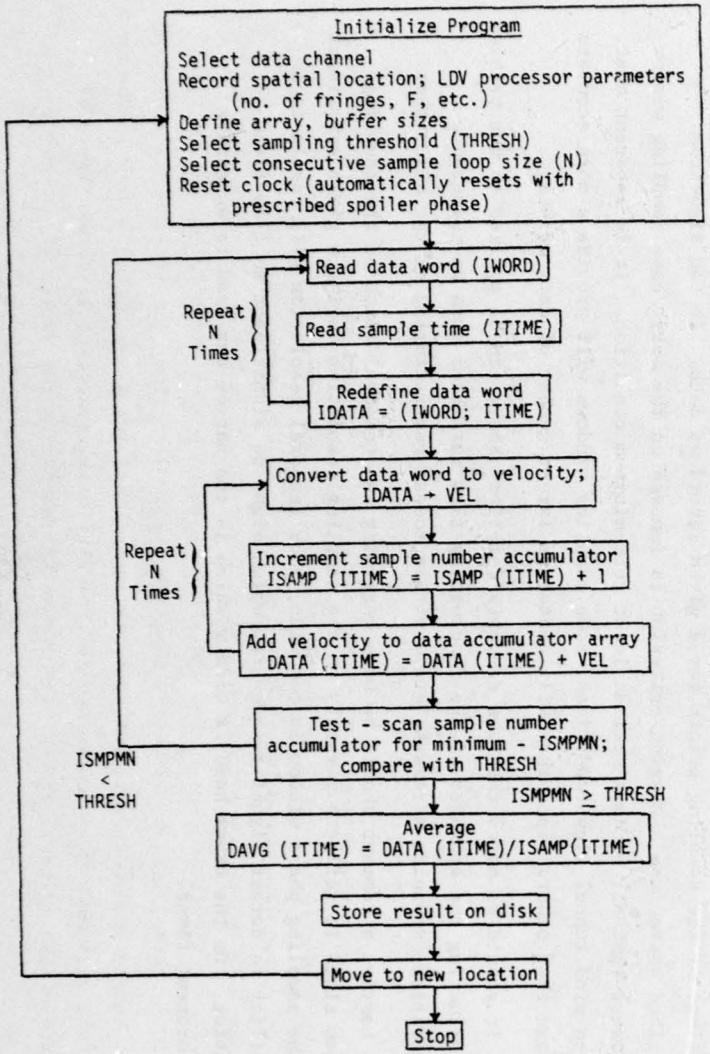

(a) Without Correction for Velocity Bias

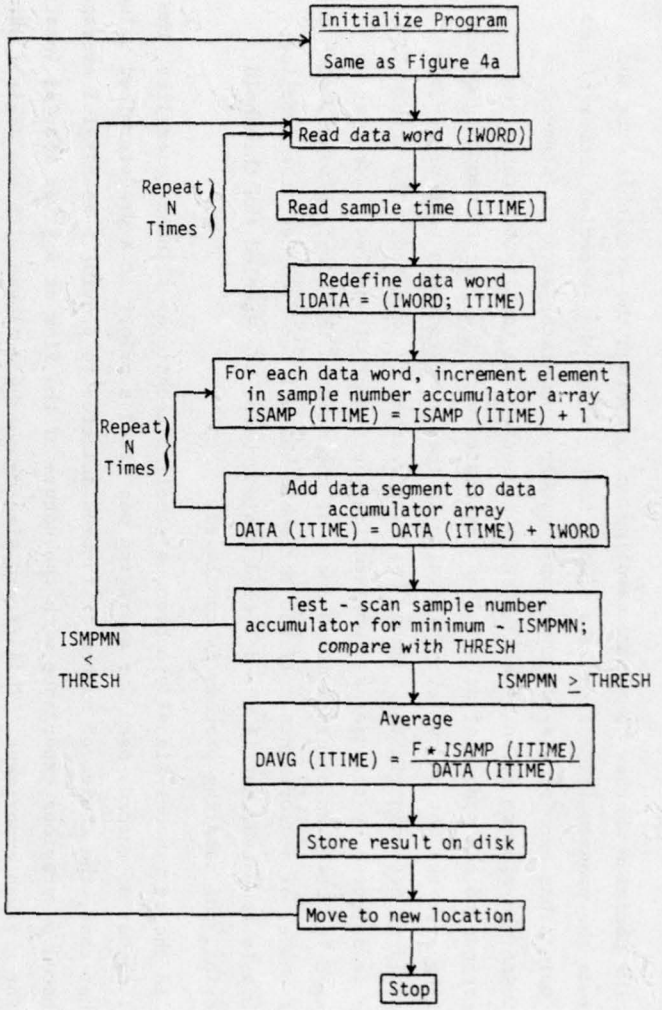

(b) One-dimensional Velocity Bias Correction Incorporated

Figure 4. LDV Sampling and Averaging Algorithm for Periodic Unsteady Flow

entries (for the same sampling window) in the sample number accumulator array. If the biasing correction has been made, the results of the sample number accumulator array are multiplied by the total number of fringes counted in all of the measurements (N). The resultant array is then divided by the corresponding time entries in the data accumulator array.

The decision whether to resume sampling or to average the available data and conclude the program is made using a simple test. After the specified number of new data points has been processed, the sample number accumulator array is scanned to determine the minimum value of all integers present. The resultant integer word corresponds to the number of data values associated with the "worst" sampling window existing over the motion cycle. This value is then compared to a user-prescribed threshold to determine if this number has been reached or exceeded. The threshold value is selected by the user as representing the number of samples which must be averaged to obtain an accurate measurement of the mean in the sampling window with the least number of measurements. If the threshold has not been reached, the sampling process is repeated, but if the detected minimum value has equaled the threshold criterion, the sampling process is concluded.

In the continuous signal/synchronous sampling techniques alluded to earlier, the total number of records used for averaging was fixed a priori at a predetermined value. In that case, the choice of number of records selected to provide a meaningful average was based on previous experience with the nature of the flow at a given spatial location and for a given experiment. This record size cannot be employed with the digital data signals available from the LDV due to the inability to accurately predict the temporal locations of the sampling points for a given record of data. In the algorithm described above, the averaging criterion is imposed on the worst-case sampling window to insure that all windows meet at least this minimum condition. It is apparent that, due to wind tunnel flow conditions, some sampling windows will provide a more accurate average than others since they will contain a larger number of data points.

It should be noted that the concepts described above can be applied to the problem of evaluating the averages of the fluctuating flow variables such as turbulence intensities, Reynolds stresses, etc., with a modest restructuring of the algorithms.

Lastly, a comment should be made regarding the temporal width of the sampling window since it reflects directly on the sampling resolution during a given experiment. If the sampling phase window is too wide, poor temporal resolution will result in an inability to detect signal frequencies which might be significant to flow field behavior. On the other hand, a window which is too narrow can lead to excessive measurement times.

V. Comparison of LDV and Hot-Film Results

To test the compatibility of the LDV and hot-film techniques with respect to the phase-locked ensemble average described above, measurements were conducted to generate a direct comparison of time-varying mean velocity characteristics at identical spatial locations. While the LDV was constructed specifically to assess flow field behavior near the airfoil surface where intermittent reversal and high turbulence levels are present, the measurements discussed below were conducted in a region where both methods were capable of providing accurate results. The data discussed below were obtained at a spatial point located 8.13 cm (3.2 inches) downstream of the spoiler (82 chord from the leading edge) and 4.16 cm (1.64 inches) above the local airfoil surface (point "A" in Figure 1). This point was situated in a region which experienced the passage of the turbulent outer shear layer during a portion of the motion cycle and which was characterized by locally laminar flow conditions during the remainder of the time.

The freestream velocity was maintained at a value of 21.3 m/sec (70 ft/sec), while the spoiler oscillated harmonically at a frequency of 13.37 Hz (equivalent to a reduced frequency based on the airfoil semi-chord of 0.5). The maximum spoiler height was fixed at 1.27 cm (0.5 inches) above the airfoil surface at midchord.

The primary advantage of obtaining a comparison in the potential flow region is the absence of turbulent fluctuations, which, therefore, should result in a reliable average with a comparatively small number of samples. The assessment of mean flow characteristics during the period of shear layer passage represented a greater challenge since the instantaneous level of turbulence directly influenced the number of records required for a reasonable average.

The data depicted in Figure 5 show a comparison of velocity component values in the freestream direction (blue beam). The hot-film anemometer results were obtained for a 25-record average with a sampling interval of 3 degrees of phase. A threshold criterion of 50 samples (worst case) was employed with the LDV requiring that particle velocities be evaluated after crossing 3 fringes. No correction for velocity bias was incorporated due to the nature of the flow (comparatively small fluctuations) at the sampling location. A sampling window of 3 degrees was used here also, yielding a cycle characterization of 120 data words. It should also be pointed out that the results depicted were obtained during two independent experimental "runs."

The qualitative agreement in the shapes of these curves is readily apparent. Phase information appears to be consistent between the two sets of data. The fluctuations which appear as "noise" in the LDV measurements can be attributed to any one of a number of factors including the need for a large number of samples. More samples are also required to properly correct for biases introduced by particles which are incapable of locally following the flow. The discrepancy in local values of the magnitude can, in part, be explained by the fact that both sets of measurements were conducted

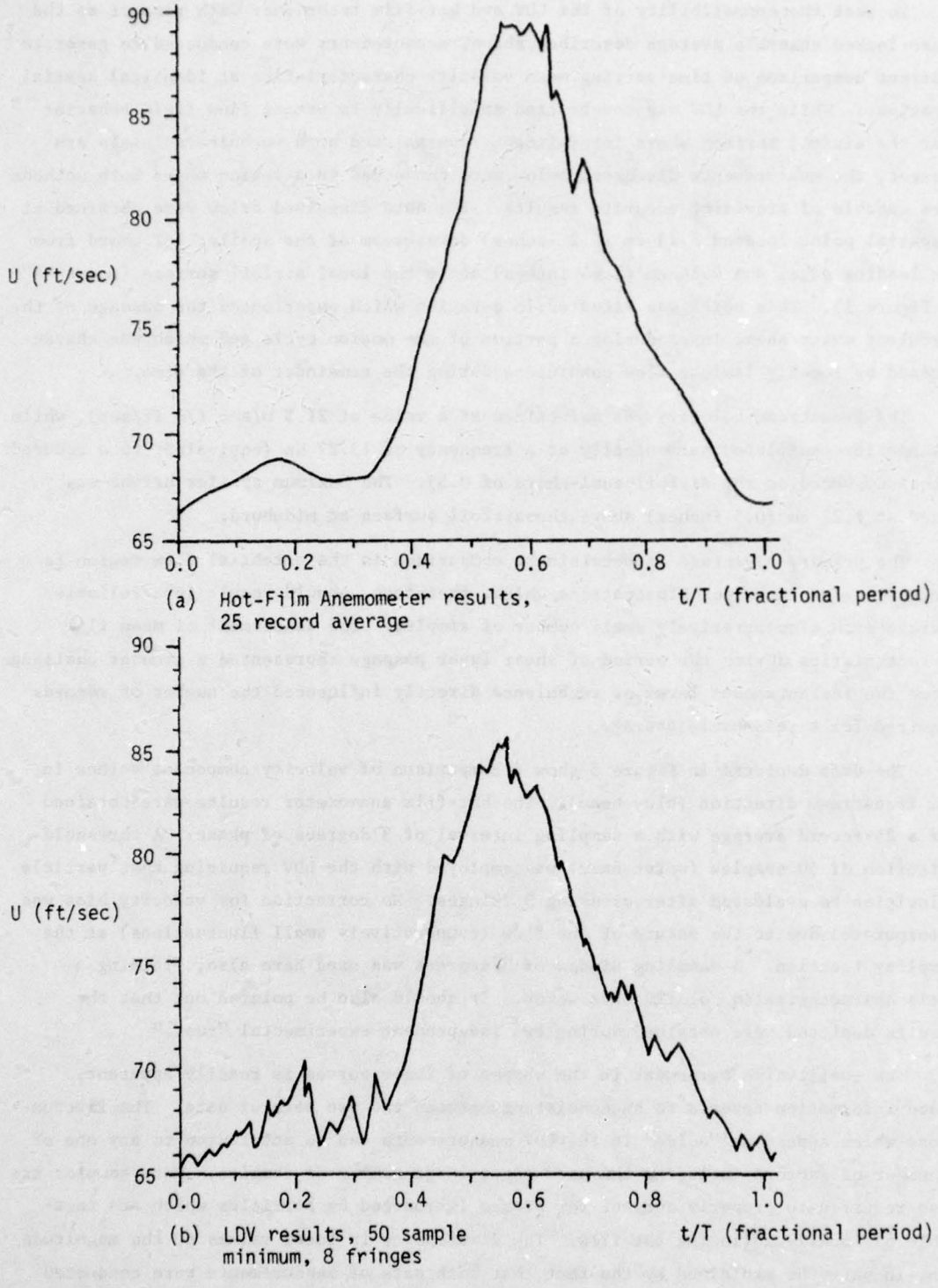

Figure 5. Comparison of Velocity Component Values in the Freestream Direction (Blue Beam)

independently. The width of the sampling window also contributes to the magnitude of this error-- the hot-wire results having been obtained from an essentially continuous (analog) signal average.

Figure 6 shows a similar comparison for the down-wash velocity component (green beam). Again, a 25-record average was employed with the hot-film anemometer, but the LDV signal processors were adjusted so that 16 fringes of traversal were required. Other experimental parameters were identical to those described above. A 2 MHz signal frequency shift was employed to provide for the identification of velocity values in both directions. Again, the agreement between the two results is apparent. In this case, however, the absence of random fluctuations in the final average indicates that the accuracy of the velocity average has been favorably affected by the fringe traversal criterion.

VI. Summary

The LDV system described in the preceding paragraphs has identified its potential as a useful tool in the investigation of unsteady flows involving periodic separation. The system employs a two-color argon-ion laser for simultaneous assessment of orthogonal flow velocity components operating in the backscatter mode. Frequency shifting devices (Bragg cells) are employed to provide a means of measuring reversed flow velocities in the interior of the separated region.

The potential accuracy of an algorithm developed to generate unsteady time-varying mean flow velocity components using discontinuous LDV data signals has been qualitatively demonstrated through a comparison with hot-film anemometer data in potential flow regions and in areas of moderate turbulence. The solutions to problems such as selective particle seeding and noise generated from solid surface reflections are required before the system can be fully exploited in the highly turbulent, intermittently reversing flow environment close to the airfoil surface.

Acknowledgements

This research was sponsored by the Frank J. Seiler Research Laboratory under work unit 2307-F1-34.

The authors wish to acknowledge the efforts of Mr. Carl Geddes whose superb craftsmanship was responsible for the fabrication of the experiment and the integration of all component subsystems which make up the LDV. The authors also wish to thank Ms. Donna Weiss for her invaluable aid in the timely preparation of this manuscript.

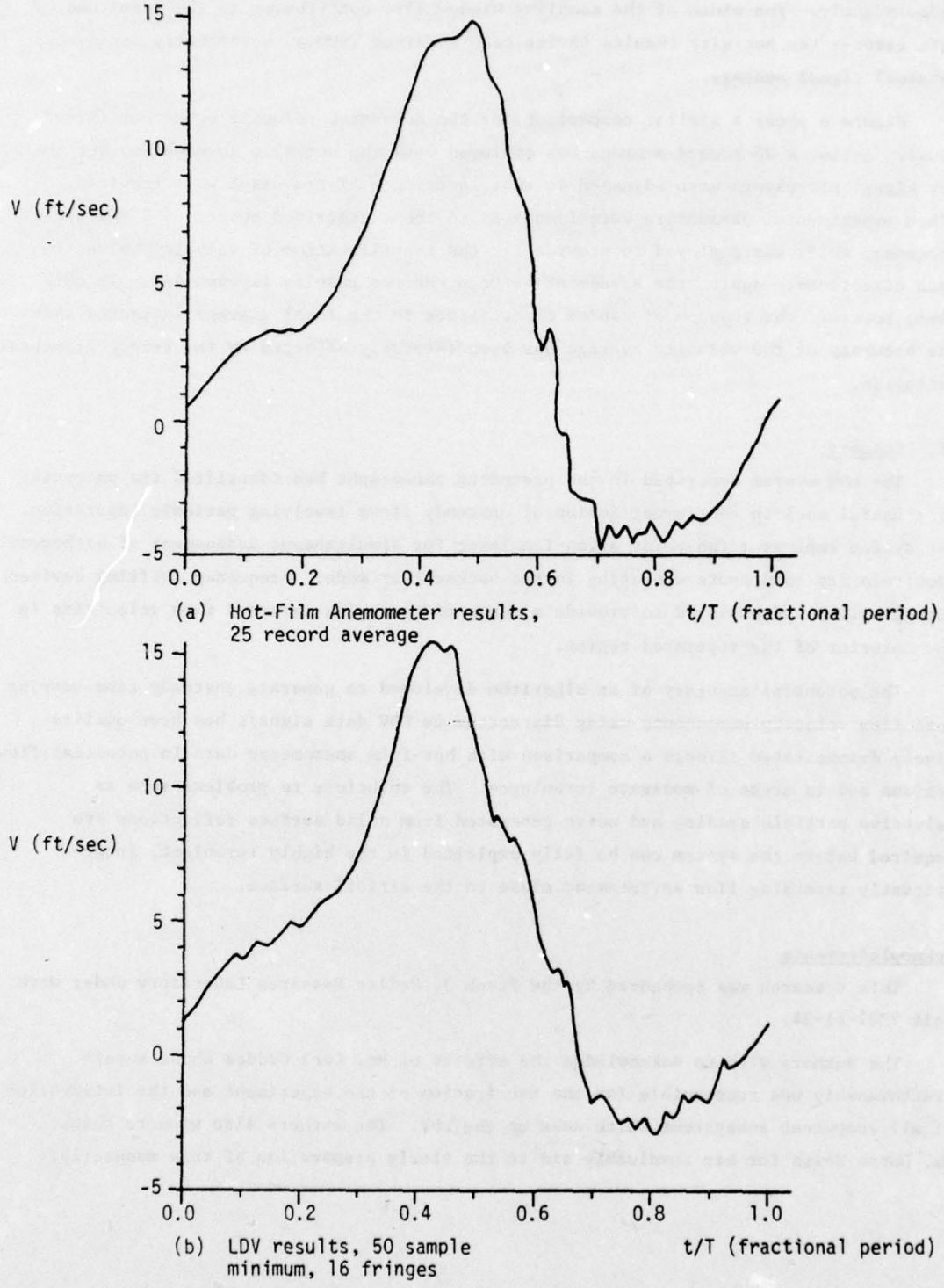

Figure 6. Comparison of Velocity Component Values in the Downwash Direction (Green Beam)

References

1. Yeh, Y. and H. A. Cummins. "Localized Flow Measurements with an He-Ne Laser Spectrometer." Applied Physics Letters, Vol. 4 (1964), 176.

2. Durst, F., A. Melling, and J. H. Whitelaw. Principles and Practice of Laser-Doppler Anemometry. 1st ed. New York: Academic Press, 1976.

3. Keesee, J. E., M. S. Francis, and J. D. Lang. "A Technique for Vorticity Measurement in Unsteady Flow." AIAA Paper 78-801, presented at the 10th Aerodynamic Testing Conference, San Diego, California, 19-21 April 1978.

4. Francis, M. S., et al. "Aerodynamic Characteristics of an Unsteady Separated Region." AIAA Paper 79-0283, presented at the 17th Aerospace Sciences Meeting, New Orleans, Louisiana, 15-17 January 1979.

5. Cline, V. A. and C. F. Lo. "Application of Dual-Scatter Laser Velocimeter in Transonic Flow Research." In Applications of Non-Intrusive Instrumentation in Fluid Flow Research, pp. 1-10. AGARD Conference Proceedings Preprint No. 193, May 1976.

6. McLaughlin, D. K. and W. G. Tiederman. "Biasing Correction for Individual Realization of Laser Anemometer Measurements in Turbulent Flows." Physics of Fluids, Vol. 16 (December 1973), 2082.

7. Dimotakis, P. E. "Single Scattering Particle Laser Doppler Measurements of Turbulence." In Applications of Non-Intrusive Instrumentation in Fluid Flow Research, pp. 1-14. AGARD Conference Proceedings Preprint No. 193, May 1976.

PRELIMINARY WORK ON A PITOT-STATIC HANDBOOK

W. Dieterich*

Abstract

This study was an initial attempt to define and identify the problems involved in the classification of pitot-static probes. There has been to date no systematic approach towards presenting pitot-static data on a common basis and therefore no method has been proposed for a preliminary designer to choose the type and location of the pitot-static system on new aircraft systems. Initial efforts were focused on the collection of past wind tunnel test data on a large number of probes. An attempt to classify the various probes on a consistent basis was made and finally a set of recommendations for future study is proposed.

I. Background

This effort was directed toward the technical need: Improved Pitot-Static Tube Systems for Moderate Angle of Attack and Supersonic Mach Numbers. The TN was originated by Mr. Carroll Butler at the Air Force Armament Test Lab as a result of problems encountered during the High Altitude Supersonic Target (HAST) flight test program where body-mounted L-shaped pitot-static probe-errors were evident in altitude and Mach number. It became apparent that probe technology was not documented for general engineering applications; presently the project engineer is not able to select a particular probe configuration for a specific target/missile application or even identify potential limitations of the selected probe design.

II. Objective

This effort had as its final goal the publication of a Pitot-Static Probe Design Handbook. This handbook on pitot-static probes, it was hoped, would be similar in format to Theory of Wing Sections by Abbott and von Doenhoff.

III. Approach

It was decided that initial efforts would concentrate on the collection and correlation of existing probe data. The specific tasks were to include (1) a comprehensive literature survey on pitot-static probes and angle of attack, α, and sideslip, β, indicators, (2) a compilation of available pitot-static probes and α/β calibration data, including external probe geometric details and (3) a correlation of probe calibration data in a consistent format with common coefficient definitions, plots and tables.

A consistent format for data presentation was decided upon after conferring with Mr. Virgil Ritchie, a consultant at NASA-Langley, and other members attending the 1978

---

*Captain, USAF, Instructor of Aeronautics, DFAN

Air Data Systems Conference held at the Air Force Academy. Each probe that was to be presented in the handbook would have the following data and plots entered:

1. A scale drawing of the probe including external and internal dimensions to include locations of static pressure ports,

2. $\frac{P_m - P_\infty}{P_\infty}$ vs α over a range of Mach numbers, where P_m is measured probe static pressure, and P_∞ is freestream static pressure,

3. $\frac{P_m - P_\infty}{P_\infty}$ vs Mach number over a range of α's, and

4. $\frac{P_{o_m} - P_{o_\infty}}{P_{o_\infty}}$ vs Mach number over a range of α's, where P_{o_m} is the measured probe total pressure and P_{o_∞} is freestream total pressure.

The information in items 1 through 4 above would be presented at $\beta = 0°$ and also at some nominal β.

The initial data search extended from January 1978 to August 1978. The Department of Aeronautics (DFAN) received a large number of reference documents from the Air Force Armament Test Lab. These documents were the first data that were studied. Very few of the documents contained pitot-static wind tunnel data on probe performance. The data contained in these reports were, for the most part, not useful because they generally lacked external probe geometry details, tabularized data, information on the specific test conditions (particularly Reynolds Number) and consistency (or the necessary information to make the data consistent). Additionally, many of the plots were unreadable or exhibited non-reproducibility.

Alternate sources of wind tunnel data were sought. Before I discuss these sources, a brief description of wind tunnel testing and reporting of probes will be given. Most wind tunnel testing of pitot-static probes in this country has been conducted at Arnold Engineering Development Center (AEDC). A majority of these probe tests was conducted for the Rosemount Engineering Co. under the sponsorship of Aeronautical Systems Division (ASD) at Wright-Patterson AFB. Testing of most of the currently used pitot-static systems was conducted during the 1950 through early 1970 time period.

Basic data, to include all measured test parameters which result from a particular test program, are generally presented by AEDC engineers in an unofficial document usually referred to as a "data package." This unofficial document includes all the engineering and other parameters necessary to reduce the data. The data are presented in tabular form. An official "Test Report" is also written by AEDC and it uses a standard format

for the presentation of the data. This official document presents the test data in a graphical format. Many of the test day conditions and other engineering parameters are omitted from this document, without which it is usually impossible to construct alternate curves. These official Test Reports, therefore, are not a suitable source of data for the Pitot-Static Design Handbook. The suitable source is the unofficial data packages since they contain all the necessary test data.

The reference documents sent to DFAN included Test Reports but not the unofficial data packages. It should be strongly noted that the reference documents sent (which did not include the data packages) probably represent the most complete reference set on pitot-static probes in the country.

Contacts at AEDC (ARO) indicated that there might be tabularized probe data at AEDC on tests which had been conducted by Rosemount Engineering Co. Upon further investigation, it was learned that virtually all the probe wind tunnel data prior to 1973 had been destroyed. Only the official Test Reports were retained by AEDC.

Data packages on a limited number of probes were found to be in the personal files of the engineers who had conducted the tests.

Even some of the data packages that were found were of limited usefulness because the probes were designated by Rosemount Engineering with probe descriptions limited to such vague references as probe A, probe B and probe C. These probes were treated as proprietary information and no serial numbers or aircraft types were referenced.

Captain Erwin Jaskolski was the point of contact at the Air Force Office at AEDC. He was particularly helpful in the process of searching for the data packages. Although AEDC had destroyed its copies of the data packages it was learned that copies of the data packages were sent to Rosemount Engineering Co. at the completion of the tests. Mr. Ron Lambdin from the Instrument Branch (ENAID) at ASD, Wright-Patterson AFB, acted as a liaison between the Air Force Academy and Rosemount Engineering Co. Mr. Dick Di Leo at Rosemount was asked if Rosemount would be willing to provide the Air Force Academy copies of the original data packages. Rosemount's reply was an unequivocal no. The legal office at AEDC was contacted and it was their opinion that Rosemount Engineering Co. would not have to provide the Air Force Academy with the data packages. At this point it was decided that enough time had been spent in trying to secure the wind tunnel data.

IV. Results

The original objective of compiling consistent data for a large number of pitot-static probes was not completed. It appears that the only source of the required data is Rosemount Engineering Co. and the Rosemount policy, already expressed, is not to cooperate. The data that were gathered, however, are discussed below.

Figure 1 illustrates the two most revealing facts of this initial study. First, there were only 10 probes found for which there were enough data to plot consistent curves. Second, the 10 probes were tested over limited Mach number ranges and in general there is little overlap between probes.

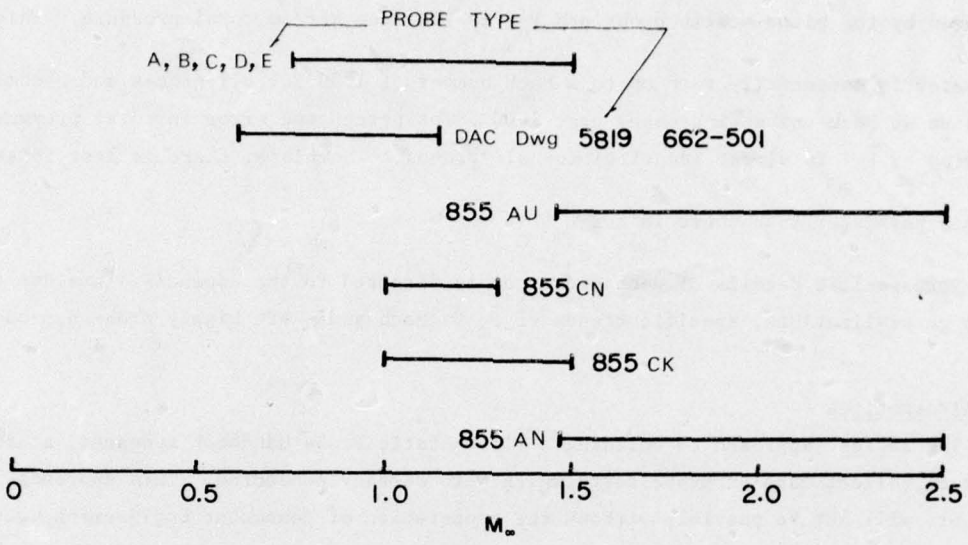

Figure 1. Tested Mach Number Range for Probes Listed in the Appendix

The data in the appendix for the 10 probes use two basic parameters to measure the performance of the probe. The first of these is $\bar{P}_m$,

$$\bar{P}_m = \frac{P_m - P_\infty}{P_\infty} \quad , \tag{1}$$

where P_m is the measured static pressure on the probe and P_∞ is the free stream static pressure. The term $\bar{P}_m$, then, represencs the percentage error in the measurement of static pressure. Wherever possible $\bar{P}_m$ was plotted vs α for constant Mach number and also $\bar{P}_m$ vs Mach (M_∞) for constant α's. In general, most probes exhibit an almost constant value of $\bar{P}_m$ over a range of α's from about -4° to +4° for all Mach numbers except between 1.10 and 1.20. When $\bar{P}_m$ is plotted vs M_∞, $\bar{P}_m$ generally decreases in

value (higher negative value) in the subsonic range. There is a shock induced discontinuity in the value of $\bar{P}_m$ between M_∞ of 1.10 and 1.20. After M_∞ = 1.20 the value of $\bar{P}_m$ generally increases (lower negative value). This occurs at all angles of attack.

The other parameter which is plotted is $\bar{P}_{o_m}$, where P_{o_m} is the total pressure measured by the pitot-static probe and P_{o_∞} is the free stream total pressure. This parameter is essentially zero up to a Mach number of 1.00 for all probes and becomes negative as Mach number increases past 1.00. The percentage error in total pressure as measured by $\bar{P}_{o_m}$ is almost identical for all probes. Therefore, there is less interest in this parameter than there is for $\bar{P}_m$.

For specific details of each probe one is directed to the appendix. Besides the above generalizations, specific trends of $\bar{P}_m$ vs Mach and α are highly probe dependent.

V. Alternatives

The easiest approach to building a Pitot-Static Probe Handbook appeared, at first, to be to collect data on probe tests which were already conducted. This approach, however, will not be possible without the cooperation of Rosemount Engineering Co.

The other alternative is to collect a number of probes and conduct a consistent set of wind tunnel tests on the probes.

VI. Recommendations

In studying the wind tunnel results of a number of probes, we found that very little testing was aimed at comparing various basic probe configurations. As a result, each probe was tested within the specific flight conditions of the vehicle on which it was to be installed. Very little attention was paid to finding out what the Reynolds number effect was on any particular probe. Thus, even if the data packages on a large number of probes had been available, the situation would exist where probe behavior would be known within a very limited Mach and Reynolds number range. The Handbook, for example, would have data on probe #1 for Mach numbers from .1 to .9 and $Re = 1 \times 10^6$. Probe #2 would have data for Mach numbers from 2.0 to 3.0 and $Re = 1 \times 10^5$. It would be very difficult to use such a handbook if each probe had data in a different flight regime.

It appears that the best way of building a useful Pitot-Static Design Handbook would be to design a consistent wind tunnel procedure in which all probes would be tested at the same Mach numbers and range of Reynolds numbers. As mentioned above, very little attention has been paid to Reynolds number. Reynolds number, as it turns out, significantly influences the performance of a probe and must be taken into account.

Due to the expense involved in a wind tunnel test it is recommended that only a limited number of probes (about 10) be tested. Each of these probes should be tested within a consistent Mach number range (M = .2 to 5.0) and Reynolds number (1×10^5 to 1×10^7, based on 1 ft) range.

Conducting a series of probe tests in the same facility would eliminate many questions concerning the reliability of comparing data on one probe tested in tunnel A to another probe tested in tunnel B.

Most of these probes could be procured from Air Force supply through the Air Force Logistics Command.

If the Pitot-Static Design Handbook is to become a reality, it is felt that a test program is the best way to proceed.

References

1. Davis, R. E. "ASD F-104/F-102 Pitot-Static Tube Test Tunnel 1T." AEDC Data Package, Test No. TM 266, May 1970.

2. Davis, R. E. and Ronald G. Lutz. Static Pressure Sensing Characteristics of Three Pitot-Static Probes at Mach Numbers from 1.0 to 2.0. AEDC TR 70-198, September 1970.

3. Hahn, J. "ASD-Rosemount F4-E Pitot-Static Probe." AEDC Data Package, Project No. VD0753, 8 December 1966.

4. Jenke. "ASD-Rosemount RF-101 Pitot Probe." AEDC Data Package, Project No. VD0844, 13 October 1967.

5. Kuklewicz, Edward F. "Transonic Wind Tunnel Tests of Two Prototype Pitot-Static Pressure Probes." Washington, D.C.: Department of the Navy, Aerodynamics Laboratory, Test Report AL 24, February 1966.

6. Rittenhouse, Lewis E. Transonic Wind Tunnel Results for Five Pressure Probes Designed to Minimize Static-Pressure Sensing Errors. AEDC TDR 62-48, March 1962.

APPENDIX

PROBE DATA

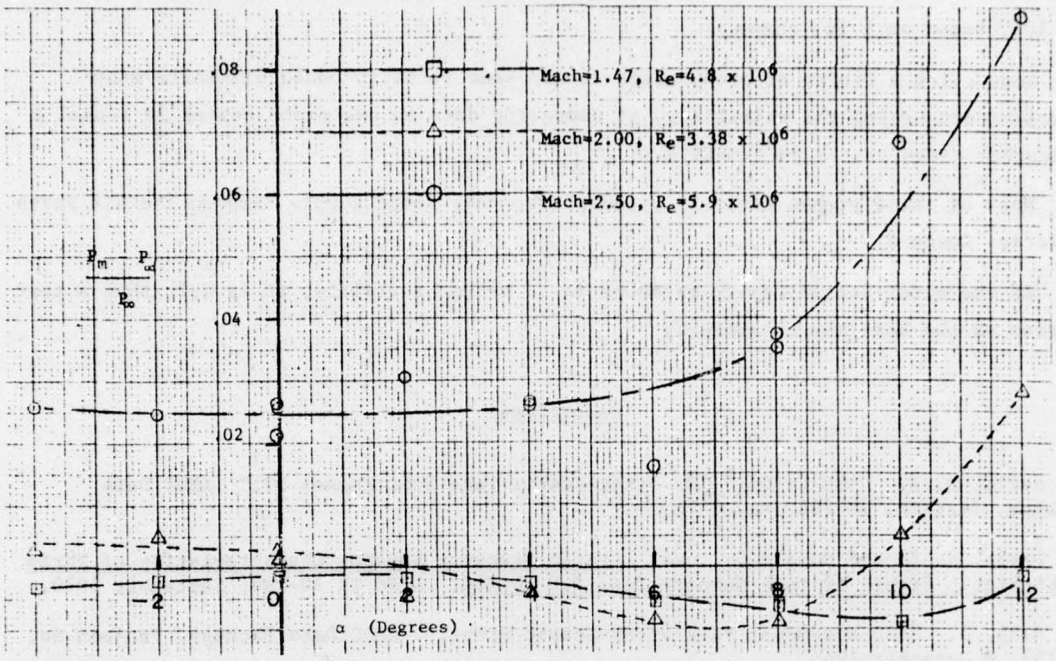

Figure A1. Static Pressure Error for Probe 855 AN (Ref. 3)

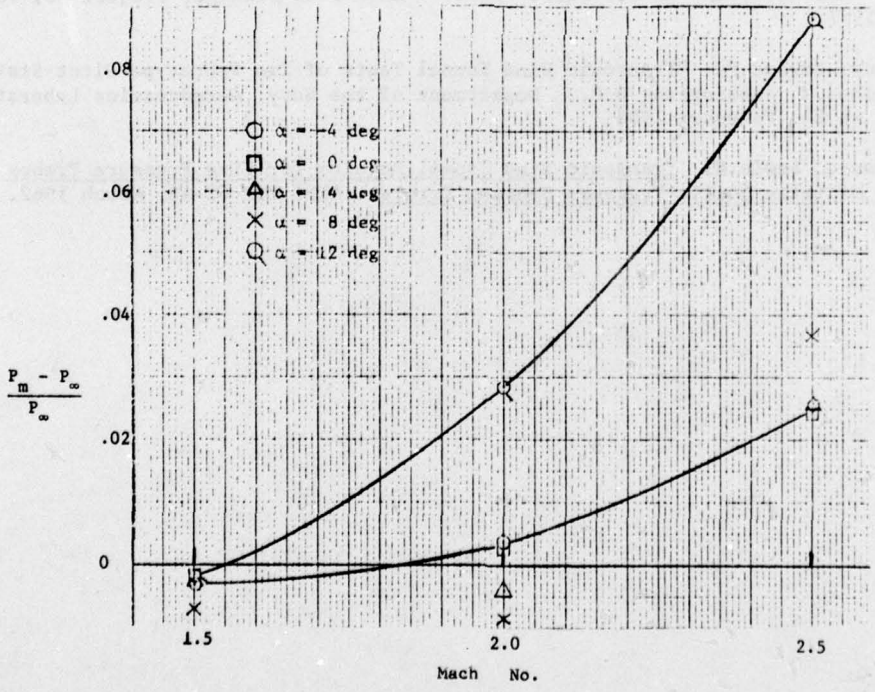

Figure A2. Static Pressure Error for Probe 855 AN (Ref. 3)

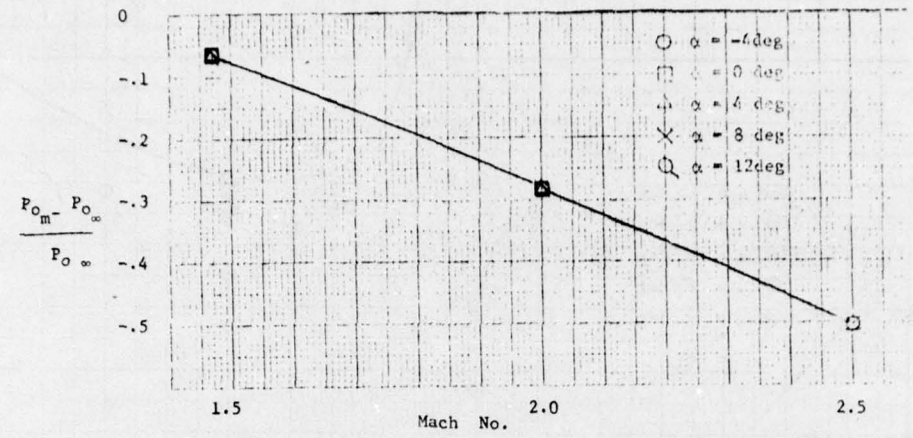

Figure A3. Total Pressure Error vs Mach No. for Probe 855 AN (Ref. 3)

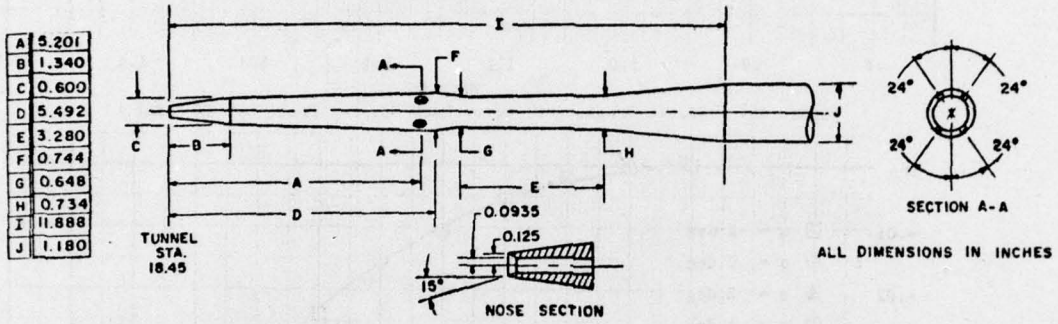

Figure A4. Pitot Probe Details and Dimensions for Probe 855 CK (Ref. 2)

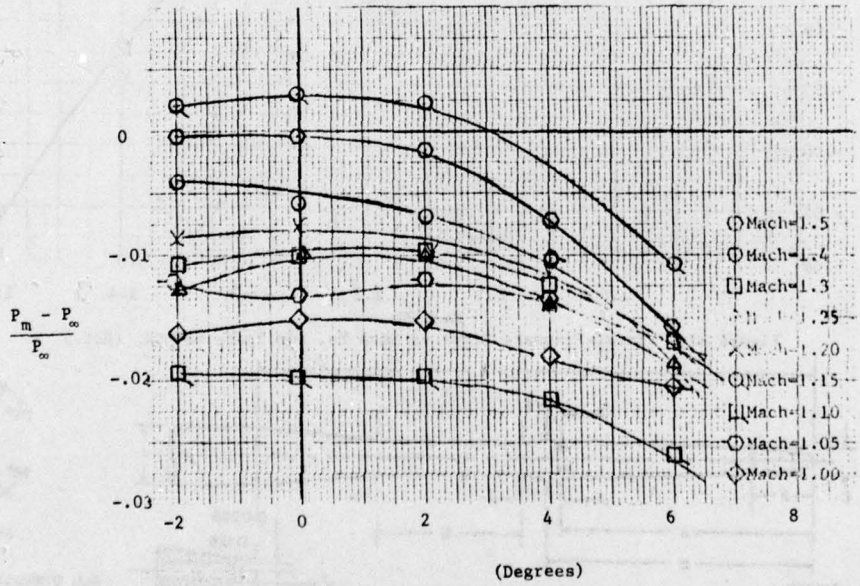

Figure A5. Static Pressure Error for Probe 855 CK (Ref. 1)

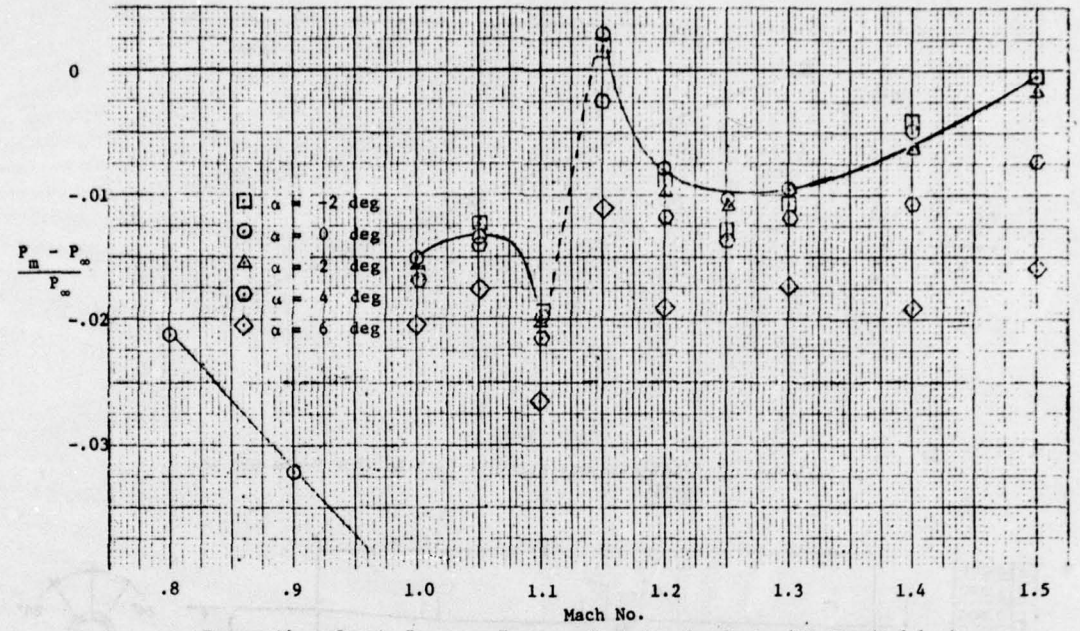

Figure A6. Static Pressure Error vs Mach No. for Probe 855 CK (Ref.1)

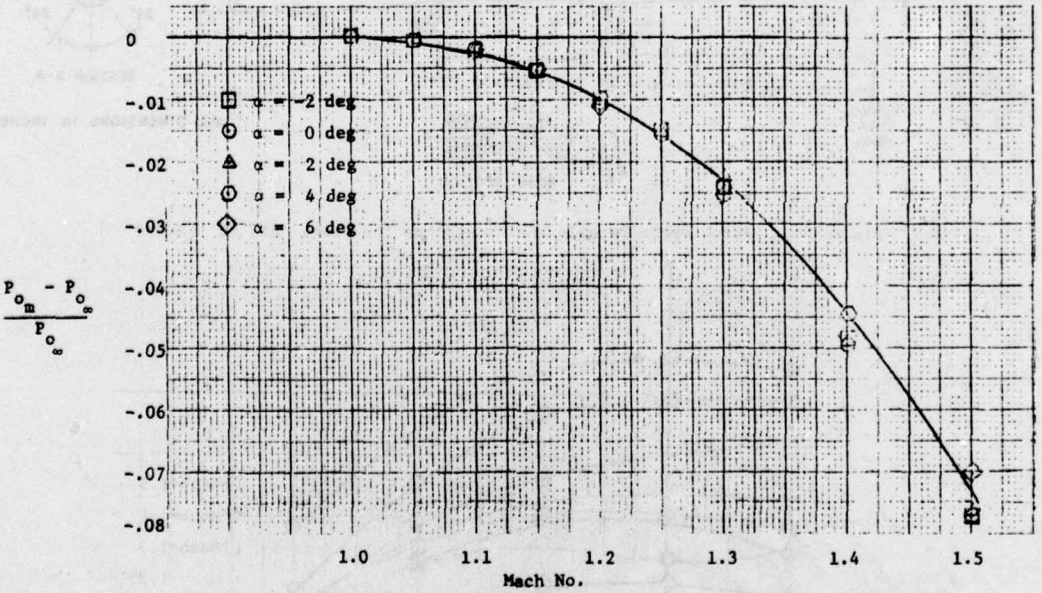

Figure A7. Total Pressure Error vs Mach No. for Probe 855 CK (Ref.1)

A	5.229
B	1.320
C	0.610
D	5.450
E	3.350
F	0.744
G	0.648
H	0.730
I	11.866
J	1.180

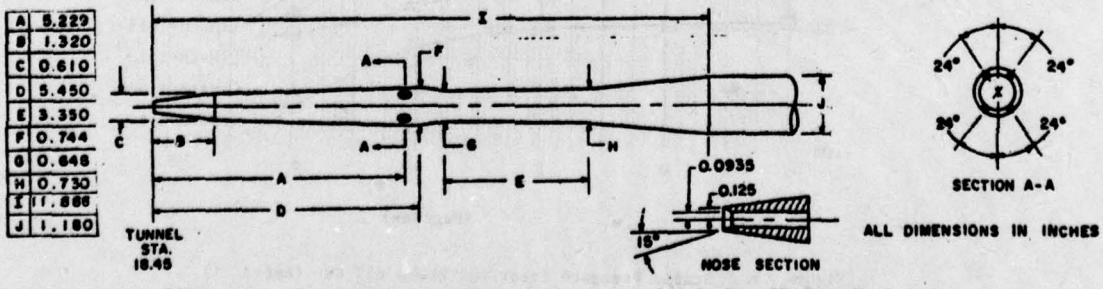

Figure A8. Pitot Probe Details and Dimensions for Probe 855 CN (Ref. 2)

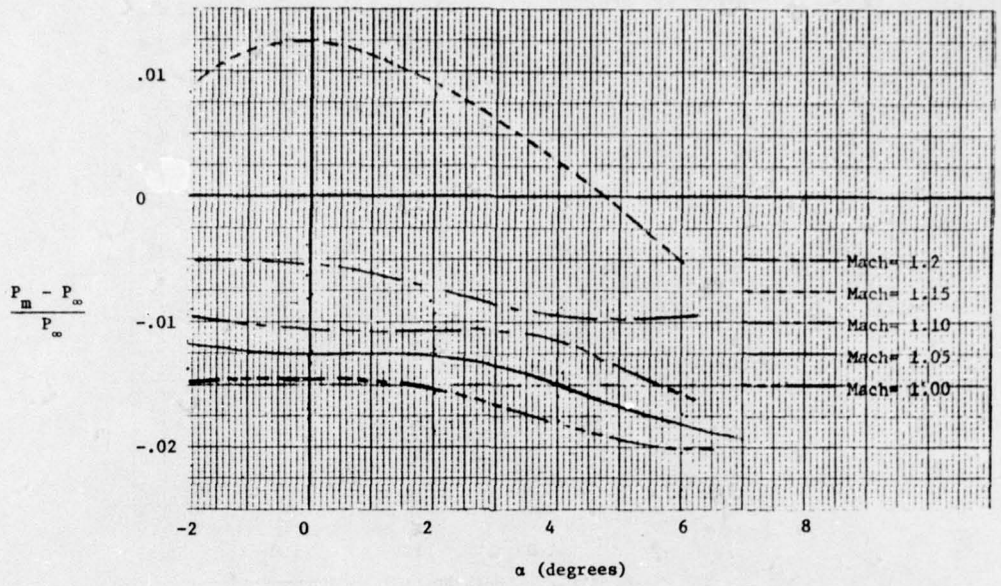

Figure A9. Static Pressure Error vs Angle of Attack for Probe 855 CN (Ref. 1)

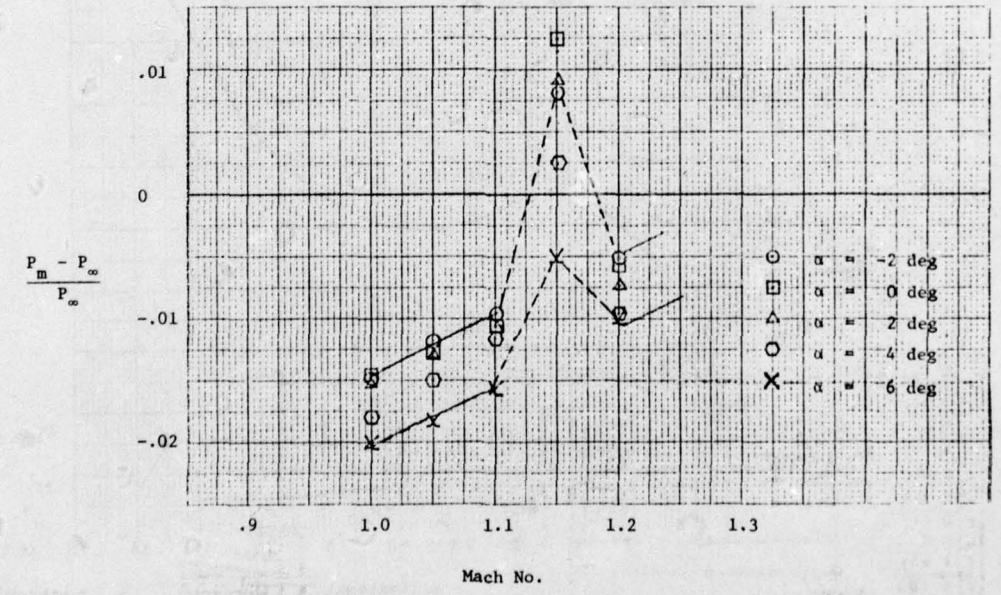

Figure A10. Static Pressure Error vs Mach No. for Probe 855 CN (Ref. 1)

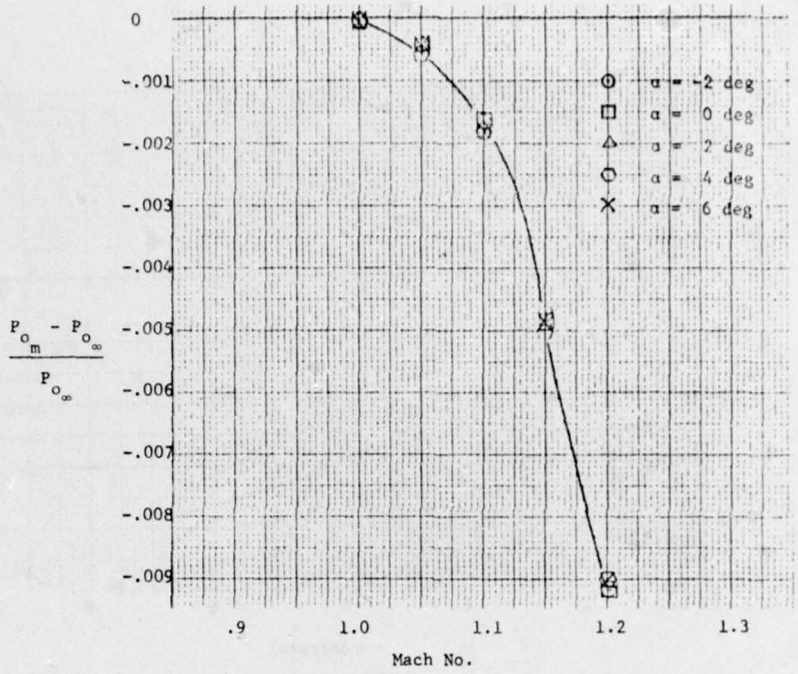

Figure A11. Total Pressure Error vs Mach No. for Probe 855 CN (Ref. 1)

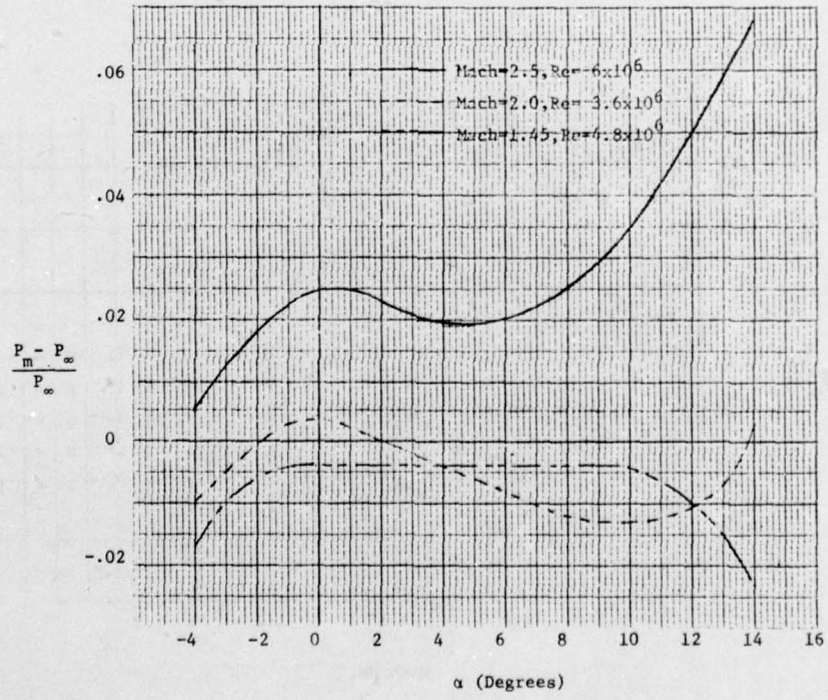

Figure A12. Static Pressure Error vs α for Probe 855 AU (Ref. 4)

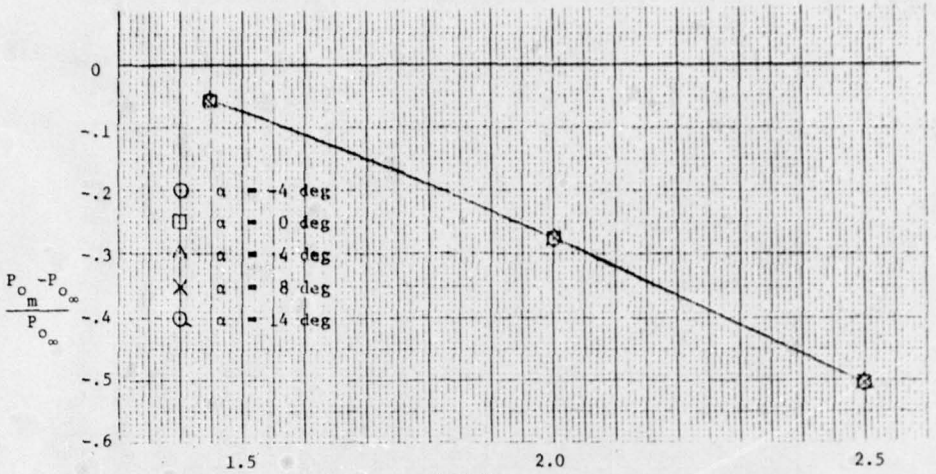

Figure A13. Total Pressure Error vs Mach No. for Probe 855 AU (Ref. 4)

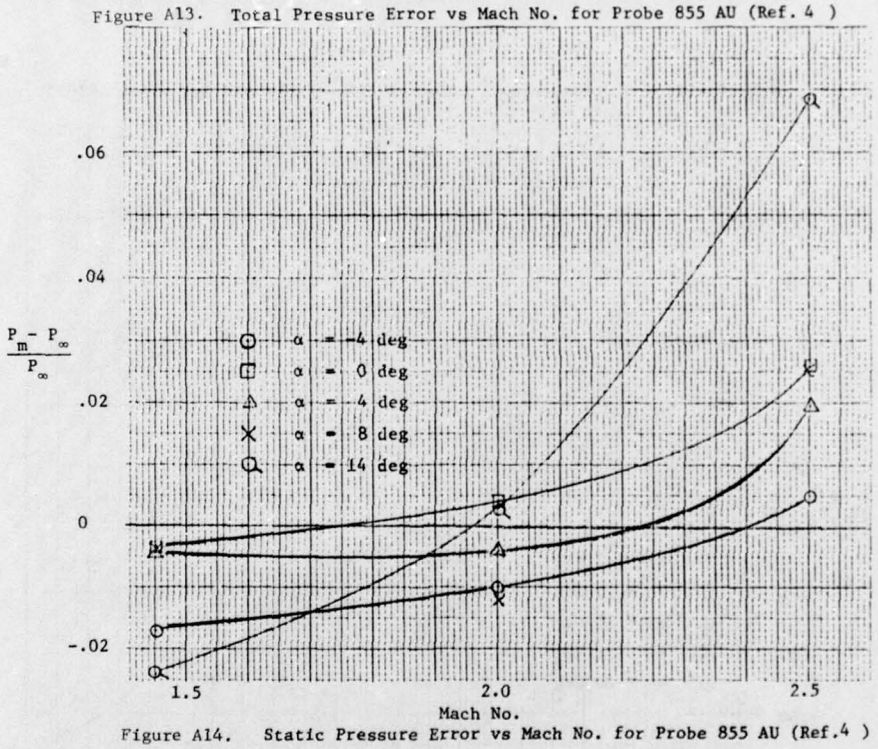

Figure A14. Static Pressure Error vs Mach No. for Probe 855 AU (Ref.4)

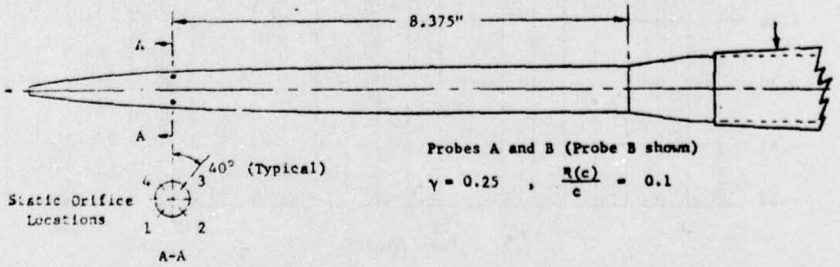

Figure A15. Pitot Probe Details and Dimensions for Probe DAC Dwg 5 819 662-501 (Ref.5)

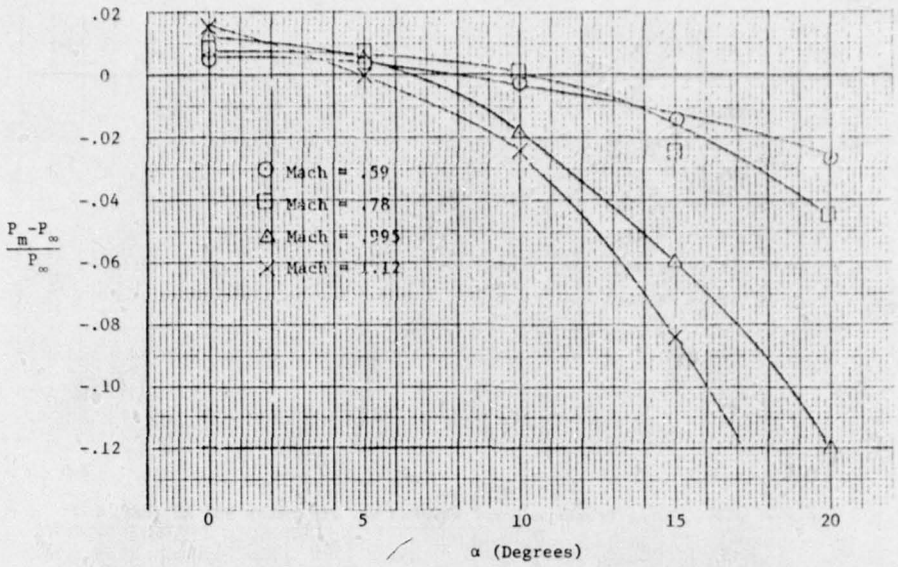

Figure A16. Static Pressure Error vs α for Probe DAC Dwg 5 819 662-501 (Ref. 5)

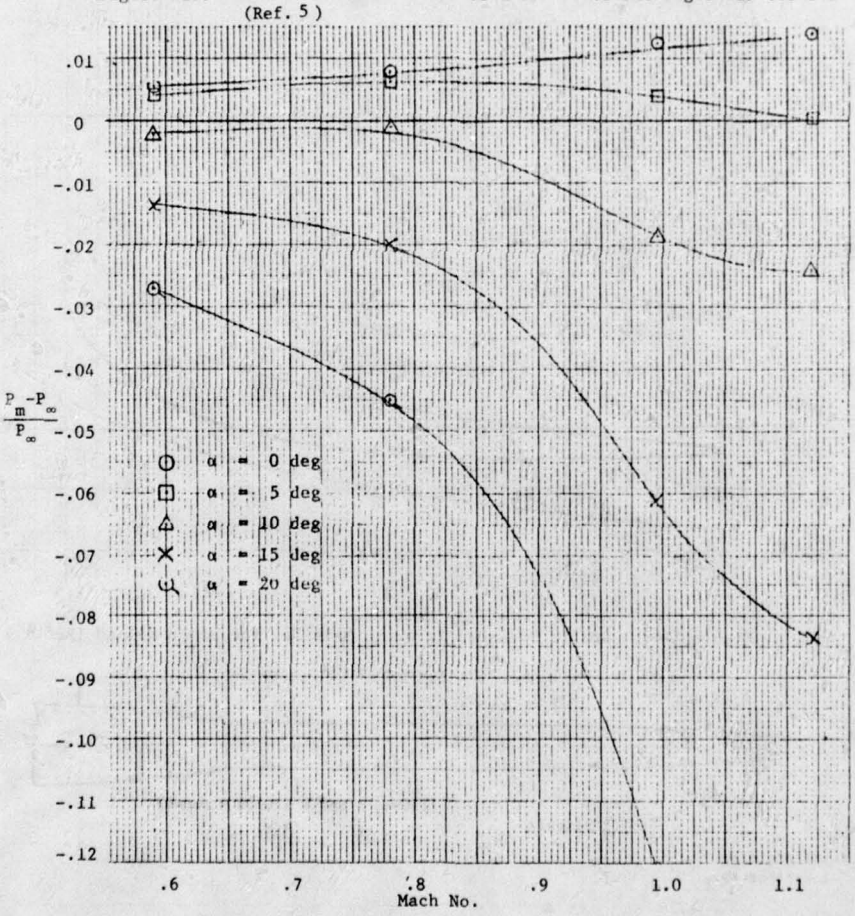

Figure A17. Static Pressure Error vs Mach No. for Probe DAC Dwg 5 819 662-501 (Ref.5)

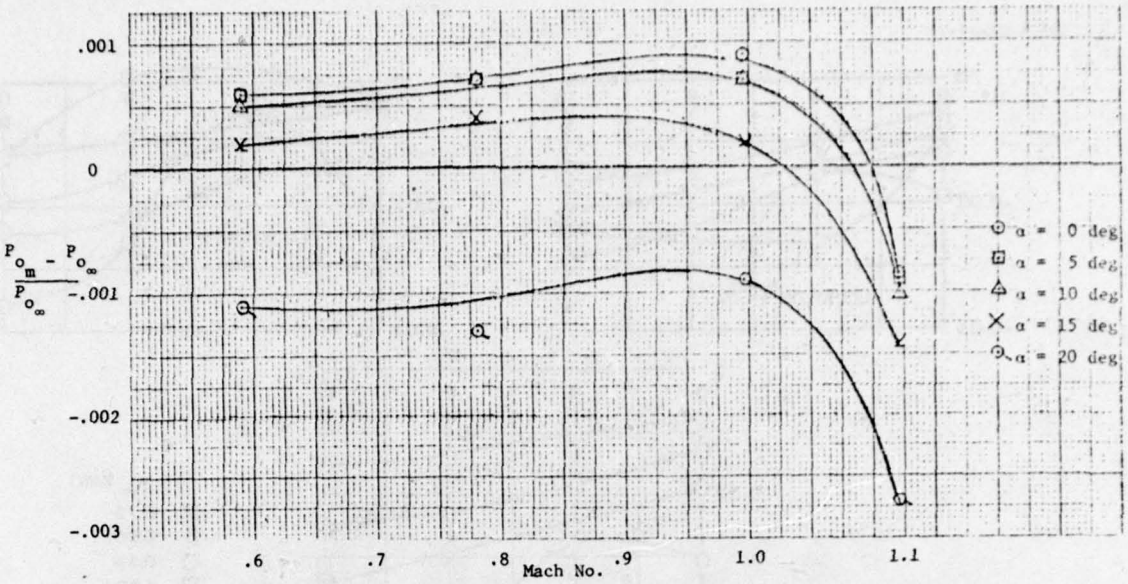

Figure A18. Total Pressure Error vs Mach No. for Probe DAC Dwg 5 819 662-501 (Ref.5)

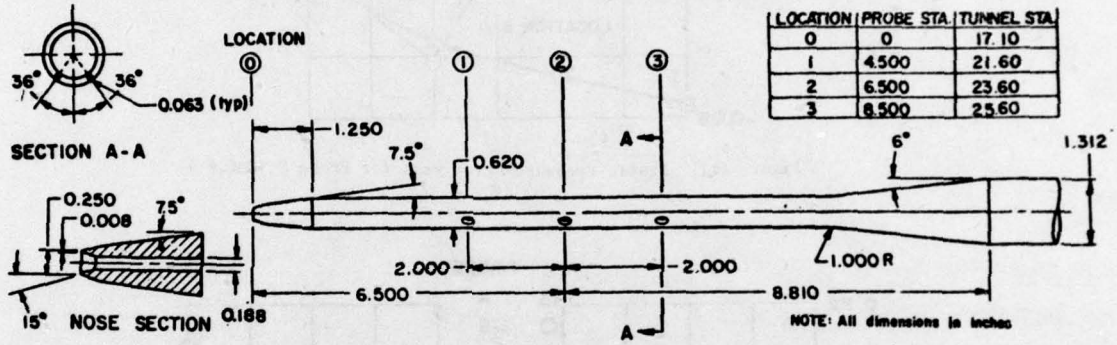

LOCATION	PROBE STA.	TUNNEL STA.
0	0	17.10
1	4.500	21.60
2	6.500	23.60
3	8.500	25.60

Figure A19. Details and Dimensions for Probe E (Ref. 6)

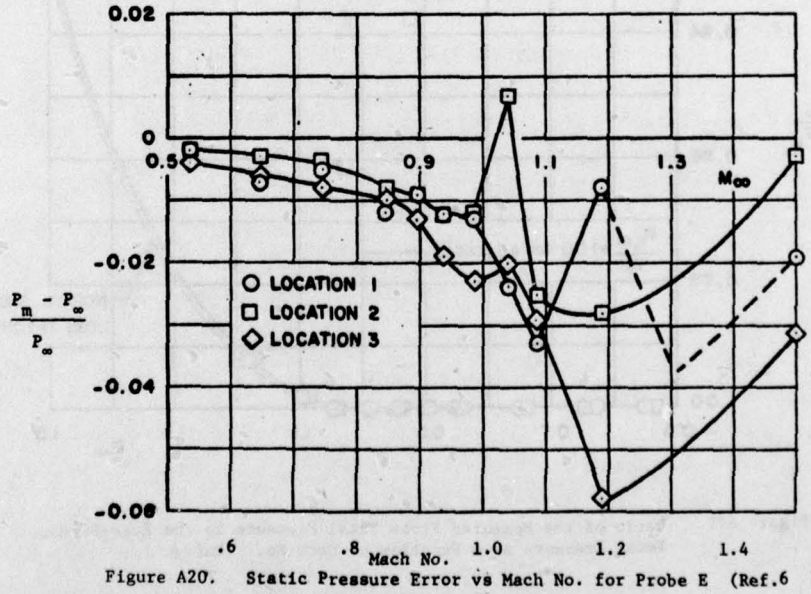

Figure A20. Static Pressure Error vs Mach No. for Probe E (Ref.6)

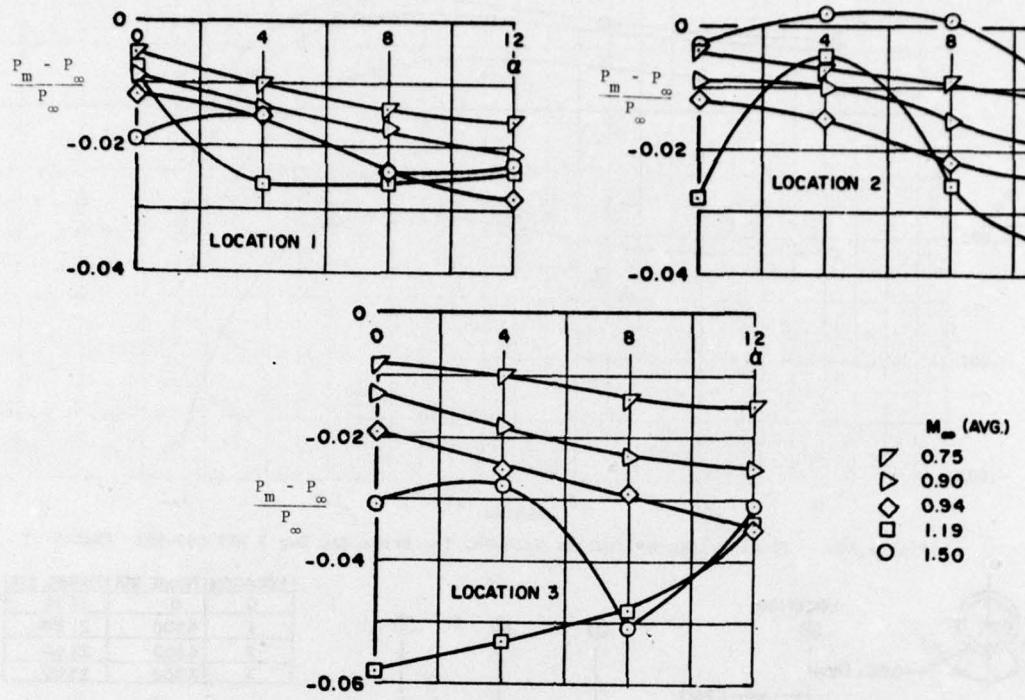

Figure A21. Static Pressure Error vs α for Probe E (Ref.6)

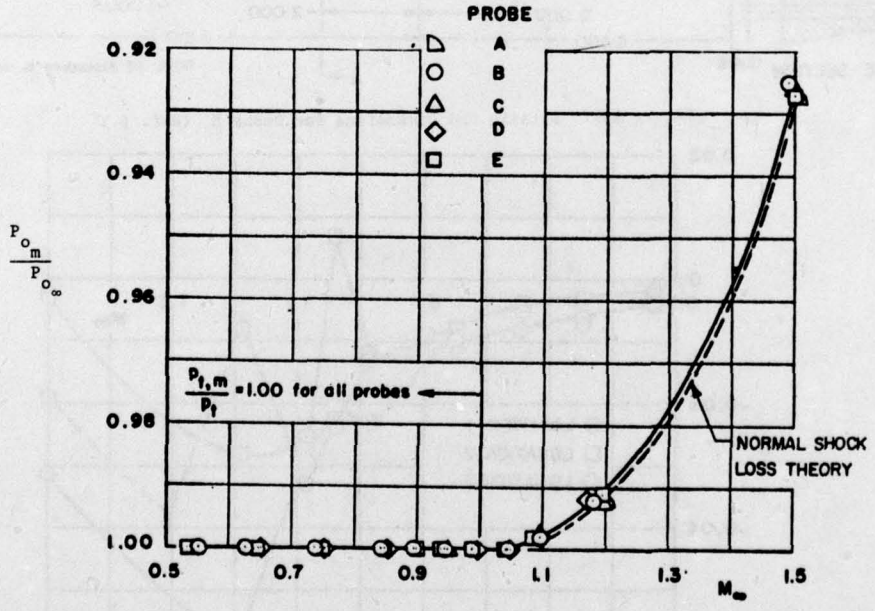

Figure A22. Ratio of the Measured Probe Total Pressure to the Free-Stream Total Pressure as a Function of Mach No. (Ref.6)

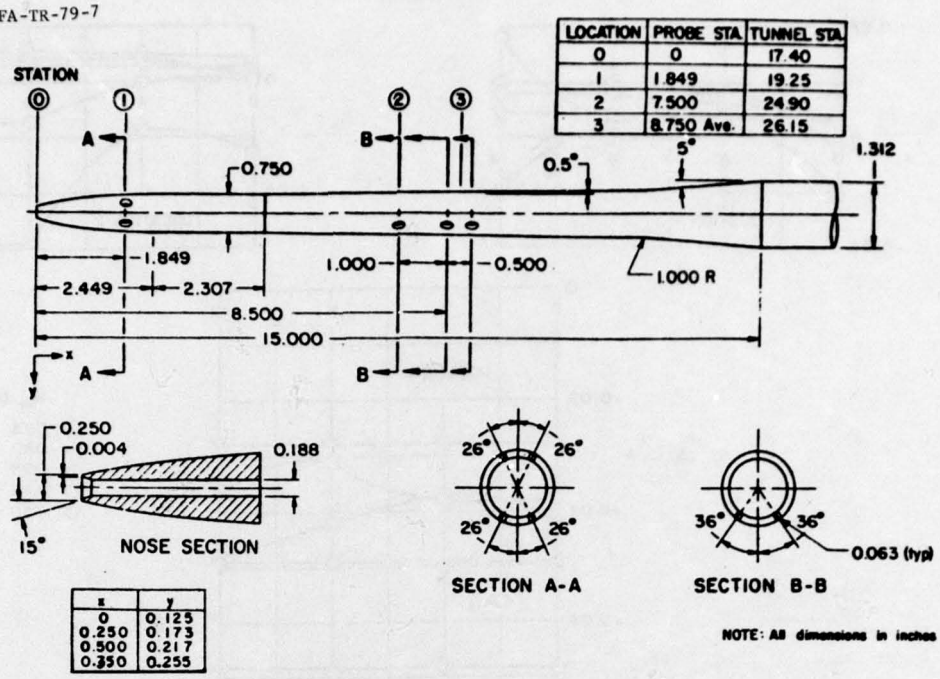

LOCATION	PROBE STA.	TUNNEL STA.
0	0	17.40
1	1.849	19.25
2	7.500	24.90
3	8.750 Ave.	26.15

x	y
0	0.125
0.250	0.173
0.500	0.217
0.750	0.255

Figure A23. Details and Dimensions of Probe D (Ref. 6)

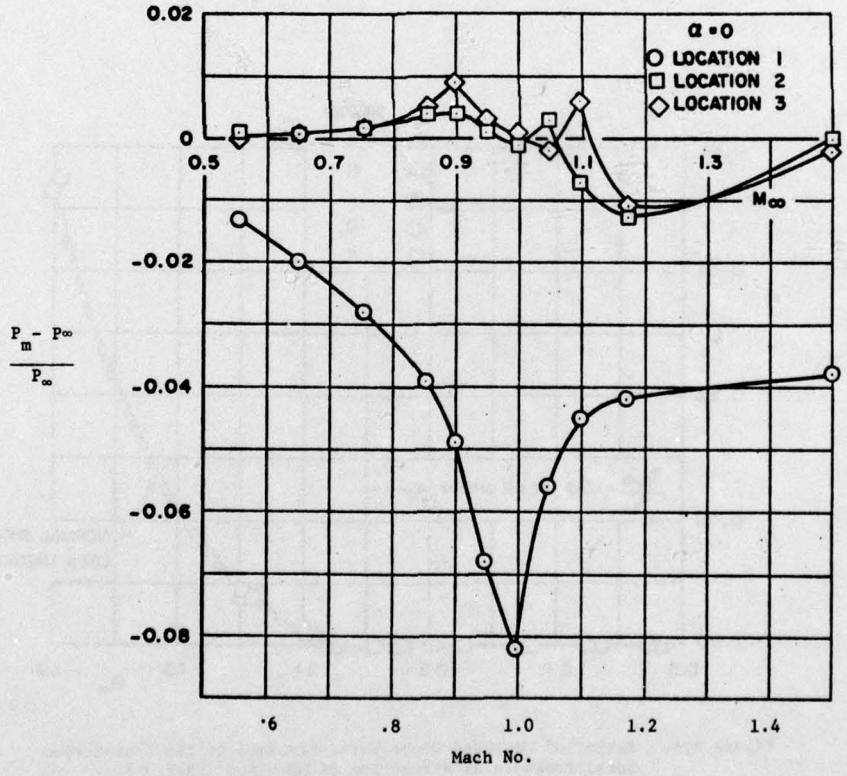

Figure A24. Static Pressure Error vs Mach No. for Probe D (Ref. 6)

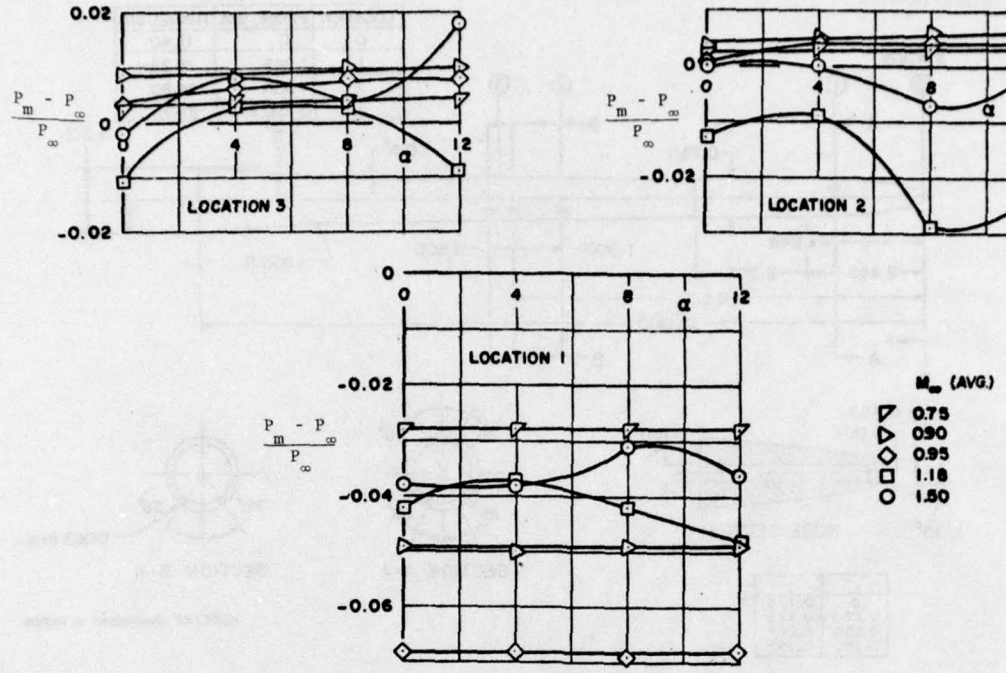

Figure A25. Static Pressure Error vs α for Probe D (Ref. 6)

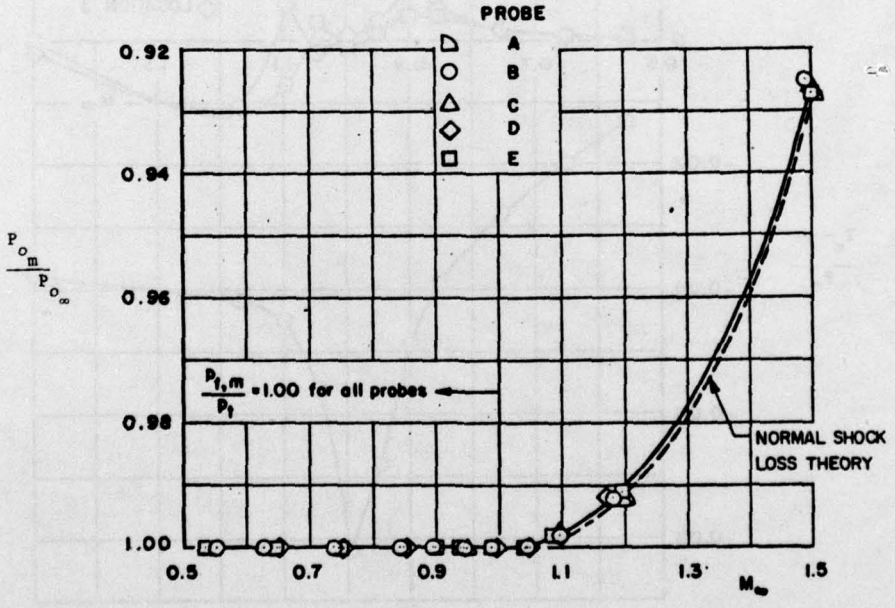

Figure A26. Ratio of Measured Probe Total Pressure to the Free-Stream Total Pressure as a Function of Mach No. (Ref. 6)

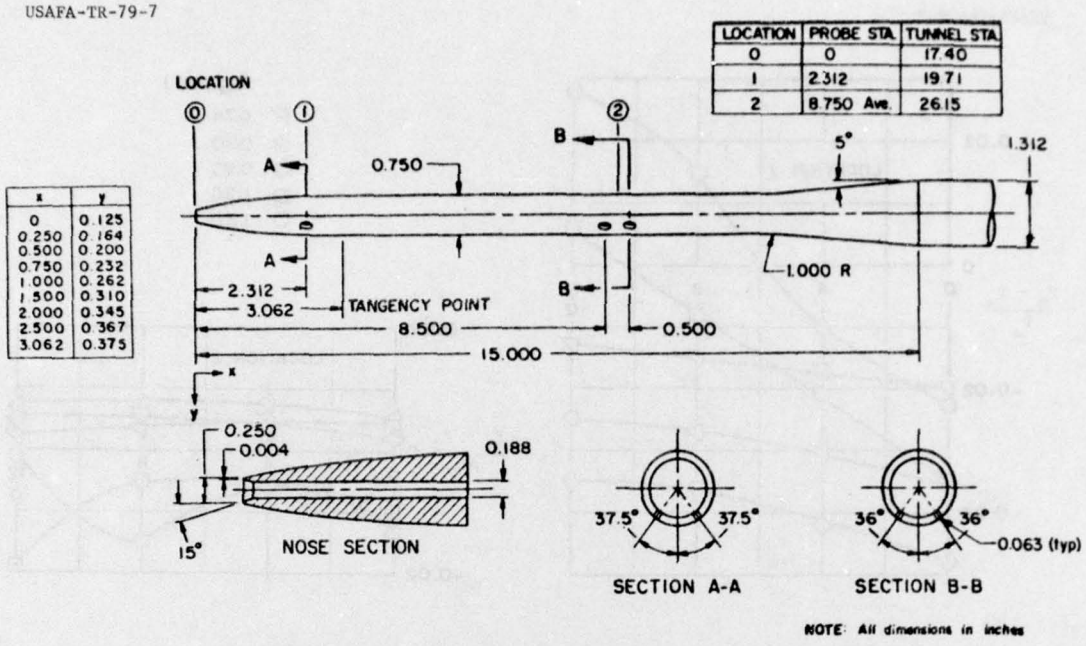

x	y
0	0.125
0.250	0.164
0.500	0.200
0.750	0.232
1.000	0.262
1.500	0.310
2.000	0.345
2.500	0.367
3.062	0.375

LOCATION	PROBE STA.	TUNNEL STA.
0	0	17.40
1	2.312	19.71
2	8.750 Ave.	26.15

Figure A27. Details and Dimensions for Probe C (Ref. 6)

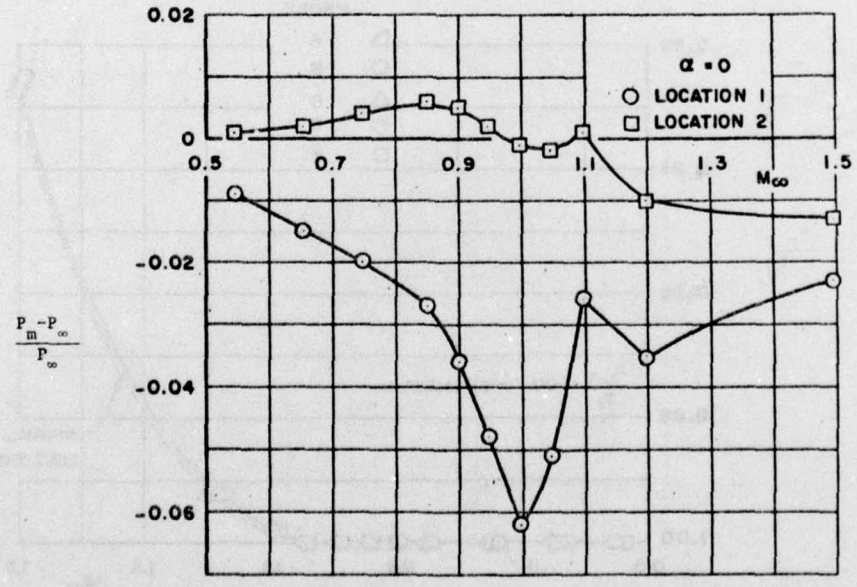

Figure A28. Static Pressure Error vs Mach No. for Probe C (Ref. 6)

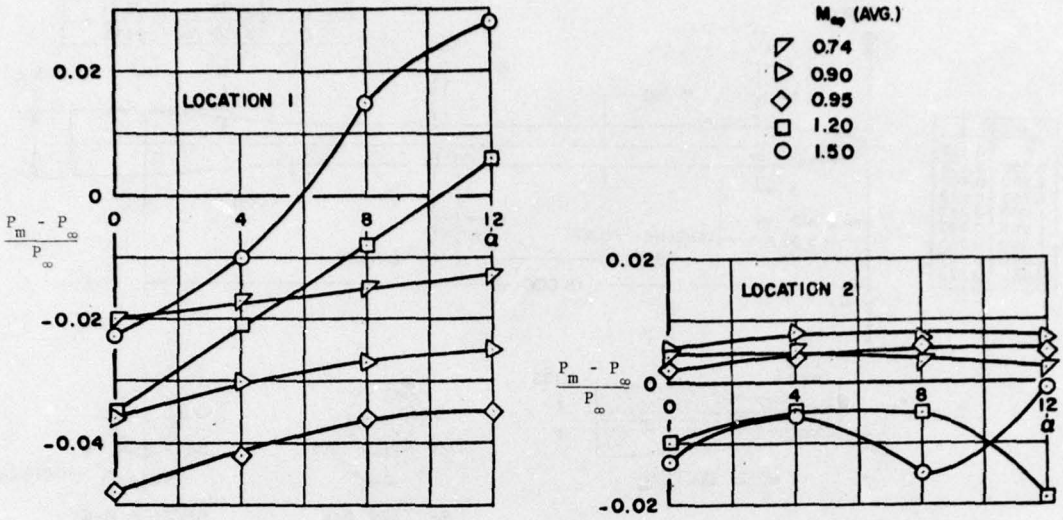

Figure A29. Static Pressure Error α for Probe C (Ref. 6)

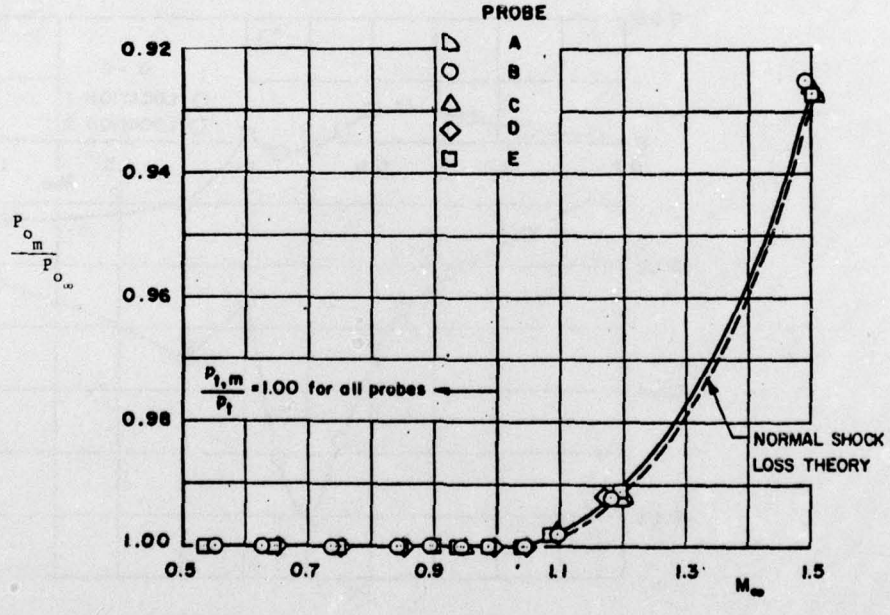

Figure A30. Ratio of the Measured Probe Total Pressure to the Free-Stream Total Pressure as a Function of Mach No. (Ref. 6)

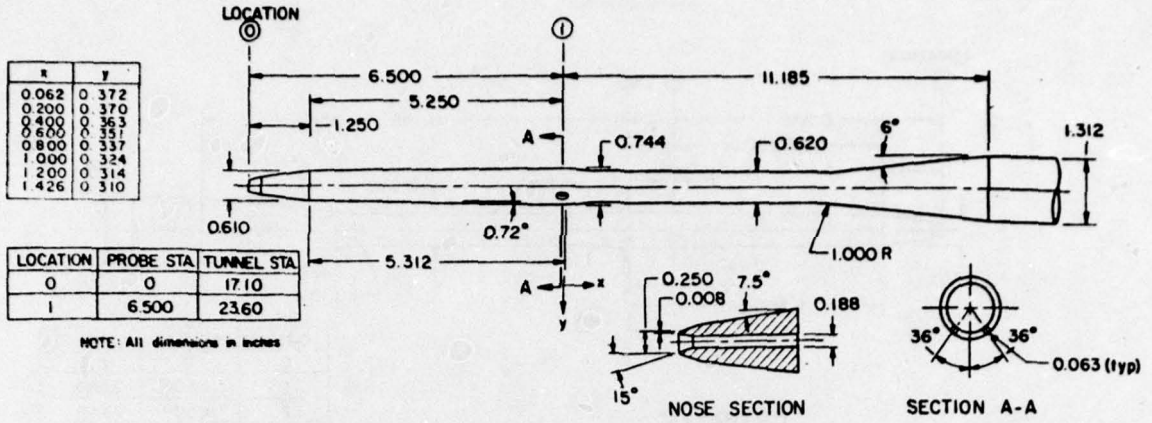

x	y
0.062	0.372
0.200	0.370
0.400	0.363
0.600	0.351
0.800	0.337
1.000	0.324
1.200	0.314
1.426	0.310

LOCATION	PROBE STA	TUNNEL STA
0	0	17.10
1	6.500	23.60

Figure A31. Details and Dimensions for Probe B (Ref. 6)

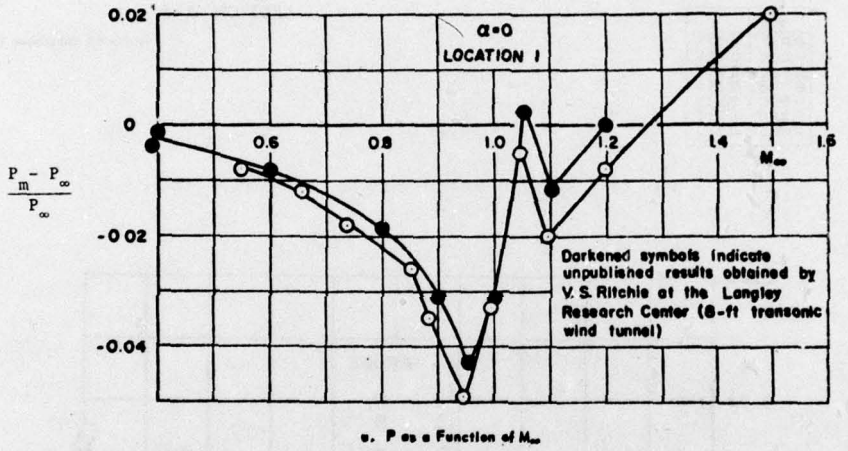

a. P as a Function of M_∞

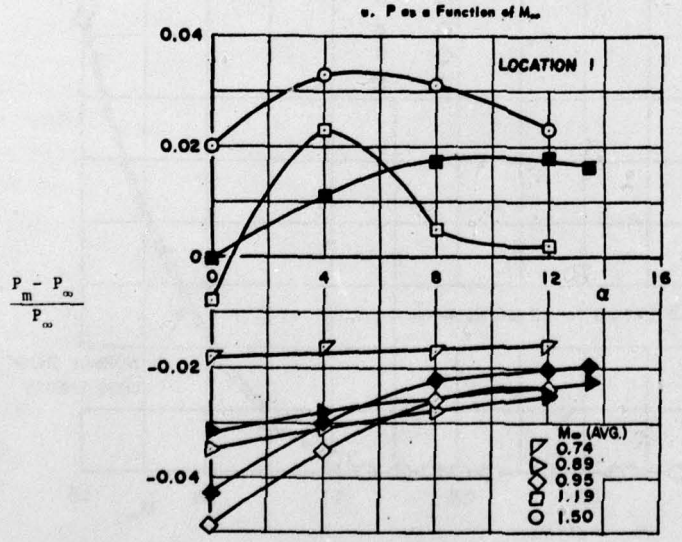

Figure A32. Static Pressure Error vs α for Probe B (Ref.6)

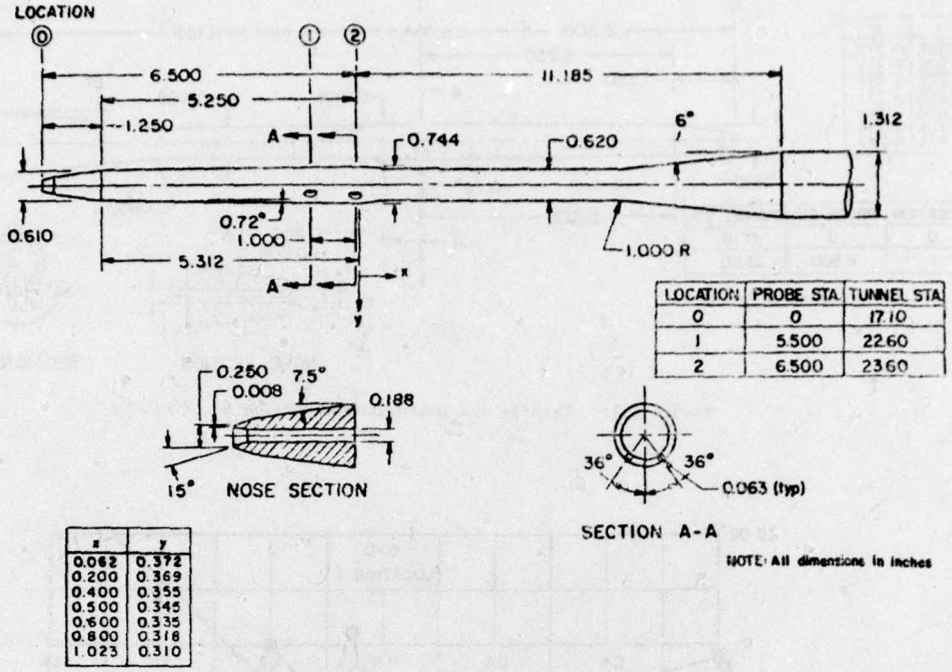

LOCATION	PROBE STA.	TUNNEL STA.
0	0	17.10
1	5.500	22.60
2	6.500	23.60

x	y
0.062	0.372
0.200	0.369
0.400	0.355
0.500	0.345
0.600	0.335
0.800	0.318
1.023	0.310

Figure A33. Details and Dimensions for Probe A (Ref. 6)

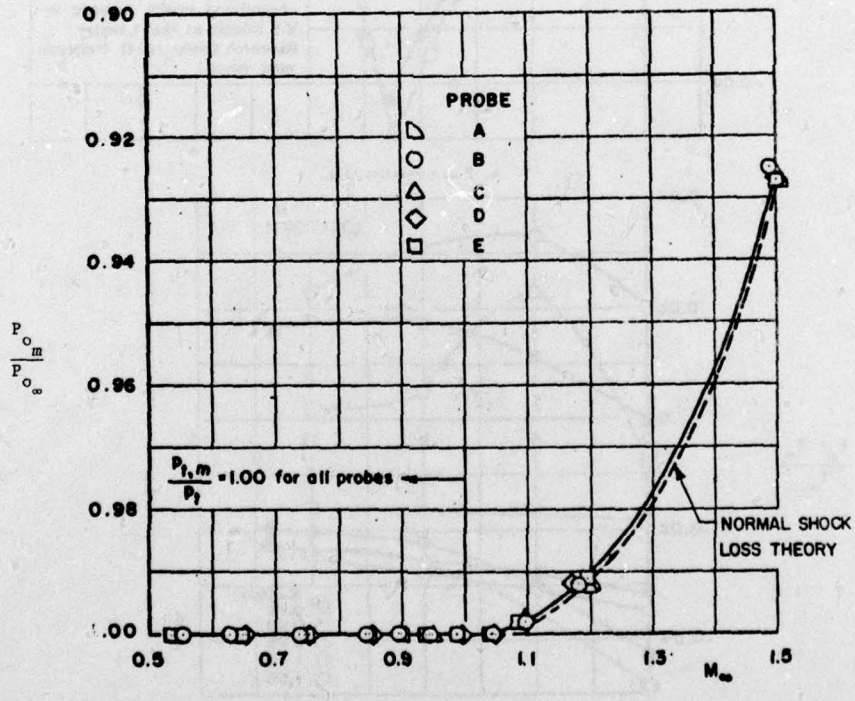

Figure A34. Ratio of the Measured Probe Total Pressure to the Free-Stream Total Pressure as a Function of Mach No. (Ref. 6)

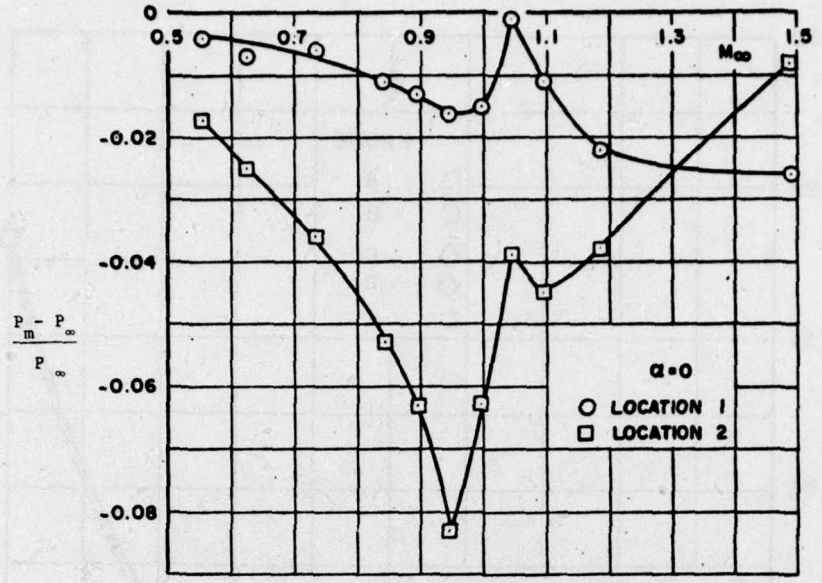

Figure A35. Static Pressure Error vs Mach No. for Probe A (Ref. 6)

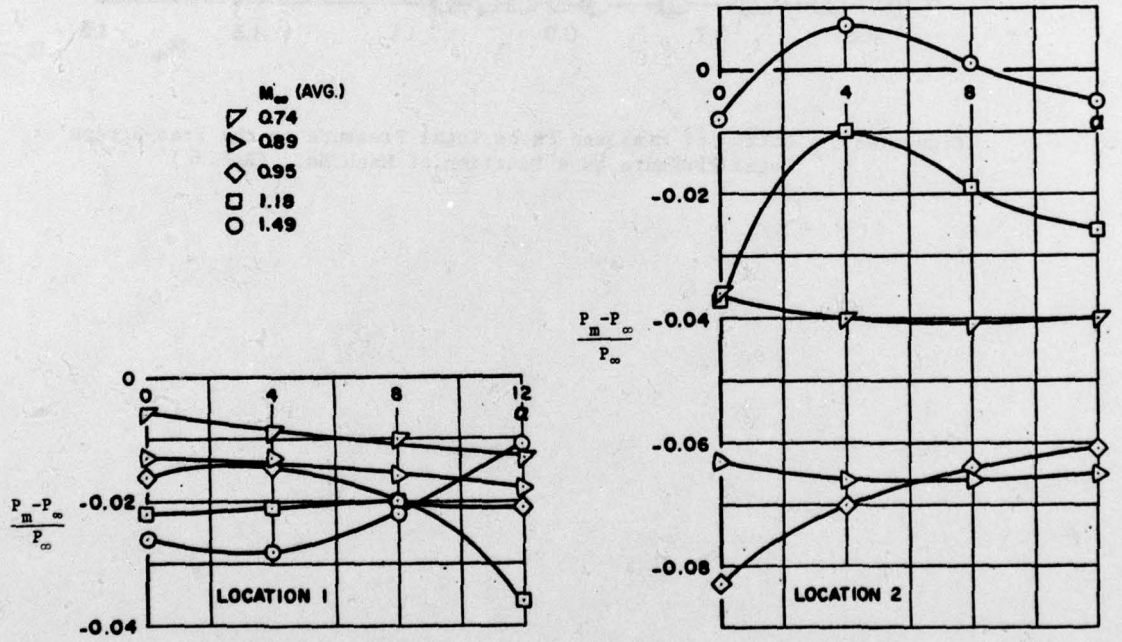

Figure A36. Static Pressure Error vs α for Probe A (Ref. 6)

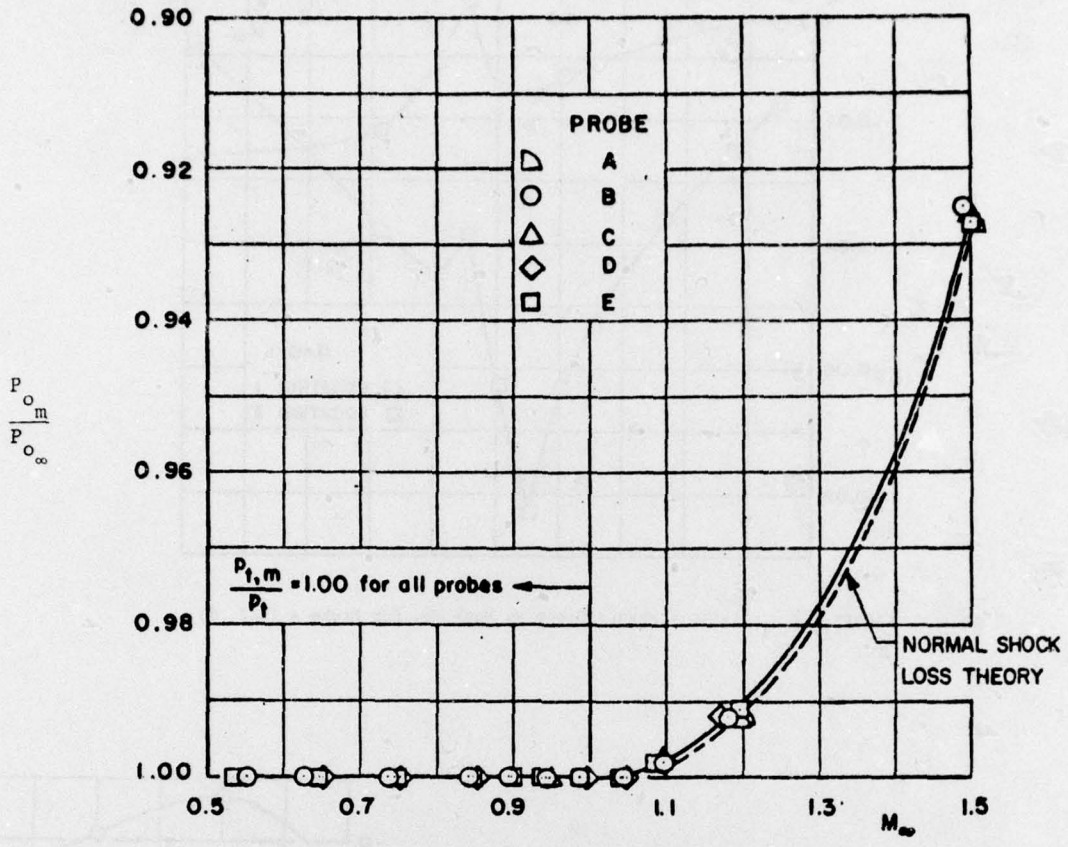

Figure A37. Ratio of Measured Probe Total Pressure to the Free-Stream Total Pressure as a Function of Mach No. (Ref. 6)

SECTION VI

ABSTRACTS

PREDICTED AND MEASURED MAXIMUM INSTANTANEOUS DISTORTION FOR FLIGHT AND WIND TUNNEL MODEL DATA FOR A MIXED-COMPRESSION INLET[+]

H. M. Brilliant,* C. A. Bauer,** and Robert A. Davis***

Extended Abstract

The integration of an engine into an aircraft creates many problems that are not experienced when the engine is tested in a direct-connect mode. One problem is the time varying total pressure distortion produced by the inlet and felt by the compressor. This distortion tends to lower the stability margin of the compressor. Most development programs rely heavily on testing of both inlets and engines in wind-tunnel and propulsion system facilities to insure compatability. Testing is expensive and time consuming because large quantities (generally 24 to 40) of high response pressure measurements at the compressor station must be obtained and analyzed.

As an alternative, Melick, Ybarra, and Bencze (Ref. 1 and 2) developed a less expensive approach of determining the probable maximum instantaneous distortion using fewer (six to eight) total pressure measurements. This method required only the mean value of the pressure and the root mean square value (RMS) of the pressure fluctuations, rather than the actual instantaneous values. They used fundamental fluid mechanics to describe the flow as a vortex created in the inlet is transported downstream to the compressor. Then, using statistics to analyze the effect of randomly distributed vortices, they determined relationships among the pressure fluctuations, steady state distortion, the probable maximum value of instantaneous distortion for the test time interval, and other flow properties. We modified their method to apply it to data available for the YF-12 inlet and engine. The goal of this study was to evaluate this new method.

In applying the method of Melick, Ybarra, and Bencze, we analyzed data from 1/3-scale and full-scale wind tunnel and from flight tests. The 1/3-scale inlet contained 40 high frequency response transducers mounted in eight 5-probe area-weighted rakes. The other two inlets contained 24 transducers mounted in six 4-probe rakes. Data were recorded on analog tape and digitized at 2000 or more samples per second. Both the conventional method for finding the instantaneous distortion and the Melick method were

---

[+]Presented at the YF-12 Experiments Symposium held at NASA Dryden Flight Research Center, 13-15 Sep 1978. Report is classified. Copies are available from NASA DFRC, PO Box 273, Edwards AFB, CA 93523

*Captain, USAF, Associate Professor of Aeronautics, DFAN

**Project Engineer, NASA Dryden Flight Research Center

***Co-op Student, NASA Dryden Flight Research Center

used to reduce data. A statistical maximum instantaneous distortion was determined using the results from the conventional method and was used for comparison.

Figure 1 shows some typical results obtained in evaluating subsets of the total set of probes for the full-scale inlet tests. Each ring of six probes (one from each rake) was evaluated to determine which ring gave the best predicted value. In this case, the percent difference (PD) between the predicted value of maximum instantaneous distortion and the measured statistical maximum value was plotted versus the ring-averaged RMS of the total pressure fluctuations. The results are shown for three different distortion indices, two of which are measures of circumferential distortion (K_θ and IDC), and one of radial distortion (K_R). Note that ring 1 is located near the centerbody where the flow is less turbulent than in the overall flow (as indicated by the RMS); ring 4 is located near the outer wall where the flow is more turbulent. While these results are for the full-scale inlet tests, the results for the 1/3-scale inlet test and the flight tests were similar.

Figure 2 shows a more complete set of results for the flight test at a high Mach number. A fourth distortion index, K_A, is a combined index; in our case, it was the sum of K_θ and K_R. Predicted distortion indices were generally within 20% of measure values. Rings 2 and 3 generally predict values very similar to the 24-probe value. However, the 24-probe value may not always be the most accurate prediction.

Applying the method to all three sets of tests, we found that the predict values of maximum instantaneous radial and circumferential distortion indices are generally within 20% of the measured statistical maximum throughout the Mach number range. The combined distortion index is within 5% of the measured value. A priori knowledge of high, low, and mean turbulence intensity areas at the compressor face is helpful in order to successfully improve the accuracy of the Melick method. However, when one set of probes is chosen, it does not consistently improve the accuracy of the prediction. Depending on the accuracy required, the method can be used to reduce the data acquisition and reduction cost and time.

References

1. Melick, H. C., A. H. Ybarra, and D. P. Bencze. Estimating Maximum Instantaneous Distortion From Inlet Total Pressure RMS and PSD Measurements. NASA TMX-73,145, 1976.

2. Melick, H. C., A. H. Ybarra, and D. P. Bencze. "Estimating Maximum Instantaneous Distortion From Inlet Total Pressure RMS Measurements." AIAA Paper 78-970, presented at the AIAA/SAE 14th Joint Propulsion Conference, Las Vegas, Nevada, 25-27 July 1978.

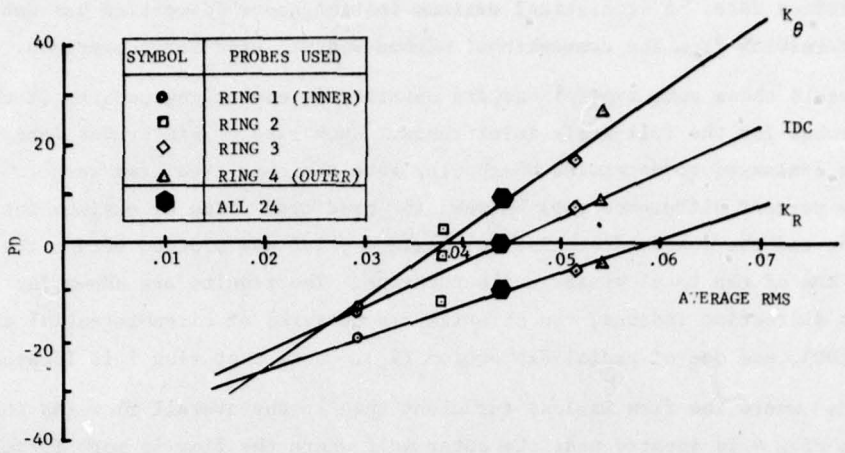

Figure 1. Influence of Average RMS on the Accuracy of the Prediction for One Full-Scale Test Point

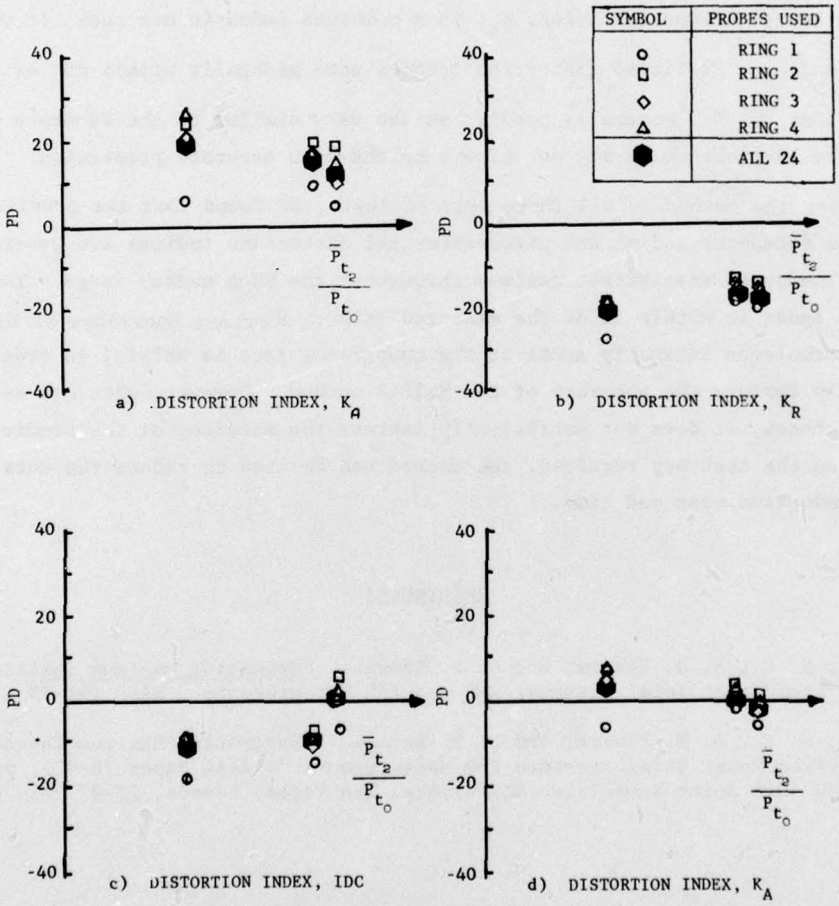

Figure 2. Effect of Ring on the Accuracy of the Prediction for Different Inlet Recoveries for Flight Tests at a Given Mach Number

★ U.S. GOVERNMENT PRINTING OFFICE: 1979-0-681-044/27